Electronic Thesis and Dissertation Repository

6-22-2020 2:00 PM

Neurite Orientation Dispersion and Density Imaging in a Rodent Model of Mild Traumatic Brain Injury

Patrick McCunn, *The University of Western Ontario*

Supervisor: Bartha, Robert, *The University of Western Ontario*
A thesis submitted in partial fulfillment of the requirements for the Doctor of Philosophy degree in Medical Biophysics
© Patrick McCunn 2020

Follow this and additional works at: https://ir.lib.uwo.ca/etd

Part of the Medical Biophysics Commons

Abstract

Mild traumatic brain injury (mTBI) has become a focal point within the medical community due to its increased prevalence in recent years. Unfortunately, there is currently no neuroimaging technique able to accurately diagnose and monitor mTBI *in-vivo*. One technique that has shown great promise is neurite orientation dispersion and density imaging (NODDI). NODDI is a diffusion MRI (dMRI) technique used to characterize microstructural complexity through the compartmental modelling of neural water fractions into Intra-neurite, Extra-neurite and CSF volume fractions. The overreaching theme of this thesis was to validate NODDI in a preclinical setting to then be applied to imaging of early mTBI. In the first study, NODDI was shown to have high precision and repeatability both between and within subject. Furthermore, it was found that small biological changes (<5%) may be detected with feasible sample sizes for NODDI metrics indicating it to be a useful tool within the preclinical research setting at 9.4 Tesla. Following this validation NODDI was used to image the early stages of mTBI in a rodent model. NODDI was able to detect changes in neurite microstructure within the first hour on mTBI. Following this successful application, NODDI was applied to a rodent model of repetitive mTBI. Many athletes experience multiple mTBI's over the course of a season and the cumulative effect of these injuries is still unknown. NODDI was successfully able to detect altered water diffusion characteristics in the brain of rodents following both a first a second mTBI. Converse to our hypothesis, the measured changes did not differ between the first and second impact on a group wise scale. These changes reinforce our previous findings showing an immediate change to the microstructure of the brain following an initial mTBI, and further this knowledge by indicating a heterogeneous individual response to the second mTBI. Further it was shown that some of these changes did not return to normal between the two injuries, potentially providing a window into the changes within the brain.

Keywords

Lay Summary

Mild traumatic brain injury (mTBI) has become an important public health concern as these injuries have become increasingly common in recent years. Unfortunately, there is no current medical imaging technique that allows accurate diagnosis and monitoring of mTBI. This is because many neuroimaging techniques such as computed tomography (CT) and positron emission tomography (PET) lack the specificity to identify the subtle damage present in the brains of those suffering from mTBI. Magnetic resonance imaging (MRI) is a good candidate to identify these changes due to its strong soft tissue contrast. One specific MRI technique that has shown promise in detecting subtle brain microstructural changes is neurite orientation dispersion and density imaging (NODDI). NODDI is able to quantify the density and spatial organization of various anatomical structures in the brain such as axons and dendrites and as such presents an opportunity to monitor brain health after injury. In this thesis, NODDI was first developed for use in a preclinical MRI setting. As animal models present a unique opportunity to study the extremely early stages of mTBI it was first necessary to redevelop this technique from clinical use in humans to rodent use in a preclinical MRI scanner. Once NODDI was validated for pre-clinical use it was then applied in the extremely early stages of a rodent model of mTBI. NODDI was able to detect changes in the neuronal structures of rodents within the first hour of mTBI, representing a potential opportunity to map out these changes over time. Following this successful application, NODDI was applied to a rodent model of repetitive mTBI, a model particularly relevant to sporting situations. Many athletes experience multiple mTBI's over the course of a season and the cumulative effect of these injuries is still unknown. NODDI was able to detect extremely early changes in the brain of rodents after both a first and second mTBI. Further it was shown that some of these changes did not return to normal between the two injuries, potentially providing a window into the changes within the brain.

Co-Authorship Statement

This thesis contains one manuscript that has been published in a scientific journal and two unpublished manuscripts.

Chapter 2 is an original research article entitled "Reproducibility of Neurite Orientation Dispersion and Density Imaging (NODDI) in rats at 9.4 Tesla" and was published in PLOS One in 2019. This manuscript was co-authored by Patrick McCunn, Kyle M. Gilbert, Peter Zeman, Alex Li, Michael J. Strong, Ali R. Khan and Robert Bartha. As first author I contributed to all aspects of the studies as well as manuscript preparation and submission. I contributed to study design, data acquisition, image analysis, database organization, statistical analysis, interpretation, and manuscript preparation. As Principal Investigator and Supervisor, Dr. Robert Bartha was responsible for study conception and design, as well as guidance on data analysis, interpretation, drafting and final revisions and approval of the manuscripts. MRI acquisition was performed by Dr. Alex Li on all studies and animal handling by Miranda Bellyou. Kyle M. Gilbert and Peter Zeman were responsible for hardware development for this study. Michael J. Strong and Ali R. Khan were responsible for supervision and study design.

Chapter 3 is an unpublished research article entitled "Neurite Orientation Dispersion and Density Imaging (NODDI) in a Rodent Model of Early Mild Traumatic Brain Injury (mTBI)". This manuscript was co-authored by Patrick McCunn, Xiaoyun Xu, Alex Li, Arthur Brown, and Robert Bartha. As first author I contributed to all aspects of the studies as well as manuscript preparation and submission. I contributed to study design, data acquisition, image analysis, database organization, statistical analysis, interpretation, and manuscript preparation. As Principal Investigator and Supervisor, Dr. Robert Bartha was responsible for study conception and design, as well as guidance on data analysis, interpretation, drafting and final revisions and approval of the manuscripts. MRI acquisition was performed by Dr. Alex Li on all studies and animal handling by Miranda Bellyou. Xiaoyun Xu assisted in study implementation and data collection. Arthur Brown was responsible for supervision and study design.

Chapter 4 is an unpublished research article entitled "Neurite Orientation Dispersion and Density Imaging (NODDI) in a Rodent Model of Repetitive Mild Traumatic Brain Injury (mTBI)". This manuscript was co-authored by Patrick McCunn, Xiaoyun Xu, Alex Li, Arthur Brown, and Robert Bartha. As first author I contributed to all aspects of the studies as well as manuscript preparation and submission. I contributed to study design, data acquisition, image analysis, database organization, statistical analysis, interpretation, and manuscript preparation. As Principal Investigator and Supervisor, Dr. Robert Bartha was responsible for study conception and design, as well as guidance on data analysis, interpretation, drafting and final revisions and approval of the manuscripts. MRI acquisition was performed by Dr. Alex Li on all studies and animal handling by Miranda Bellyou. Xiaoyun Xu assisted in study implementation and data collection. Arthur Brown was responsible for supervision and study design.

Acknowledgments

For those who know me, you'll know this section is going to be short and to the point.

To my supervisor Dr. Bartha: Thank you for supporting me in the lab and allowing me to pursue a million different shenanigans outside of the lab.

To my committee members, Dr. Khan and Dr Strong: Thank you for the amazing guidance and inspiration along the way.

To lab mates and colleagues at CFMM: Thank you for letting me consistently bounce ridiculous ideas off you and teaching me the wonder of a for loop.

To my Mom: I always told people that anytime I wanted to quit school I reminded myself that you went to school while raising 16-year-old me. If you can do that, I can make it through an exam or two.

To my siblings Chris, Beth, and Jared: I told you I was doing something with myself the last couple years.

To my friends: You know who you are, and I'd rather thank you over a beer than with a few words on pages you may never read.

To Reginald and Leonard: You're the best dog-sons a guy could want.

Table of Contents

List of Tables

List of Figures

List of Appendices

List of Symbols, Abbreviations, and Constants

Symbols and Units

- γ - Gyromagnetic Ratio
- μ - Magnetic Moment
- M – Bulk Magnetization
- T – Tesla

Abbreviations

- AD – Axial Diffusivity
- ADC – Apparent Diffusion Coefficient
- BBB – Blood Brain Barrier
- CCI – Controlled Cortical Impact
- CHARMED - Composite Hindered And Restricted Model of Diffusion
- CNS – Central Nervous System
- DKI – Diffusion Kurtosis Imaging
- dMRI – Diffusion Magnetic Resonance Imaging
- DT – Diffusion Tensor
- DTI – Diffusion Tensor Imaging
- EMF – Electromagnetic Field
- FA – Fractional Anisotropy
- FID – Free Induction Decay
- FT – Fourier Transform
- GE - Gradient Echo
- IsoVF – Isotropic Volume Fraction
- M – Bulk Magnetization
- MD – Mean Diffusivity
- MRI – Magnetic Resonance Imaging
- mTBI – Mild Traumatic Brain Injury
- NDI – Neurite Density Index

- NMR – Nuclear Magnetic Resonance
- NODDI – Neurite Orientation Dispersion and Density Imaging
- ODI – Orientation Dispersion Index
- PD – Proton Density
- PGSE – Pulsed Gradient Spin Echo
- RD – Radial Diffusivity
- RF – Radio Frequency
- SE – Spin Echo
- SNR – Signal-to-Noise Ratio
- T_1 – Longitudinal Relaxation Time Constant
- T_2 – Transverse Relaxation Time Constant
- TAI – Traumatic Axonal Injury
- TBI – Traumatic Brain Injury
- TE – Echo Time
- TR – Repetition Time
- WMTI - White Matter Tract Integrity

Constants

- Boltzmann constant (K) = 1.38 x 10^{23} J/K
- Planck's constant (h) = $6.6 \ x \ 10^{-34}$ J/s
- Proton gyromagnetic ratio (γ) = 2.675 x 10^8 rad/s $\cdot$ T

Chapter 1

1   Introduction

1.1 Background and Motivation

Awareness of the immediate and long-term detrimental effects of mild traumatic brain injury (mTBI) has increased recently. Currently there is no pathognomonic test that allows diagnosis of mTBI and subsequent monitoring of recovery. Clinical assessments focus on self-reported patient symptoms but unfortunately provide little with regard to the underlying biological changes that lead to these symptoms [1–4]. Further, it is nearly impossible to study the immediate (1-2 hours) changes in a clinical setting as patients simply aren't available for study during this time period. Thus, we are left with a vague understanding of the pathological processes taking place in the immediate stages of mTBI. To develop unbiased metrics of mTBI that can inform diagnosis we must understand the underlying metabolic and microstructural features of these injuries.

Currently there are many medical imaging techniques available that can be used to non-invasively image the body. Unfortunately though, most are unable to image mTBI as large scale changes such as expanding epidural hematoma are absent [5,6]. Magnetic resonance imaging (MRI) is ideally suited for imaging the soft tissues within the brain and thus is widely used in the study of mTBI [7,8]. Various MRI techniques have been carefully developed that provide accurate and detailed *in-vivo* information about changes in the structure [9,10], metabolism [11,12], and function [13,14] of the brain due to mTBI. Despite these capabilities, imaging mTBI *in-vivo* is still limited in individual patients due to small physical size and heterogeneous distribution of injury markers in the brain [15]. Moreover, many microstructural abnormalities such as white matter lesions are found in a large percentage of healthy middle-aged individuals, further compounding the difficulty in detection of microstructural changes specific to mTBI [16]. Thus, there is a need to develop techniques that are sensitive specifically to microstructural changes in mTBI. One modality that has been shown to be effective in the detection of

microstructural changes in mTBI is diffusion magnetic resonance imaging (dMRI). dMRI is a powerful magnetic resonance modality that can probe anatomical microstructure and structural connectivity within the normal brain and following injury or pathology [17]. dMRI has been used extensively to study various forms of brain injury including mTBI and has been able to detect alterations in diffusion patterns of water years after initial injury in the clinical setting [18–20], and within 4 hours of injury in the pre-clinical setting [21]. Despite this, no current studies have attempted to use dMRI withing the first hour following an injury. Furthermore, the changes in these metrics have been inconsistent due to the heterogeneous nature of mTBI pathological changes [22–26]. To disentangle these features various advanced biophysical models have been proposed which model the diffusion signal in a biologically relevant form such as the composite hindered and restricted model of diffusion (CHARMED), white matter tract integrity (WMTI), and neurite orientation dispersion and density imaging (NODDI) [27–29].

NODDI is a biophysical model that separates the dMRI signal into three unique compartments termed intra-neurite, extra-neurite and CSF compartments [30]. The intra-neurite compartment is representative of dendrites and axons, while the extra-neurite compartment is comprised of various cell bodies, areas in close proximity to neurons, and glial cells. The CSF compartment is simply the area taken up by freely diffusing water. This model allows detection of neuronal changes separate from changes within the extra-neurite compartment. Thus, NODDI is well situated to image mTBI *in-vivo* in an attempt to understand the various pathological processes taking places in the immediate stages following mTBI.

1.2 Thesis Objectives and Organization

This thesis describes the process by which NODDI has been used to image various pathological changes in mTBI *in-vivo* at 9.4 Tesla in a rodent model of traumatic brain injury (TBI). Contained in this work is the first quantification of the reproducibility of NODDI in a rodent model at 9.4 Tesla, the first time NODDI (or any dMRI technique) has evaluated the temporal changes of diffusion characteristics within the brain of a rodent from hours 1-4 following a mTBI, and the first time the effect of repetitive mTBI

on diffusion characteristics within the rodent brain has been quantified with NODDI (or any dMRI technique) within the first hour of both an initial and secondary mTBI. This thesis requires an understanding of neuroanatomy, mTBI, MRI, dMRI, and NODDI. Therefore, a brief review of the relevant neuroanatomy is described, specifically that needed for the discussion of TBI in chapter 1.3. In chapter 3 the focus will shift to an overview of MRI in isolation followed by a description of diffusion processes and dMRI in chapter 4. Finally, in chapter 5, I will show how dMRI can exploit biophysical models to create a biologically relevant image using NODDI.

The overall objective of this work is to develop Neurite orientation dispersion and density imaging into a viable dMRI technique applicable to detection of subtle microstructural changes in pre-clinical rodent models of mild traumatic brain injury using high field MRI. We hypothesized that NODDI will be sensitive to early microstructural changes in the brain in a rodent model of mTBI. Secondary to this objective, we aimed to determine whether NODDI metrics provided greater sensitivity than standard dMRI metrics to changes in the brain following mTBI in a rodent model. The following provides a summary of the specific objectives contained within each chapter of this thesis.

Chapter 2 characterizes the reproducibility of NODDI in a rodent model at 9.4 Tesla. When this work began, no attempt had been made to determine either the feasibility or reproducibility of obtaining NODDI metrics at 9.4 Tesla in a rodent brain. As ultra-high field MRI presents many unique challenges, such as increased main magnetic field inhomogeneity and physiological artefacts, it was necessary to first determine the reproducibility and the utility (as determined by necessary sample sizes and measurable biological effects) of NODDI in this model.

Chapter 3 presents the first application of NODDI to a pre-clinical rodent model of mTBI at 9.4 Tesla. We hypothesized that NODDI would detect changes in water diffusion indicating changes in the microstructure of the brain within the first 4 hours of mTBI. Further, we hypothesized that NODDI would be more sensitive to these changes than standard DTI metrics.

In Chapter 4 we extend the model of rodent TBI used in Chapter 3 to study the early microstructural changes present in a rodent model of repetitive mTBI. We hypothesized that NODDI would be able to detect water diffusion changes indicating microstructural changes in a rodent model of repetitive mTBI 9.4 Tesla. Furthermore, we hypothesized that these changes would be unique after an initial and secondary mTBI.

Finally, in Chapter 5, the findings of this thesis are summarized and synthesized, particularly the novel contributions of this work to the field. A discussion of the current state of NODDI as a neuroimaging technique to study mTBI in both a clinical and pre-clinical model is also provided. The thesis concludes with a discussion of future directions for this work.

1.3 Neurons and Mild Traumatic Brain Injury

1.3.1 Neurons, Glial Cells, and the Blood Brain Barrier

The Nervous System may be broadly defined as the communication center of a body. Within the nervous system there are two major classes of cells: neurons and glial cells. Neurons process and transmit information within the nervous system in the form of an action potential, enabling communication throughout the body. Glial cells on the other hand provide mechanical and metabolic support to the neurons, amongst various other processes.

Neurons are made up three distinct parts: a cell body (or soma), an axon, and dendrites. The cell body houses the nucleus and associated intra-neurite structures and acts to integrate and organize various input stimuli. The axon and dendrites may be collectively referred to as neurites and are mainly responsible for collecting stimuli from neighbouring neural cells (dendrites) and transmitting signals from the cell body to the synapse (axon). For a more in depth overview of the nervous system please refer to [31].
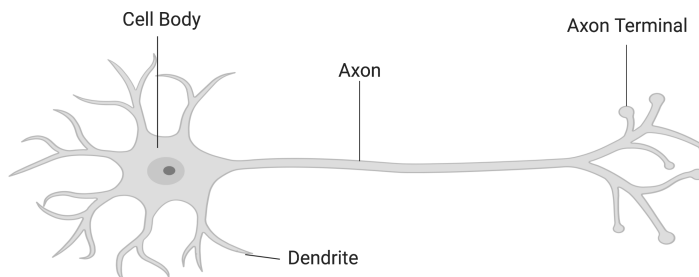
Figure 1.1 - General representation of the neuron including cell body, axon dendrites and axon terminal. Here we term the axons and dendrites collectively as neurites.

Glial cells are largely divided into two categories: microglia and macroglia, the latter of which contains astrocytes and oligodendrocytes. Glial cells reside in the space near neurons and function as the resident immune cells within the brain and act to modulate neurotransmission at the synaptic level [32]. Further, they act to form myelin and insulate neurons, supply nutrients and oxygen to neurons, destroy pathogens, and various other dynamic processes essential to the healthy functioning of the central nervous system [33–35]. Additionally, in many pathological processes such as mTBI, glial cells are essential in mediation of the neuroinflammatory response [36].

In addition to neurons and glial cells, the blood vessels of the CNS possess unique properties which allow highly specific regulation of the movement of molecules, ions, and cells from the vasculature to the brain [37]. Termed the blood brain barrier (BBB), the properties of these blood vessels enable careful maintenance of homeostasis and protection from pathogens and toxins [38]. This control is highly coordinated and responds continuously and dynamically to various chemical and electrical stimuli to protect and support the brain and CNS [39].

1.3.2   Neurons, Glia, and the Blood Brain Barrier during Mild Traumatic Brain Injury

Traumatic brain injury (TBI) refers to a wide variety of damage to the brain caused either directly or indirectly by a sudden impact, generally to the head itself, resulting in the disruption of normal brain function [5]. TBI has a long history of study within the

neuroscience community. However, there is still no pathognomonic test that can be used to accurately diagnose or assess TBI. This is particularly important in mTBI, which lacks obvious pathological presentations during the early phase of injury when decisions regarding treatment and return to play in sport are most critical [40,41]. Many different efforts have attempted to develop diagnostic criteria through observation of the complex cascade of metabolic, physiological, and behavioral effects associated with mTBI, but currently with limited success [42–44]. Current diagnosis relies on patient self-reporting, and qualitative symptom assessment in an effort to manage recovery, which leaves the possibility of unknowingly biased and unreliable assessments [45,46]. Thus, to enable clinicians to offer accurate patient diagnosis and prognosis it is necessary to develop unbiased metrics of mTBI. This thesis attempts to elucidate such metrics by focusing on changes in tissue microstructure that may be associated with alterations to neurons, glia, and the blood-brain barrier in the very early phase of mTBI.

There are many changes to neurons that have been shown to accompany mTBI. The most common is neuronal cell death [47], but many others have been observed such as axonal beading [48], and demyelination and remyelination [49]. Each of these processes has been shown in various stages and to various degrees in mild traumatic brain injury [50–55]. Further, axonal beading and swelling has been shown to occur within the first hour of injury, albeit in varied models and to our knowledge not yet in a closed head model of mTBI [56,57]. Unfortunately, it is still unclear what effect these processes have in terms of assessing the severity of mTBI and subsequent recovery.

In addition to neuronal changes, glial cells are known to act in both a neuroprotective and neurodegenerative manner over the course of injury and recovery in mTBI [58]. Following injury, microglia undergo morphological changes which can produce neuroprotective factors and coordinate neurorestorative processes or can become dysregulated and produce pro-inflammatory and cytotoxic mediators that hinder repair [59]. Astrocytes respond to mTBI by undergoing reactive astrogliosis which aims to limit tissue damage and restore homeostasis, but may also inhibit adaptive neural plasticity mechanisms underlying recovery [60,61]. Oligodendrocytes are uniquely vulnerable to damage under pathological processes and show various patterns of apoptosis and

dysfunction following mTBI [62–65]. Further, in the acute inflammatory phase BBB disruption and leakage takes place contributing to infiltration of blood-borne leukocytes, blood plasma proteins, and macrophages [66–68]. BBB disruption can occur within minutes following mTBI [69–71], with various neuroinflammatory processes occurring within several hours if initial injury [72,73].

Despite the importance of these pathological processes in mTBI, much of our current knowledge is confined to *ex-vivo* histological samples leaving a gap in our knowledge of the dynamic properties of neurites, glial cells, and the blood brain barrier. As NODDI's biophysical model separately quantifies the changes in neurite volume and orientation, this technique is well suited to detect and monitor the progression of changes in neurite structure *in-vivo* in mTBI. Further, neuroinflammatory processes and blood brain barrier disruption would take place within the extra-neurite compartment, once again allowing this technique to provide a detailed *in-vivo* look at the dynamic processes taking place in mTBI. Finally, as NODDI allows *in-vivo* imaging by which we might detect various dynamic changes within the neural microstructure, careful study of the immediate effects of mTBI on neurons, glia and the blood barrier to injury is possible. This in turn could lead a more thorough understanding of the nervous system's response to mTBI and potential interventions to improve patient recovery and outcomes.

1.4 MRI – Nuclei, Magnetization, and Avoiding Quantum Mechanics

All discussions of MRI must first begin with the discussion of the phenomenon of nuclear magnetic resonance (NMR). While the bulk properties of MRI take place on a macroscopic level and are thus well explained in the realm of classical physics, it is important to understand (in brief) the basis of the quantum mechanical description of NMR and how we extend this description into the realm of classical physics. Thus, this first chapter begins with a brief description of the quantum mechanical properties of nuclei and magnetization and transitions into a discussion of bulk magnetization and manipulation of particle ensembles to generate a measurable NMR signal for use in MRI.

All discussions and derivations in this chapter rely heavily on those presented in references [74–77].

1.4.1   Brief Description of "Spin"

All atomic and sub-atomic particles possess an intrinsic property known as spin angular momentum, or simply spin. This quantum mechanical property is highly analogous to the classical property of the angular momentum of a sphere rotating about some axis. There are several distinctions though to be made: spin is an intrinsic property of a particle and quantized in discrete states. It does not, in fact, represent the physical motion (rotation) of the particle in question.

1.4.2   Spin and the Magnetic Moment I – Quantum Mechanics

Individual particle spin is a quantum mechanical phenomenon. Spinning charge produces a magnetic field and thus a magnetic moment $\vec{\mu}$ in the direction of $\vec{J}$ (the angular momentum of the proton) such that:

$$\vec{\mu} = \gamma \cdot \vec{J} \tag{1}$$

Here γ is the gyromagnetic ratio, a proportionality constant dependent upon the nucleus. For hydrogen (particularly relevant in MRI),

$$\gamma = 2.675 \ x \ 10^8 \ rad/s \cdot T \tag{2}$$

The hypothetical measurement of a single spin relies on a quantum mechanical description of angular momentum such that

$$J = \hbar\sqrt{I(I+1)} \tag{3}$$

Where I is the spin quantum number of the nucleus and may only take on discrete half integer values (I = 0, 1/2, 1, 3/2, …), $\hbar = h/2\pi$, and $h = 6.6 \ x \ 10^{-34} \ Joule/s$ (Planck's constant). Thus, by quantum mechanics, the magnitude of the magnetic moment of a particle is simply a constant:

$$\mu = \gamma \hbar \sqrt{I(I+1)} \qquad (4)$$

For MRI, and particularly diffusion weighted MRI, we generally focus solely on hydrogen nuclei that possess a spin quantum number $I = \pm 1/2$. Therefore, we find for the hydrogen nucleus, there are two distinct energy states:

$$J = \pm \hbar \sqrt{3}/2 \qquad (5)$$

$$\mu = \pm \gamma \hbar \sqrt{3}/2 \qquad (6)$$

We say spin energy is quantized as only one of these two states may be observed for a single spin at a single moment in time.

Without influence from external factors, the orientation of the magnetic moment is random. However, interaction of the magnetic moment $\vec{\mu}$ with a magnetic field $\vec{B}$ will cause $\vec{\mu}$ to precess around $\vec{B}$ such that the torque on the particle is defined as:

$$\vec{\tau} = \vec{\mu} \times \vec{B} \qquad (7)$$

This is true for each individual particle within the field. The torque may also be described by Newtons Second Law as the time rate of change of the angular momentum:

$$\frac{d\vec{J}}{dt} = \frac{1}{\gamma}\frac{d\vec{\mu}}{dt} \qquad (8)$$

Therefore, we obtain the following equation of motion for a spin in a magnetic field:

$$\frac{d\vec{\mu}(t)}{dt} = \gamma \vec{\mu}(t) \times \vec{B}(t) \qquad (9)$$

The precessional frequency of the magnetic moment induced by the magnetic field, known as the Larmor Frequency is defined as:

$$\omega_0 = \gamma B_0 \qquad (10)$$

Further to this discussion, the quantization of energy tells us that the magnetic moment of a proton in an external magnetic field may be measured in only one of two states. The magnetic moment may precess around an axis parallel to the main magnetic field (known as the "spin up" state) or the magnetic moment may precess around an axis antiparallel to the main magnetic field (known the "spin down" state). While both states occur naturally, the spin up is at a lower energy state to the spin down, and thus preferentially populated. The distribution of the nuclei into these states will be discussed later and is governed by Boltzmann statistics.

Thus, we see the basis for the origin of the magnetic moment due to spin angular momentum and its interaction with an external magnetic field in terms of quantum mechanics. This description of the magnetic moment is essential to understanding the basis of MRI, but the use of quantum mechanics is only necessary to this point. While a single nuclear spin is governed by these properties, a large ensemble of these spins may be accurately described by classical mechanics. In a typical imaging voxel within an MRI experiment, the number of individual water protons, or spins, is on the order of 10^{19}. The use of quantum mechanics is not only unnecessary when dealing with the scales of MRI, it becomes impractical. This allows the departure from the rigorous quantum mechanical description of single particle spins, into the classical realm of an ensemble of these spins known as bulk magnetization, $\vec{M}$.

1.4.3   Spin and the Magnetic Moment II – Classical Description

With the quantum mechanical description of spins in an external magnetic field described, we now move to a more relevant discussion in MRI imaging: Bulk Magnetization ($\vec{M}$). $\vec{M}$ is simply defined as the total magnetic moment of an ensemble of N spins such that:

$$\vec{M} = \sum_{i=1}^{N} \vec{\mu_i}$$

(11)

As discussed earlier, individual spins in an external magnetic field may take on one of two measured states: spin up or spin down, with the spin up state being the lower energy state. The population distribution of these states takes on the form of the Boltzmann distribution:

$$\frac{N_\uparrow}{N_\downarrow} = e^{-\Delta E/KT} \approx 1 + \frac{\gamma \hbar B_0}{KT} \tag{12}$$

Here $K = 1.38$ x 10^{23} J/K is the Boltzmann constant and ΔE is the energy difference between the spin up and spin down states known as the Zeeman energy:

$$\Delta E = E_\downarrow - E_\uparrow = \gamma \hbar B_0 \tag{13}$$

Noting M will simply be the difference of magnetization resulting from spin-up magnetic moments and spin-down magnetic moments, we arrive at:

$$\vec{M} \approx \frac{\gamma^2 \hbar^2 N_\downarrow B_0}{4KT} \hat{z} \tag{14}$$

Thus, we find that the statistical distribution of an ensemble of spins placed in an external magnetic field will produce a net magnetization vector $\bar{M}_z(t)$ aligned in the direction of the external magnetic field, $\vec{B}_0 = \vec{B}_0 \hat{z}$. This net magnetization, $\bar{M}_z(t)$, is said to precess about the main magnetic field, $\vec{B}_0 = \vec{B}_0 \hat{z}$, according to the following equation of motion, known as the Bloch Equation [78]:

$$\frac{d\vec{M}(t)}{dt} = \gamma \vec{M}(t) \times \vec{B}(t) \tag{15}$$

This vector may be described by classical mechanics and is no longer quantized into discrete energy states (ie. it may now take on any orientation in three dimensions). From this point on all discussions of magnetization refer simply to this bulk magnetization, and no longer individual magnetic moments.

Equation (15) can be rewritten in terms of individual components:

$$\frac{dM_z(t)}{dt} = 0 \tag{16}$$

$$\frac{dM_x(t)}{dt} = \gamma M_y(t) B_z(t) \tag{17}$$

$$\frac{dM_y(t)}{dt} = \gamma M_x(t) B_z(t) \tag{18}$$

The solutions to these equations become:

$$M_z(t) = C \tag{19}$$

$$M_y(t) = M_x \cos(\omega t) + M_y \sin(\omega t) \tag{20}$$

$$M_y(t) = M_y \cos(\omega t) - M_x \sin(\omega t) \tag{21}$$

Where C is a constant. In other words, in the presence of an external magnetic field, $\vec{B}_0 = \vec{B}_0 \hat{z}$, the longitudinal component of the magnetization (M_z) is simply constant while the transverse components (M_x and M_y) vary sinusoidally around the main magnetic field.

1.4.4   The Bloch Experiments

The Bloch equations derive their name from Felix Bloch who's experiments represented a landmark in NMR and MRI development [79]. Bloch and his colleagues were able to detect the transverse component of the signal by placing a receiver coil such that magnetic flux through the coil was at a right angle to the main magnetic field (B_z) and measuring the small electrical current generated in this coil. Additionally, Bloch *et al.* followed this experiment by perturbing the magnetization with a second constant magnetic field (B_1) at right angles to the main magnetic field. He found that this caused a transient measurable electrical signal in the receiver coil, that decayed at a rate specific to the individual material being studied. It was reasoned that the individual spin magnetic

moments were interacting with each other and with their environment, causing the system to release energy in a process termed relaxation.

1.4.5   Relaxation Time Constants

Felix Bloch defined two relaxation time constants; the spin-lattice and spin-spin relaxation time constants. These are denoted T_1 and T_2 respectively. T_1 describes the rate at which the longitudinal component (ie $M_z(t)$) approaches its equilibrium value of magnetization M_0, while T_2 describes the rate at which the magnetization component orthogonal to the main field (ie $M_{xy}(t)$) decays. Further to these, a time constant, T_2^*, describes the rate at which the magnetization component orthogonal to the main field decays including the effect of local inhomogeneities in the main magnetic field. These time constants are largely dependent on the molecular environment as well as magnetic field strength and temperature. Inclusion of the relaxation terms above modify equation (15) such that we have:

$$\frac{d\vec{M}(t)}{dt} = \gamma\vec{M}(t) \times \vec{B}(t) - R(\vec{M}(t) - M_0) \tag{22}$$

Where R is the relaxation matrix represented by:

$$\begin{pmatrix} 1/T_2 & 0 & 0 \\ 0 & 1/T_2 & 0 \\ 0 & 0 & 1/T_1 \end{pmatrix} \tag{23}$$

1.4.6   The Bloch equations

The behaviour of the bulk magnetization M in a static magnetic field $\vec{B}_0 = \vec{B}_0\hat{z}$ with relaxation terms can now be described. Equation (22) can be rewritten in terms of individual components as follows:

$$\frac{dM_z(t)}{dt} = \gamma\left[M_x(t)B_y(t) - M_y(t)B_x(t)\right] - \frac{M_z(t) - M_0}{T_1} \tag{24}$$

$$\frac{dM_x(t)}{dt} = \gamma\left[M_y(t)B_z(t) - M_z(t)B_y(t)\right] - \frac{M_x(t)}{T_2} \tag{25}$$

$$\frac{dM_y(t)}{dt} = \gamma\left[M_z(t)B_x(t) - M_x(t)B_z(t)\right] - \frac{M_y(t)}{T_2} \tag{26}$$

These equations are derived in the cartesian coordinate system, or what is commonly referred to as the "laboratory reference frame". It turns out that since the magnetization is constantly precessing at the Larmor frequency in the transverse plane, defining a "rotating reference frame" simplifies the required mathematics. Replacing $B_z(t)$ by $B_{z\_eff}(t) = B_z(t) + \Omega/\gamma$, where Ω is the angular frequency of the rotating frame, we transform the above magnetization equations into the rotating reference frame:

$$\frac{dM_z(t)}{dt} = \gamma\left[M_x(t)B_y^r(t) - M_y(t)B_x^r(t)\right] - \frac{M_z(t) - M_0}{T_1} \tag{27}$$

$$\frac{dM_x(t)}{dt} = -B_{z\_eff}(t)M_y(t) - \gamma M_z(t)B_y^r(t) - \frac{M_x(t)}{T_2} \tag{28}$$

$$\frac{dM_y(t)}{dt} = -\gamma M_z(t)B_x^r(t) + B_{z\_eff}(t)M_x(t) - \frac{M_y(t)}{T_2} \tag{29}$$

Note B^r refers to the components of the magnetic field defined in the rotating reference frame. For the remainder of this chapter all equations and derivations will occur in this rotating frame unless explicitly stated otherwise.

1.4.7   RF Pulses

Up to this point we have discussed magnetic moments, bulk magnetization, and their behaviour in the presence of a static magnetic field. But how does this lead to an MR signal? To generate a usable signal, we must manipulate the magnetization using specific radiofrequency (RF) pulses. These, radiofrequency pulses can cause the magnetization to

be "rotated" into the transverse plane where, due to Faraday's Law, can then induce a measurable signal in a nearby coil.

While there are countless different RF pulse types used in NMR and MRI, we will illustrate the simplest example of the effect of a single sinc RF pulse that has a duration much less than that of T_1 and T_2. If this RF pulse is applied along the x axis in the rotating frame equations ($(27$ - (29) now become:

$$\frac{dM_z(t)}{dt} = -M_y(t)\gamma B_x^r(t) \tag{30}$$

$$\frac{dM_x(t)}{dt} = 0 \tag{31}$$

$$\frac{dM_y(t)}{dt} = -M_z(t)\gamma B_x^r(t) \tag{32}$$

The solutions to these equations are given by:

$$M_z(t) = M_0 \cos(\omega_x t) \tag{33}$$

$$M_x(t) = 0 \tag{34}$$

$$M_y(t) = M_0 \sin(\omega_x t) \tag{35}$$

Where the ω_x represents the frequency of rotation about the x-axis. If we denote $\alpha = \omega_x t$ we may generate a general matrix form for the magnetization in all three dimensions generated by an RF-pulse directed along the x-axis in our rotating frame:

$$\begin{bmatrix} M_x(t) \\ M_y(t) \\ M_z(t) \end{bmatrix} = \begin{bmatrix} 1 & 0 & 0 \\ 0 & \cos(\alpha) & -\sin(\alpha) \\ 0 & \sin(\alpha) & -\cos(\alpha) \end{bmatrix} \begin{bmatrix} 0 \\ 0 \\ M_0 \end{bmatrix} \tag{36}$$

Thus when $\alpha = 90°$, $M_x(t) = 0$, $M_z(t) = 0$, and $M_y(t) = M_0$. While this is an extremely simplistic example, it helps to illustrate the potential to manipulate the bulk magnetization of an ensemble of spins placed in an external magnetic field.

1.4.8   Signal Detection

According to Faraday's Law of induction, a time varying magnetic field will generate a current in a surrounding wire. This is the basis of all NMR and MRI signals. Similar to the original Bloch experiment, receiver coils are placed such that the magnetic flux through the coil is at a right angle to the main magnetic field (B_z). As the magnetization vector is rotated from the longitudinal to the transverse plane and subsequently relaxes, the magnetic flux through the coil changes and we can measure the current induced. For a given magnetic field in the laboratory frame:

$$\overrightarrow{\Phi}_B = \int_{coil\ area} \vec{B}(\vec{r}) \cdot \vec{M}(\vec{r},t) d\vec{r} \tag{37}$$

where Φ_B is the magnetic flux through the coil, $B(r)$ is the magnetic field in the laboratory frame and $M(r,t)$ is the bulk magnetization vector. The voltage generated from this process is

$$V(t) = \frac{-d\Phi_B}{dt} \tag{38}$$

Thus, we can see how perturbing the magnetization vector induces a measurable electrical signal in the surrounding receiver coils.

1.4.9   FID

Once the magnetization has been rotated into the transverse plane due to excitation from an RF pulse, this magnetization may now be detected due to the voltage it produces in the receiver coil as described above. In most MR experiments the signal will take a form of a free induction decay (FID) described by:

$$s(t) = \int_{coil\ area} \vec{M}_{xy}(\vec{r},t) e^{-i\omega(\vec{r},t)} d\vec{r} \tag{39}$$

where M_{xy} is the transverse magnetization, r is the vector in Cartesian space, and $\omega(r, t)$ is the frequency in our rotating frame.

1.4.10 Spatial Localization I – Slice Selection

We have shown how to manipulate the bulk magnetization to produce a measurable electrical signal by using RF pulses. The next step is to spatially encode the bulk magnetization to generate a usable image. This is accomplished using additional magnetic fields, known as gradients, to vary the z-component of the magnetic field strength along the different axes. Mathematically these gradients are defined as:

$$G_z = \frac{\partial B_z}{\partial z}, G_x = \frac{\partial B_z}{\partial x}, G_y = \frac{\partial B_z}{\partial y} \tag{40}$$

Of particular importance is the effect the gradient has on the spins at a given position. Applying a gradient will increase or decrease the total magnetic field strength at a particular position within the laboratory frame according to the following equation:

$$B(i) = B_0 + i \cdot G_i \tag{41}$$

where i is either the x, y, or z dimension in scanner space. This change in magnetic field strength alters the Larmor frequency with the new frequency being spatially defined according to the position relative to the gradient:

$$f(i) = \frac{\gamma}{2\pi}(B_0 + iG_i) \tag{42}$$

This allows the selective excitation of nuclei using band limited RF pulses. For example, if we apply the gradient described above, the Larmor frequency varies linearly along an axis (usually $\hat{z}$). Therefore, we may "tune" our RF pulse such that we specifically excite certain slabs, known as slices, along the length of the longitudinal axis. Using carefully designed pulse sequences, the user may control the position, shape, and width of each slice.

1.4.11   Spatial Localization II – In-plane localization

In-plane localization relies on two distinct gradients referred to as the phase-encoding gradient and the frequency-encoding gradient. These gradients induce a temporary change in the resonant frequencies of excited nuclei that in turn causes a phase shift in the rotating reference frame given by:

$$\emptyset = -\gamma G t \qquad (43)$$

We apply this principle in two dimensions after our slice selective excitation, allowing us to localize our signal within a slice.

First, in our "phase encode" direction a gradient is applied perpendicular to our main magnetic field causing a spatially dependent increase in the precessional frequency of the nuclei along the phase encode axis (Time A in Figure 1.2 below). After the gradient is removed (Time B), the nuclei return to their initial frequency but with various phase shifts, dependent on their position along the phase encode axis. In Figure 1.2 the phase encode axis has been depicted to be the y-axis in the rotating frame and the gradient strength is represented vertically. These nuclei are now said to be "phase encoded" and will maintain this phase shift until further gradients are applied or the MR signal decays. This process is repeated for varied phase encode gradient strengths to sample as many possible spatial frequencies within a given image.
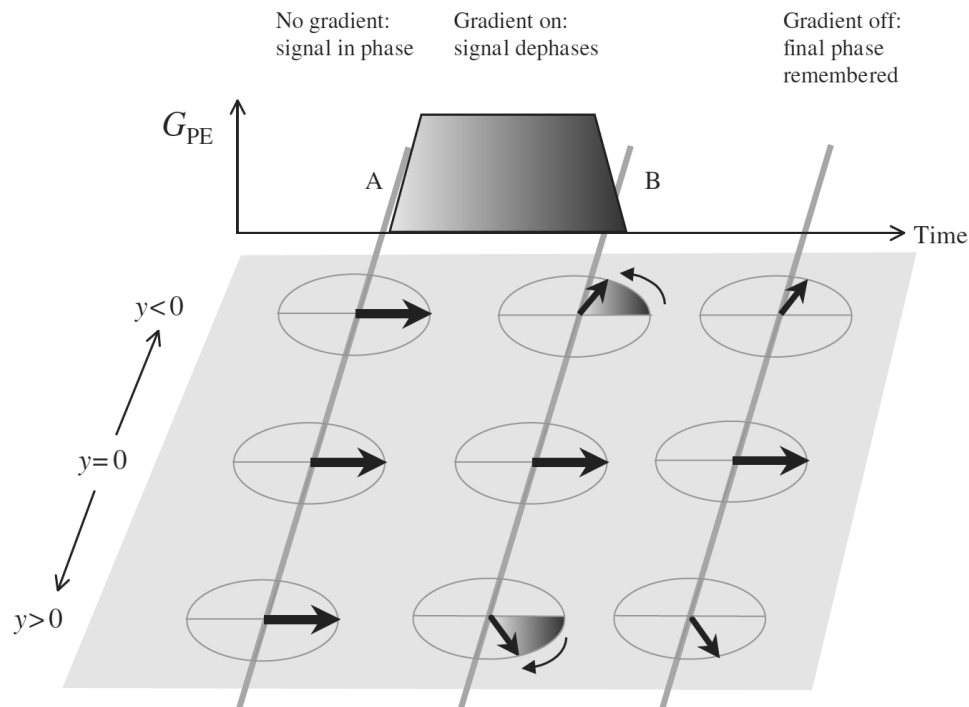
Figure 1.2 - Illustration of phase encoding for spatial localization in the MR signal. At time A the phase encode gradient is applied leading to attenuation of the precessional frequency of the spins. Once the gradient is removed (time B), the spins return to their original frequency but with a spatially dependent phase shift. Thus, these spins are now phase encoded. Figure reproduced with permission from Picture to Proton.

Finally, we apply a frequency encode gradient, perpendicular to the phase encode gradient. During the measurement of our signal the frequency encode gradient causes an accumulated phase shift dependent on the nuclei position on the frequency encode axis. This gradient is often referred to as our "readout gradient" as it is applied during the acquisition of our signal. If we sample our received complex signal in quadrature at discrete time intervals, we can recover both this phase and frequency. Thus, each data point represents a different "amount" of frequency encoding and corresponds to a different spatial frequency. By sampling this way, we can collect all the spatial frequencies in the frequency encode direction with a single RF excitation.

1.4.12 Fourier Transform and K-space

When we measure the signal from our sample, we obtain a sinusoidal combination of all the sampled spatial frequencies over the course of a given excitation. By Fourier theory this signal can be decomposed into individual parts each representing a unique spatial frequency. We store this information in k-space. k-space is simply our raw data space where each data point represents a unique spatial frequency and the magnitude (brightness) of the point represents the relative contribution of that spatial frequency of nuclei to the resulting image.
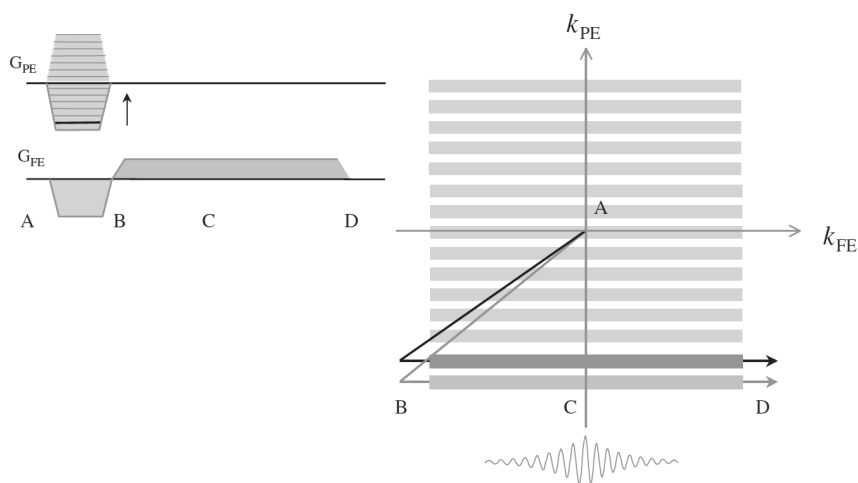
Figure 1.3 – Illustration of the k-space trajectory produced by the combination of phase encoding and frequency encoding used for spatial localization in MRI. Figure reproduced with permission from Picture to Proton.

Figure 1.3 shows how our phase encode (G_{PE}) and frequency encode (G_{FE}) gradients allow us to "traverse" k-space. Immediately after our excitation RF pulse, we begin at the center of k-space (Point A), which represents the total signal irrespective of location. Generally, we store the signal in 2-dimensional Fourier space, where the axes (k_{PE}, and k_{FE}) represent the spatial frequencies in the phase encode and frequency encode directions of the image. We first move to a position along our k_{PE} by applying a phase encode gradient, and then sample along this line varying our position on the k_{FE} axis through application of a frequency encode gradient (from points B-D). This process is repeated for a set number of phase-encode steps to "fill" k-space. From k-space one may

apply a Fourier transform to reconstruct the k-space data back into a recognizable image as shown in Figure 1.4.
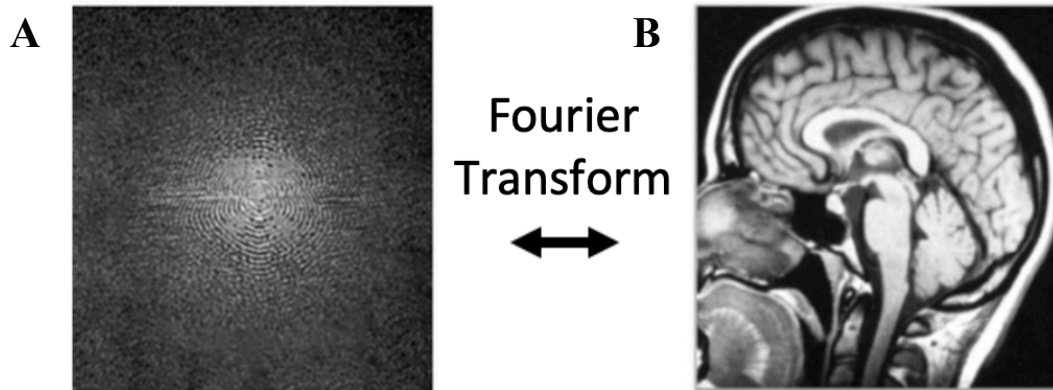
Figure 1.4 - A) Representation of the combination of all spatial frequencies obtained from a given MR signal in k-space. B) MR image reconstructed by Fourier transform from the shown k-space data. Image reproduced courtesy of Allen D. Elster, MRIquestions.com.

1.4.13   Spin Echo Pulse Sequence

While there are countless pulse sequences and variations of pulse sequences, most pulse sequences fall into two categories; spin echo or gradient echo pulse sequences. To illustrate these pulse sequences, we use pulse sequence diagrams. On the vertical axis we represent gradient or signal strength and the horizontal axis represents time. In a spin echo pulse sequence (also known as Hahn Spin Echo [80]), two pulses are used, commonly a 90° excitation pulse followed by a 180° refocusing pulse. The first pulse tips the magnetization into the transverse plane (also known as excitation). Once in the transverse plane the individual spins tend to precess at different rates due to magnetic field inhomogeneities. By applying a 180° refocusing pulse those spins that precess faster will be reordered and are now behind. At some time, known as the Echo Time (TE), these spins will eventually catch up, forming a coherent signal known as an echo. We will find later that this pulse sequence is the backbone of the NODDI pulse sequence used in this thesis.
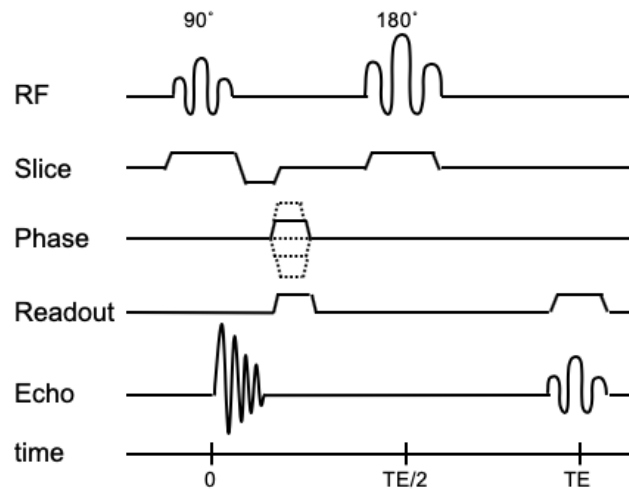
Figure 1.5 – Representative spin echo pulse sequence diagram. In the spin echo pulse sequence, a 180° refocusing pulse is used to invert the spins in the transverse plan, leading to rephasing known as an echo.

1.4.14   Gradient Echo Pulse Sequence

In a gradient pulse sequence, we apply a dephasing gradient along the frequency encode axis to speed up the dephasing of the spins in the transverse plane. To create a measurable echo, we then apply a gradient of opposite polarity and equal magnitude (termed a rephasing gradient), causing the spins to rephase and create our echo. By applying these gradients, we may speed up the formation of our echo as opposed to the spin echo pulse sequence, and thus gradient echo sequences form the basis of many rapid imaging techniques [81].
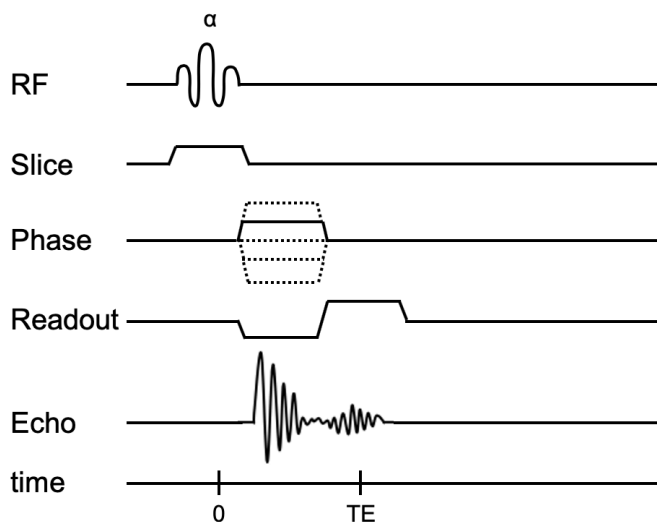
Figure 1.6 – Representative gradient echo pulse sequence diagram. In the gradient echo pulse sequence, a dephasing and rephasing gradient of equal and opposite polarity is used to rapidly create an echo in our signal.

1.5 Diffusion and MRI

To this point, we have briefly described how an image is generated by manipulating protons of the water molecule with various magnetic fields and RF pulses. In this section we show how we may further manipulate the MR signal to measure how water moves within biological tissue. By doing this we are able infer various microstructural components of the brain and gain greater insight into the structural basis of brain function. In this section, a brief background of diffusion in biological tissues will first be introduced followed by the technical aspects and implementation of diffusion weighted MRI (dMRI).

1.5.1   Introduction to Diffusion and Diffusion Weighted MRI (dMRI)

This section will cover the basics of diffusion in a biological context. Much like relating the quantum mechanical description of magnetic moment to the bulk magnetization, we begin by giving a brief description of the microscopic properties of diffusion. However, within the context of MRI, the diffusion of water in tissue can be adequately explained on the macroscopic level and the need for the complex mathematics associated with

microscopic diffusion can be largely ignored. First the phenomenon of diffusion will be discussed and then diffusion will be related to the previous discussion of MRI to show how to produce image contrast related to diffusion in a biological medium.

1.5.2   The Microscopic Description of Diffusion – Brownian Motion

Diffusion by definition is the motion of molecules in a random pattern due to thermal motion. This process is also known as Brownian motion, named after Robert Brown, who published his observations in an 1827 paper of the apparently random motion of pollen grains immersed in a fluid medium [82]. While Brown discussed these observations, the exact mathematical description of these interactions may not be solved analytically. Similar to the previous description of spins in a magnetic field, when discussing ensembles of particles in a fluid medium, statistical methods can be used to bridge the gap from the microscopic to the macroscopic and provide a mathematical solution to macroscopic diffusion.

1.5.3   Macroscopic Diffusion in an Isotropic Environment

In 1855, Adolf Fick began to describe the phenomenon of diffusion, on a macroscopic scale, based on the concepts of flux and concentration gradients [83]. His first law states that particle flux J, in an isotropic fluid medium, will be directed from areas of high concentration to low concentration and will be proportional to the concentration of particles in the medium at a given point in space. Mathematically stated:

$$\vec{J} = -D\vec{\nabla}n(r, t) \tag{44}$$

Here $n(r, t)$ is the concentration of particle at position r and time t and D is simply a scalar value describing the rate of diffusion in the given medium. As the medium is isotropic, D is the same in all directions. Fick's second law uses conservation of mass to predict how diffusion will lead to concentration changes over time giving:

$$\frac{\partial n}{\partial t} = D\nabla^2 n \tag{45}$$

Here concentration changes $(\partial n / \partial t)$ within a volume are proportional to the second derivative of the concentration gradient $(\vec{\nabla}^2 n)$ and the diffusivity (D).

In 1905, Einstein described the observations made by Brown and Fick, using the random walk model (ie. a stochastic process) [84] leading to a mathematical framework to describe Brownian Motion. In this model, a path is described as a series of successive steps on a Cartesian grid and a step is defined as a move from one grid point to another and each possible step is weighted with equal probability. For example, in Figure 1.7 A) below, a two-dimensional random walk model is shown where each possible step has probability p = 1/4. As the number of steps grows, the end points for each successive run tends towards a Gaussian distribution. This is known as isotropic diffusion and the probability of finding a particle at a given point in space and time can be solved mathematically. This same situation is further shown Figure 1.7 B) in three dimensions where each step has probability p=1/8 (cube).

Consider first an ensemble of particles in an isotropic medium. The probability density $P(\vec{R}, t)$, that a particle will move distance, $\vec{R}$, in some time, t, can be computed by solving:

$$\frac{\partial P(\vec{R}, t)}{\partial t} = D \nabla^2 P(\vec{R}, t) \tag{46}$$

The solution to this equation, commonly now known as the ensemble average propagator (EAP) or diffusion propagator, is simply a Gaussian distribution [84]:

$$P(\vec{R}, t) = \frac{1}{(4\pi Dt)^{3/2}} e^{-\frac{\|\vec{R}\|^2}{4Dt}} \tag{47}$$

where D is the diffusion coefficient, D represents a measure of the squared particle displacement over time. In the isotropic medium described here, the diffusion coefficient is independent of direction, which is the definition of isotropic diffusion.

In the biological context the diffusion coefficient is experimentally determined and based on the mass of the molecule and the temperature and viscosity of the medium. For water

molecules diffusing in water at 37°C, the diffusion coefficient has been determined to be $3x10^{-9}m^2/s^2$ [87]. Therefore in 50 ms, approximately 32% of the water molecules will have moved 17 μm. whereas only 5% of them have travelled over distances greater than 34 μm. [88].
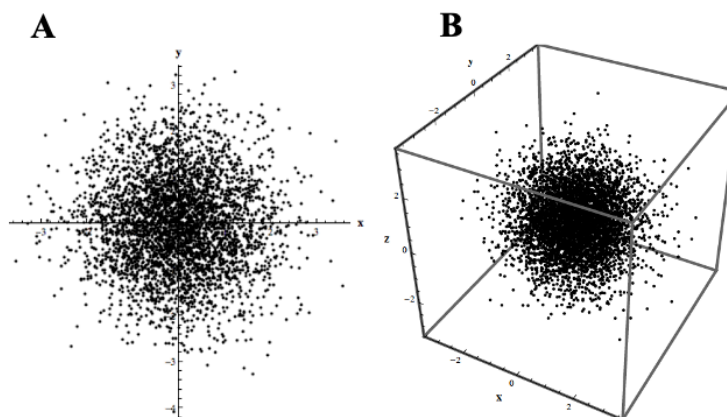
Figure 1.7 – Illustration of a random walk in A) 2-dimensions and B) 3-dimensions. In each image a single particle was allowed to diffuse freely according to the random walk model with n=100 steps and A) p=1/4 from the origin or B) p=1/8. The resulting point clouds show the endpoints for the diffusion of a particle after 1000 successive trials tending toward Gaussian isotropic diffusion. Reproduced with permission of Frank R. Lawrence from The Principles of Diffusion Tensor Imaging [77].

1.5.4   Macroscopic Diffusion in an Anisotropic Environment

In the previous illustration, diffusion was in a purely isotropic medium, with no barriers present. This situation is rarely found in a biological medium, as barriers are generally present and rarely are there purely homogenous environments. Examples of barriers relevant to diffusion imaging include cell membranes and axonal fibres due to the associated timescales of the diffusion measurement (which we will find later to be approximately 50-100 ms and will be discussed in 4.7) [89]. When such barriers are present, diffusion will predominantly occur in a direction perpendicular to the barrier. Einstein's relation may be extended in these cases to describe the directional variations in diffusion by:

$$\underline{D} = \begin{bmatrix} D_{xx} & D_{xy} & D_{xz} \\ D_{yx} & D_{yy} & D_{yz} \\ D_{zx} & D_{zy} & D_{zz} \end{bmatrix} \qquad (48)$$

$\underline{D}$ is now defined by the diffusion tensor, representing anisotropic diffusion. This tensor is a positive definite, symmetric ($\underline{D}^T = \underline{D}$) tensor. Otherwise stated this tensor allows us to mathematically describe diffusion with directional dependence, known as anisotropic diffusion.
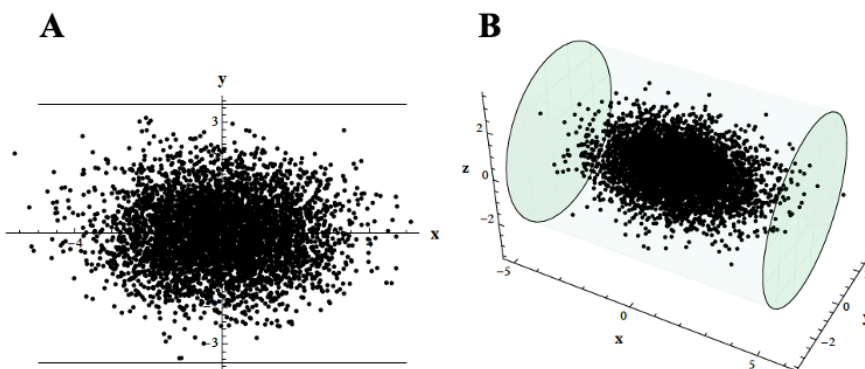
Figure 1.8 - Illustration of a random walk with hypothetical barriers present in A) 2-dimensions and B) 3-dimensions. In each image a single particle was allowed to diffuse freely according to the random walk model with n=100 steps and A) p=1/4 from the origin or B) p=1/8. The resulting point clouds show the endpoints for the diffusion of a particle after 1000 successive trials tending towards anisotropic diffusion. Reproduced with permission of Frank R. Lawrence from The Principles of Diffusion Tensor Imaging [77].

1.5.5   Diffusion NMR and the Bloch-Torrey Equations

Until now, the phenomenon of diffusion has not been related to the diffusion measurement made by MRI. The Bloch equations described earlier do not account for the effects of the diffusion of water on the magnetization vector, and consequently do not provide a basis for the measurement of water diffusion in tissue by MRI. Early experiments in NMR provided the basis for diffusion weighted MRI. In 1956, H.C. Torrey accounted for the effects of diffusion in an NMR experiment, producing what is known as the Bloch-Torrey equation [90]:

$$\frac{d\vec{M}}{dt} = \vec{M} \times \gamma B_{eff} - \frac{M_x\vec{\imath} + M_y\vec{\jmath}}{T_2} - \frac{(M_z - M_0)\vec{\imath}}{T_1} + \vec{\nabla} \cdot (D\vec{\nabla}\vec{M}) \tag{49}$$

This equation describes the time evolution of the transverse magnetic field incorporating the effect of diffusion of water in a biological medium.

1.5.6   Stejskal-Tanner: The PGSE and b-value

In 1965 Stejskal and Tanner introduced the Pulsed Gradient Spin Echo (PGSE) sequence to measure the diffusion coefficient D [91]. The sequence is diagrammed in Figure 1.9 and based on the spin echo pulse sequence described previously. Important to note are two quantities unique to the PGSE and essential for diffusion measurements: δ, the diffusion gradient duration and Δ, the duration between the two diffusion gradients. In this pulse sequence, two diffusion gradients are placed symmetrically on either side of the 180° refocusing pulse. The phase change induced by the first gradient will be:

$$\emptyset_1 = -\gamma(\delta G)x_1 \tag{50}$$

where x_1 indicates the position of the particle as the diffusion gradient is applied and G is simply the gradient strength. The phase change during the second pulse is:

$$\emptyset_2 = -\gamma(\delta G)x_2 \tag{51}$$

where x_2 is the new position of the particle.
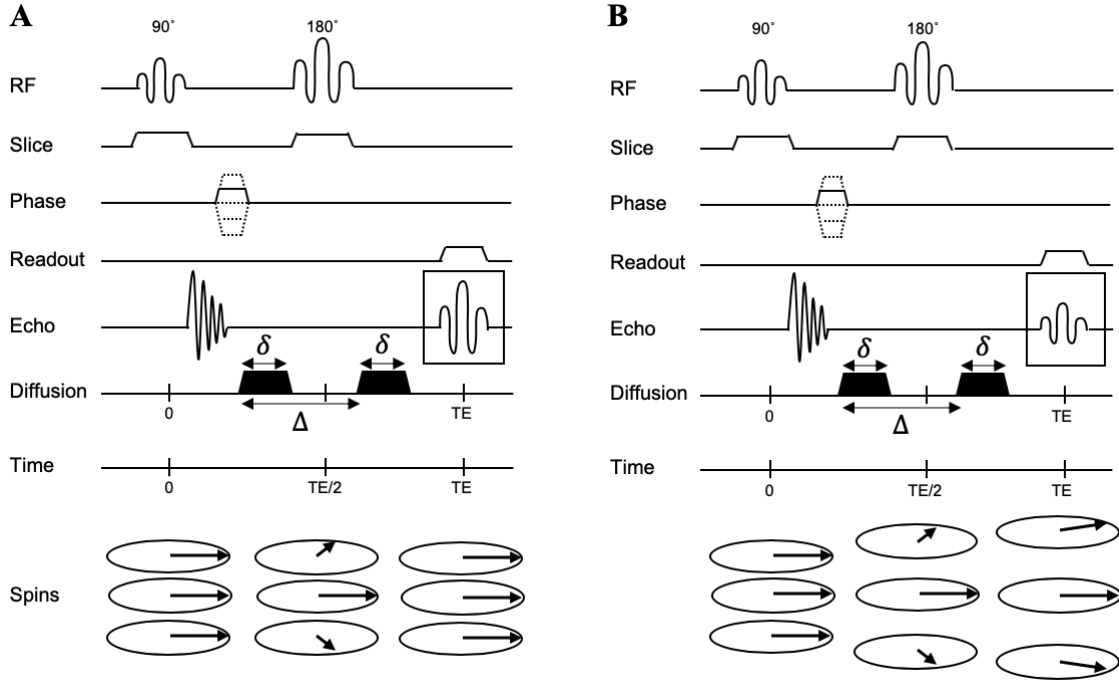
Figure 1.9 – Representative pulse sequence diagram for the PGSE sequence when no diffusion is present (A) and when the spins diffuse (B). Here δ is the diffusion pulse duration and Δ is the duration between the two diffusion pulses. When no diffusion is present, the diffusion gradients act equally and opposite on either side of the refocusing pulse and all spins rephase to create a full echo. When diffusion is present, the diffusion gradients have unequal effects on either side of the refocusing pulse, thus leading to a reduced echo.

If a particle has not moved (ie. no diffusion has taken place), the phase changes caused by the two diffusion gradients will cancel resulting in no signal attenuation. Stejskal and Tanner showed that if a particle moved during or between the diffusion gradients, the magnetization, and therefore the signal $S(r)$, would be attenuated giving:

$$S(r) = S_0(r)e^{\left[-\gamma^2|G|^2\delta^2\left(\Delta - \frac{\delta}{3}\right)D\right]}$$

(52)

Commonly in Diffusion Weighted Imaging, several terms above are collected into a single "b-value", a term coined by Le Bihan [92]:

$$b = \gamma^2|G|^2\delta^2\left(\Delta - \frac{\delta}{3}\right)$$

(53)

This b-value is user defined and indicates the amount of diffusion "weighting" that attributed to a diffusion imaging pulse sequence. Now Equation (53) reduces to:

$$S(r) = S_0(r)e^{[-bD]} \qquad (54)$$

Simply put, diffusion of water during the time course of the pulse sequence leads to measurable signal loss.

1.5.7   Diffusion Timescales

So, what are these pulse sequence timescales and why do these scales uniquely lend themselves to applications such as neuroimaging? Table 1.1 shows some representative (but by no means exhaustive) values of axon diameter, cell body diameter, and extra axonal space (ie space between neighbouring axons) in both rats and humans. We term these unique areas as microstructural environments. The typical diffusion time in a diffusion experiment is determined from various pulse sequence parameters and largely ranges from 20-100 ms [88]. In that time the mean water displacement will range from 1 - 15 μm, which allows for enough diffusion to differentiate between each of the microstructural environments below. Therefore, over the course of a diffusion pulse sequence, the signal is weighted by not just diffusion, but the relative contribution of diffusion within each of these microstructural environments.

Table 1.1 - Representative values of human and rat microstructural features and diffusion parameters.

Quantity	Humans	Rats
Axon Diameter in Corpus Collosum	0.5 – 5.0 μm [93]	0.4 – 3.0 μm [94,95]
Neuron Cell Body Diameter	< 50 μm [96]	< 15 μm [97,98]
Extra Axonal Space	8 μm [99] (internal capsule)	not available
Diffusion time in DTI	50 - 100 ms [88]	
Mean Water Diffusion Distance	1 - 15 μm [100]	

1.5.8   Diffusion-Weighted Imaging (DWI) and the Apparent Diffusion Coefficient (ADC)

With this in mind, in 1990, Moseley *et. al.*, attempted to describe directional diffusion [101]. Combined with an "unweighted" image (ie. one lacking any diffusion gradient), the metric called apparent diffusion coefficient (ADC), may be obtained:

$$\frac{ln\,(S(b))}{S_0} = -b \cdot ADC \tag{55}$$

By measuring this ADC in multiple directions, a measure of anisotropy may be obtained. Initially, Moseley et al. proposed a metric based on ADC_z/ADC_x, requiring two DWI's [101]. This method suffered though as it was rotationally variant, and largely depended on the gradient encoding directions.

1.5.9   Diffusion Tensor Imaging

In an attempt to overcome the rotational variance, in 1994 Basser et al. proposed the use of the diffusion tensor to characterize the local diffusion within a voxel [102]. The diffusion tensor is given by:

$$\underline{D} = \begin{bmatrix} D_{xx} & D_{xy} & D_{xz} \\ D_{yx} & D_{yy} & D_{yz} \\ D_{zx} & D_{zy} & D_{zz} \end{bmatrix} \tag{56}$$

This is the same tensor used by Einstein to describe Anisotropic Gaussian diffusion. Thus, this tensor allows us to determine the magnitude and direction of diffusion in three independent directions within a given imaging voxel.

1.5.10   The Diffusion Tensor (Imaging) Metrics

Commonly there are several scalar metrics one may extract from the diffusion tensor:

Trace: The trace provides a metric of the magnitude of the diffusion tensor. Mathematically the trace is simply the sum of the individual eigenvalues of $\underline{D}$:

$$Trace\,(\underline{D}) = \lambda_1 + \lambda_2 + \lambda_3 \tag{57}$$

Here λ_1, λ_2, and λ_3 represent the principle, secondary and tertiary eigenvalues respectively.

Mean Diffusivity (MD): MD is a metric indicating the overall magnitude of diffusion, or simply the average of the eigenvalues of $\underline{D}$:

$$MD(\underline{D}) = \frac{\lambda_1 + \lambda_2 + \lambda_3}{3} \tag{58}$$

Axial Diffusivity (MD): For a directionally dependent diffusion tensor, the axial diffusivity may simply be defined as the magnitude of diffusion along the longitudinal (principle) axis of the tensor:

$$AD(\underline{D}) = \lambda_1 \tag{59}$$

Radial Diffusivity (MD): For a directionally dependent diffusion tensor, the radial diffusivity is the average diffusion radiating in the transverse directions of the tensor (secondary and tertiary eigenvalues):

$$RD(\underline{D}) = \frac{\lambda_1 + \lambda_2}{2} \tag{60}$$

Fractional Anisotropy (FA) is a metric ranging between 0 and 1 and describes the degree of directionality of the diffusion tensor. An FA value of 0 indicates purely isotropic (Gaussian Diffusion) while a value nearing 1 indicates highly directional diffusion. FA is mathematically determined as:

$$FA(\underline{D}) = \sqrt{\frac{(\lambda_1 - \lambda_2)^2 + (\lambda_2 - \lambda_3)^2 + (\lambda_3 - \lambda_1)^2}{2(\lambda_1^2 + \lambda_1^2 + \lambda_1^2)}} \tag{61}$$
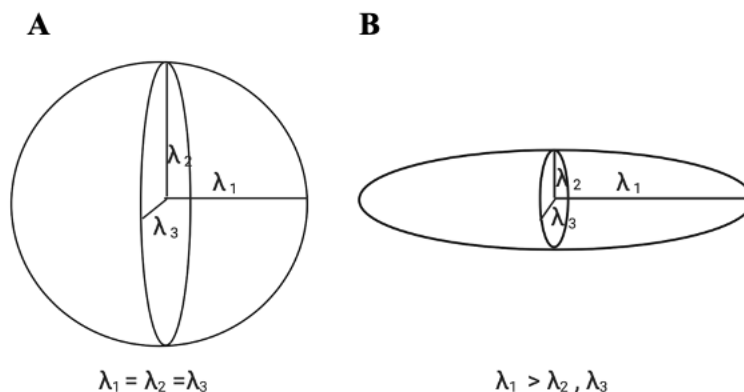
Figure 1.10 - Representative depictions of the diffusion tensor as an ellipsoid. A) Isotropic Gaussian diffusion, $\lambda_1 = \lambda_2 = \lambda_3$; FA = 0 B) $\lambda_1 > \lambda_2, \lambda_3$, 0 < FA < 1.

1.5.11   Shortcoming of dMRI and DTI

Since its introduction, DTI has largely become the standard for diffusion weighted imaging protocols. The applications have become widespread, including, but not limited to, brain injury [103,104] neurodegenerative disease [105,106], behaviour [107] and even cardiac imaging [108]. Indeed, DTI has become a powerful tool by which researchers may infer underlying tissue microstructure. Despite this utility, DTI suffers from some limitations. Each marker obtained provides a localized metric of average water diffusion from which subsequent analysis relies on inference for a conclusion. Thus, while powerful, DTI lacks the specificity to identify unique microstructural environments (such as those listed in 1.5.7). Without this information DTI cannot distinguish between distinct processes such as loss of structural integrity or neural remodelling, and thus leads to an inherently vague and limited model of neuroanatomy [109]. To this end, more sophisticated dMRI acquisition and reconstruction techniques have been developed to overcome the limitations of DTI one of which is neurite orientation dispersion and density imaging (NODDI) [29]. From here the focus of this thesis will be on NODDI.

1.6 Neurite Orientation Dispersion and Density Imaging

The following sections discuss neurite orientation dispersion and density imaging (NODDI) and how it may offer an improvement over traditional dMRI techniques such as DTI by reconstructing tissue microstructure directly from the diffusion MR signal. The equations and metrics derived in this section follow those presented in [29,30]

1.6.1   NODDI Tissue Model

NODDI uses a biophysical tissue model with three separate non-exchanging microstructural compartments: intra-neurite, extra-neurite and CSF. NODDI distinguishes between each compartment based on the diffusion characteristics of each of these distinct environments. The intra-neurite space refers to the space taken up by dendrites and axons collectively. The diffusion in this space is unique in that it is highly restricted in any direction perpendicular to the long axon of a neurite, while it is unhindered in a direction parallel to it. Conversely, within the space surrounding the neurite, largely comprised of glial cells, cell bodies and in the case of mTBI various blood borne proteins, diffusion is hindered but much less so than in the intra-neurite space. Thus, this diffusion may be described as simple anisotropic Gaussian diffusion. Finally, the CSF or isotropic compartment is simply the space taken up by cerebrospinal fluid and modeled as isotropic Gaussian diffusion.

1.6.2   NODDI Signal Equation

In this work a PGSE pulse sequence as described in the 1.5.6 is used to generate the NODDI signal. Based on the three-compartment model described above, the full acquired signal S is normalized as:

$$S = v_{iso}S_{iso} + (1 - v_{iso})(v_{in}S_{in} + (1 - v_{in})S_{en}) \qquad (62)$$

Here, S_n is the signal belonging to each characteristic microstructural compartment, and v_n is the volume fraction of water belonging to each characteristic microstructural compartment. Here $iso, in,$ and en indicate the isotropic, intra-neurite and extra-neurite

compartments respectively. Each compartment has a characteristic signal component that may be described individually.

First, the signal from the isotropic compartment is separated from the full signal equation (ie. CSF compartment). This is simply modelled as signal decay due to isotropic diffusion with diffusivity d_{iso}:

$$S_{iso} = e^{-bd_{iso}} \tag{63}$$

The intra-neurite component S_{in} is defined as a set of "sticks" of zero radius and parallel diffusivity $d_\parallel$ distributed in space according to the Watson distribution and mathematically defined as:

$$S_{in} = \int_{S^2} f(\vec{n}) e^{-bd_\parallel (\vec{q}\cdot\vec{n})^2} d\vec{n} \tag{64}$$

Here $e^{-bd_\parallel (\vec{q}\cdot\vec{n})^2}$ describes signal attenuation due to a given b-value, b, gradient direction, $\vec{q}$, and diffusion direction, $\vec{n}$, while $f(\vec{n})d\vec{n}$ is the probability of a given neurite having an orientation within $d\vec{n}$, an infinitely small cone centered around $\vec{n} \in S^2 \rightarrow \mathbb{R}^+$. Following the work of Zhang *et al.* [30], the orientation distribution function, $f(\vec{n})$, follows a Watson distribution:

$$f(\vec{n}) = M\left(\frac{1}{2}, \frac{3}{2}, \kappa\right)^{-1} e^{\kappa(\vec{\mu}\cdot\vec{n})^2} \tag{65}$$

Here M is a confluent hypergeometric function, $\vec{\mu}$, is the mean orientation and κ is the concentration parameter that quantifies the orientation dispersion about $\vec{\mu}$.

The extra-neurite signal component, S_{en}, is modelled as attenuation due to anisotropic Gaussian diffusion:

$$S_{en} = e^{-b\vec{q}^T\left[\int_{S^2} f(\vec{n})D(\vec{n})d\vec{n}\right]\vec{q}} \tag{66}$$

Here $D(\vec{n})$ is a cylindrically symmetric tensor, with parallel diffusivity $d_\parallel$, perpendicular diffusivity $d_\perp$ and principle diffusion orientation along $\vec{n}$. As in [29], the parallel

diffusivity matches that of the intra-neurite compartment, with the perpendicular diffusivity set using a tortuosity model [110] as

$$d_\perp = d_\parallel(1 - v_{in}) \tag{67}$$

The orientation dispersion index (ODI) is defined as a value ranging from 0-1 according to the concentration parameter of the Watson distribution κ

$$ODI = \frac{2}{\pi}arctan(\frac{1}{\kappa}) \tag{68}$$

1.6.3   NODDI Fitting

The NODDI fitting routine fixes the diffusivity values $d_\parallel$ = 1.7 x 10^{-3} mm^2/s and d_{iso} = 3.0 x 10^{-3} mm^2/s. The following parameters are then estimated to solve the above equations: v_{in}, κ, $\vec{\mu}$, and v_{iso}. Briefly, the fitting procedure first follows a brute-force search over a grid of physically plausible values based on known tissue properties. The results of this initial search are then used as a starting point for a Gauss-Newton nonlinear optimization procedure, using a Rician noise model, to produce the maximum likelihood estimates of the parameters listed above.

1.6.4   NODDI Acquisition

The NODDI acquisition scheme relies on a multi-shell acquisition scheme. Multi-shell refers to the use of multiple b-values and offers distinct advantages to the single shell acquisition (single b-value) employed in DTI. Higher b-value (> 1000 s/mm^2) images have been shown to increase contrast between gray matter and white matter and better elucidate the smaller microstructural features in white matter but suffer from low signal to noise ratio [111–113]. Lower b-value images (< 1000 s/mm^2) on the other hand provide a higher signal-to-noise ratio (SNR) and more anatomic information [114]. By using multiple b-values, we are able to gain both advantages and encode more detailed features of the cellular environment within our dMRI signal, with the caveat of increased acquisition time [115,116]. In 2012, Zhang *et. al.* provided the seminal work for the optimization of the NODDI acquisition [29]. It was shown for NODDI metrics to be

accurate and precise with only two moderate non-zero b-values. In simulation the optimal choice of these b-values to be 711 s/mm^2 and 2855 s/mm^2 but *in-vivo* the precise choice of these b-values had little effect on the resulting NODDI metrics. Finally it was also shown that the precise distribution of directions of b-values within and between shells had limited effect on the resulting parameters provided sufficient angular resolution was achieved (while sufficient was not expressly quantified within this paper, by convention it is taken to be a HARDI [117] acquisition with > 50 total gradient directions). While this study was performed in humans, it also showed quantitatively that all microstructural parameters were minimally affected by axon diameter lending this application to non-human models.

1.6.5   NODDI Metrics

From the above signal equations, the following scalar metrics may be obtained:

Neurite Density Index (NDI): Neurite density Index is a scalar value ranging from 0 to 1 and represents the volume fraction of the diffusion signal originating from within the axons and dendrites.

Orientation Dispersion Index (ODI): Orientation dispersion index is a scalar value ranging from 0 to 1 and represents the dispersion of the modelled "sticks" of the intra-neurite compartment. A value near 0 represents highly aligned and coherent fiber bundles (ie white matter tracts of the corpus collosum), while a value towards one represents widely dispersed fibers (ie grey matter).

Extra-Neurite Volume Fraction: The extra-neurite fraction represents the volume fraction of the diffusion signal originating from anisotropic gaussian diffusion. This would be indicative of diffusion near neurons and axons and within cell bodies. This is a simple 1-NDI, and thus varies inversely with NDI as a scalar value.

Isotropic Volume Fraction (IsoVF): Isotropic volume fraction is a scalar value from 0-1 and represents the signal originating from freely diffusing water. Within the nervous

system, this can largely be attributed exclusively to the CSF, but may also arise from pathological processes such as Edema.
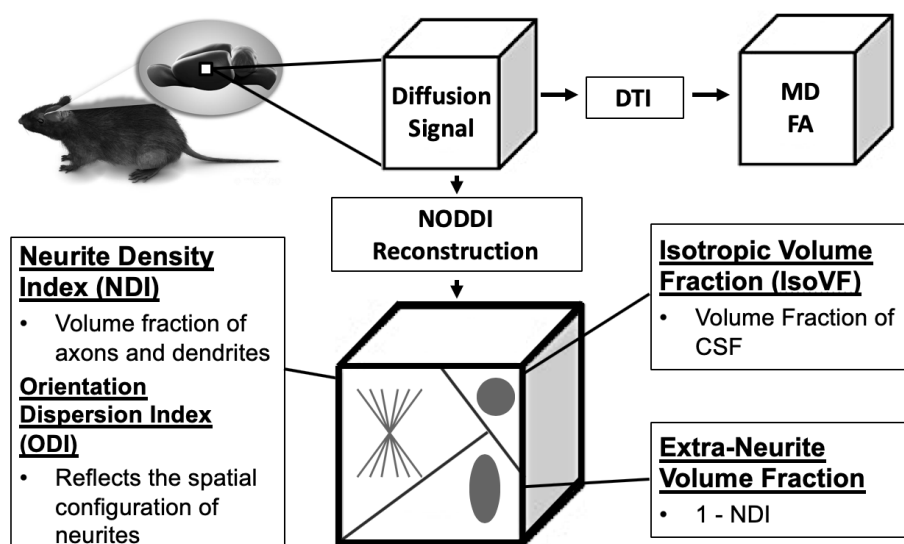
Figure 1.11 - Representation of the relevant NODDI metrics obtained from a multi-shell PGSE signal within a given imaging voxel. Notice the diffusion signal may be simultaneously reconstructed to produce DTI metrics.

1.6.6   NODDI in Traumatic Brain Injury

As discussed in Chapter 2, many neuropathological changes are evident in various stages of mTBI, of which NODDI may be well situated to detect due to the nature of the multi-compartmental biophysical model. Pathological processes such as axonal beading lead to an increase in NDI as the inner diameter of the axon expands, whereas demyelination would lead to a decrease in NDI. Separate changes within the extra-neurite compartment such as neuroinflammatory effects may lead to increased NDI. Thus, NODDI is uniquely situated to image mTBI *in-vivo* in an attempt to understand the various pathological processes taking places in the immediate stages following mTBI.

To this point though, the use of NODDI in traumatic brain injury studies has been undertaken exclusively in the clinical realm and to our knowledge, limited to a select few studies. Table 1.2 below summarizes the currently available studies applying NODDI to brain injuries and the relevant changes in NODDI metrics found in each study with respect to matched controls.

Table 1.2 - Summary of the currently published work applying NODDI in traumatic brain injury and concussion.

Study	Study Participants	Imaging Time Post-Injury	NDI	ODI	IsoVF
[118]	Athletes with a history of concussion (male and female)	> 6 months post-concussion	Increase (left anterior corona radiata and proximal to the left superior corona radiata)	Decrease (left anterior corona radiata. Splenium of the corpus callosum, superior longitudinal fasciculus	None
[119]	Athletes during concussion recovery (male and female)	1-7 days post-concussion	Decrease (corona radiata and longitudinal fasciculus)	None	None
[120]	Participants with mTBI due to auto p accidents.	15 ± 10 days post-mTBI	Decrease (various regions)	None	None

It can be seen that the study designs and results vary greatly. While these studies suggest the information provided by NODDI may be valuable in mTBI, such studies are still limited their ability to relate changes in diffusion to the underlying pathological processes taking place. Thus, for proper interpretation, we must first evaluate the effect of various pathophysiological processes on the signal changes detectable by NODDI in a traumatic brain injury. Pre-clinical rodent imaging provides such an opportunity.

1.6.7   NODDI in Pre-Clinical Rodent Models

In the development of novel techniques and exploration of disease models, pre-clinical animal models are often used. Mice and rats are often the animals of choice in these studies, as they share similar genetic information with humans, and in many instances similar biochemical, physiological, and microstructural properties [121] in the brain. Combined with their fast reproduction rate, relatively low economic footprint, and limited variation within breeds, rodent models are ideal to explore many normal and disease processes within the nervous system [122].

Although there are advantages to using rodent models, there are also many distinct disadvantages in regard to MRI. The largest of these is their size. The rat brain is approximately 500 times smaller than the human brain, presenting many technical challenges such as limited spatial resolution and low signal-to-noise ratio (SNR) [123,124]. Compounding these challenges with those specific to measuring the diffusion of water within and near neurites presents a challenging prospect. Many recent technical advances in MRI have helped to overcome these challenges including the use of ultrahigh field magnetic field strength (of particular importance to this thesis). Additionally, advances in modelling and image reconstruction have furthered the abilities of MRI within a pre-clinical setting such that the ability to image neurite density directly *in-vivo* in a pre-clinical rodent model is becoming a reality.

As described in section 1.2, the overall objective of this work is to develop neurite orientation dispersion and density imaging into a viable dMRI technique applicable to detection of subtle microstructural changes in pre-clinical rodent models of early mild traumatic brain injury at 9.4 Tesla. Additionally, we aim to determine whether NODDI metrics provided greater sensitivity than standard dMRI metrics to changes in the brain following mTBI in a rodent model. However, with any novel technique, the feasibility and reproducibility of the underlying metrics must be evaluated, so that researchers can confirm or reject a hypothesis with a known level of certainty. Therefore, the objective of the first experimental work described in this thesis was to quantify the reproducibility of NODDI in a rodent model at 9.4 Tesla. In addition, various analysis techniques and the necessary sample sizes and biological effects by which an accurate statistical inference may be gained were explored.

Chapter 2

2 Reproducibility of Neurite Orientation Dispersion and Density Imaging (NODDI) in Rats at 9.4 Tesla

2.1 Introduction

Diffusion weighted magnetic resonance imaging (dMRI) is a powerful magnetic resonance modality that provides a wealth of information regarding tissue microstructure, from which structural connectivity and pathological changes within the brain can be inferred [17,125]. As different microstructures predictably retard diffusion, the apparent diffusion of molecules combined with the angle of an applied diffusion gradient provides an indirect measure of neuroanatomy [102]. The most commonly used dMRI technique is diffusion tensor imaging (DTI). For DTI, a series of pulsed-gradient, spin–echoes are used to produce a 3x3 symmetric matrix modelling Gaussian diffusion (3). Most commonly, DTI characterizes the overall water diffusion within a given voxel by measuring mean diffusivity (MD) and the degree of directionality of the principle component of this diffusion, through fractional anisotropy (FA). This technique has been utilized for many years and has provided valuable insights into the effects of disease, as well as neurological and physiological processes [108,126–129].

However, subtle tissue diffusion characteristics may be missed in DTI because the method lacks the specificity to identify unique microstructural environments. For example, DTI cannot distinguish between distinct processes such as the loss of structural integrity and neural remodelling, and as a result provides an inherently vague and limited model of neuroanatomy [109,130]. Several more sophisticated dMRI models have been developed to overcome the limitations of DTI such as Q-Ball imaging [131], CHARMED [27], diffusion kurtosis imaging [132], oscillating gradient diffusion MRI [133], and more recently neurite orientation dispersion and density imaging (NODDI) [29]. NODDI examines neurite morphology by specifically probing the unique diffusion patterns within

three separate microstructural environments: intra-neurite, extra-neurite, and CSF compartments [29].

Diffusion patterns within the brain may be separated into three distinct microstructural environments: highly restricted within neurites (intra neurite compartment), hindered diffusion near neurites (extra-neurite compartment) and free diffusion within the CSF compartment [30]. A carefully designed diffusion weighting scheme in an MRI pulse sequence combined with NODDI modelling is used to produce scalar maps indicating the volume fraction contribution of each compartment to the full diffusion signal. The intra-neurite space is modelled as cylinders of zero radius (modelling highly restricted diffusion perpendicular to neurites and free diffusion parallel to neural tracts) dispersed according to the Watson distribution (ranging from heavily dispersed to entirely parallel) while the extra-neurite space is modelled as Gaussian anisotropic diffusion [134]. Lastly the CSF compartment is modelled with Gaussian isotropic diffusion [29].

The NODDI acquisition incorporates a multi-shell protocol that leads to a multi-compartmental diffusion MR signal. Previous work has shown that the use of 2 shells (each shell corresponding to a subset of diffusion weightings known as b-values) combined with several b=0 images, is sufficient to obtain NODDI scalar maps *in-vivo* [29]. These images are reconstructed based on the Stejskal-Tanner equations for a pulsed gradient spin-echo (PGSE) experiment, and the total signal determined to be the sum of the individual contributions from three non-exchanging tissue compartments (intra-neurite, extra-neurite, and CSF compartments) [29]. From this signal, quantitative scalar image maps may be reconstructed yielding the following NODDI metrics: neurite density index (NDI), orientation dispersion index (ODI), and isotropic volume fraction (IsoVF). Additionally, by ensuring one shell conforms to DTI acquisition standards (e.g. a single shell with > six directions of $b = 1000$ s/mm^2 and one $b = 0$ volume) [17], it is possible within a single scan to obtain standard diffusion tensor metrics such as fractional anisotropy (FA) and mean diffusivity (MD). It is commonly recommended that DTI and NODDI be acquired simultaneously and analyzed together [109]. While MD and FA are routine measures obtained in diffusion imaging, the addition of the ODI, NDI, and IsoVF scalar maps can provide a more specific analysis of complex neuroanatomy [109,130].

ODI characterizes the angular variation and spatial configuration of neurite structures. NDI represents the fraction of tissue that comprises axons or dendrites (also referred to as intra-neurite volume fraction). Extra-neurite fraction may be reconstructed as 1- NDI, and as such does not provide unique information separate from NDI. IsoVF represents the CSF water fraction [29].

Previous use of NODDI has focused largely on the feasibility, reproducibility, and application to human imaging at field strengths up to 3 Tesla [135–141]. Specifically, it was shown that NODDI metrics were significantly dependent on field strength [142]. Many pre-clinical studies use rodent models to study neuro-pathological processes requiring extremely small voxel sizes relative to that used in human MRI. Image signal to noise ratio (SNR) is directly proportional to voxel size and to main magnetic field strength. Therefore, the use of ultra-high field strengths combined with strong imaging gradients helps to achieve adequate SNR for diffusion modelling at the image resolution required in rodent models [143]. While the feasibility of NODDI at 9.4 Tesla has been shown [144], we are aware of no studies that have explored reproducibility in rodent models at 9.4 Tesla. As ultra-high field MRI, and specifically pre-clinical rodent MRI, faces many unique challenges such as increased magnetic field inhomogeneities and physiological noise [124], it is important to carefully define reproducibility in the context of ultra-high field rodent imaging. Thus, our specific objective was to determine the reproducibility of the three most commonly derived NODDI metrics (ODI, NDI and IsoVF) at 9.4 Tesla in the rat brain. This information is crucial for the planning of future studies involving rat models of neurodegenerative disease or neurological injury.

2.2 Methods

2.2.1   Subjects

Ten adult male Sprague Dawley rats were scanned twice on separate days with 7 ± 1 days between scans. Sample sizes were chosen to reflect common practice in pre-clinical imaging studies. On the day of the scans, anesthesia was initiated by placing the animals in an induction chamber with 4-5% isoflurane and an oxygen flow rate of 1-

1.5 L/min. Following induction, isoflurane was maintained between 1.5-2.5% with an oxygen flow rate of 1-1.5 L/min through a custom-built nose cone. All animal procedures were approved by the University of Western Ontario Animal Use Subcommittee and were consistent with guidelines established by the Canadian Council on Animal Care.

2.2.2   Imaging

All images were acquired using a 31 cm bore 9.4 Tesla Agilent small animal MRI scanner at the Centre for Functional and Metabolic Mapping at the University of Western Ontario. Images were acquired with an eight-channel receive coil used in conjunction with a 2-channel transmit coil. The receive coil consisted of eight loops adhered to the inner surface of a conformal helmet that was adjustable in width to accommodate varying head sizes. Low input-impedance preamplifiers were used to reduce inter-element coupling. The transmit coil was comprised of two overlapped rectangular loops mounted on an inverted U-shaped former. The coil design and optimization followed that built for marmoset imaging [145], but with dimensions optimized for rat imaging.

The NODDI diffusion encoding scheme was incorporated into a centric-ordered spin echo echo-planar-imaging (EPI) acquisition pulse sequence (number of shots = 4, number of averages = 2, 25 slices with slice thickness = 500 μm, FOV 40 x 40 mm, matrix size 160 x 160, resulting in-plane resolution = 250 × 250 μm, TE = 25 ms, TR = 5.0 s). Two averages were used, rather than increased diffusion directions, to ensure adequate SNR in the higher b-value shell for NODDI reconstruction. As it is recommended that NODDI be used in conjunction with standard DTI metrics (FA and MD) [109] we chose a b-value of 1000 s/mm^2 for the inner shell. Following the work of Zhang *et. al.* [29], a second b-value of 2000 s/mm^2 was chosen. Use of these b-values has been shown to produce reproducible values of NODDI specific metrics in human imaging at lower field strengths, and can be used to obtain standard DTI measures [29]. To sample q-space, we chose a scheme totaling 108 directions spread across two b-values, optimized according to Caruyer *et. al.* [146]. This sampling scheme allows for twice the number of directions in the higher b-value shell. Specifically, the outer shell consisted of 72 b-value = 2000 s/mm^2 directions (gradient strength (G) = 339.1 mT/m, time between the

start of the first and second diffusion pulse (Δ) = 14.44 ms, the duration of a single gradient pulse (δ) = 4.32 ms, TE = 25 ms and TR = 5.0s). The inner shell consisted of 36 b-value = 1000 s/mm^2 directions (G = 169.6 mT/m, Δ = 14.44 ms, δ = 4.32 ms, TE = 25 ms and TR = 5.0s). Fifteen b = 0 s/mm^2 were interspersed evenly throughout the acquisition and two preparation volumes were acquired at the beginning of each average but not used, resulting in a total imaging time of 83 minutes. A single reverse phase encoded b=0 volume was acquired at the end of the diffusion sequence for subsequent use in TOPUP and EDDY (number of shots = 4, number of averages = 2, 25 slices with slice thickness = 500 μm, FOV 40 x 40 mm, matrix size 160 x 160, resulting in-plane resolution = 250 × 250 μm, TE = 25 ms, TR = 5.0 s). Anatomical images were also acquired for each subject within each session using a 3D fast low angle shot [147] pulse sequence (250-μm isotropic resolution, FOV 40 x 40 x 20 mm, matrix size = 160 x 160 x 50, TE = 5.0 ms, TR = 30.0 ms, total acquisition time = 7 min).

2.2.3   Image Processing

Images were pre-processed using fMRI Software Library (FSL, v.5.0.10, Oxford, UK). TOPUP [148] followed by EDDY [149] was used to correct for eddy current induced distortions as well as susceptibility-induced distortions. Brain masks were produced using the 3D Pulse Coupled Neural Network (PCNN) tool for Matlab [150]. The NODDI Matlab toolbox (available from the UCL Microstructure Imaging Group) was then used to produce maps of ODI, NDI, and IsoVF in diffusion space.

For each subject, the first volume in each diffusion data set (b = 0) was aligned with its corresponding anatomical images using a linear registration in FSL (FLIRT) [151]. The transformation matrix from the preceding step was then used to bring all NODDI scalar maps into anatomical space. Anatomical images were then aligned to the Waxholm Space Atlas Sprague Dawley template [152] using a linear transformation (FLIRT) followed by a non-linear transformation (FNIRT) [153] in FSL. FNIRT registration parameters were optimized for the registration of rodent images. While a quantitative analysis (such as Dice coefficient) of registration quality was not performed, anatomical images were visually inspected to ensure good registration quality. The Waxholm Space Atlas

Sprague Dawley template includes binary masks for the relevant brain regions of interest in this study. Inverse transformation matrices from the preceding steps were used to bring these masks from template space into the anatomical image space of each rat. Each mask was eroded by 5% around the edges to avoid partial volume effects within a given ROI.

2.2.4   Statistical Analysis

Statistical analyses to examine measurement reproducibility were performed for the mean region of interest (ROI) analysis, the whole brain voxel-wise analysis, and the voxel-wise analysis within a given ROI. These three techniques were chosen as they represent the most common analysis techniques in neuroimaging studies. The ROI analysis focused on six different tissue regions: thalamus, corpus callosum, dentate gyrus, hippocampus, whole brain white matter, and whole brain grey matter. In both the ROI and voxel-wise analyses the scan-rescan reproducibility was characterized using the coefficient of variation (CV). CV was chosen as it reflects both the reproducibility and variability of these metrics as well as provides insight into necessary sample sizes and minimum detectable effect size. CVs were calculated between subjects and within subjects to quantify the between subject reproducibility and within subject reproducibility respectively. The between subject CV was calculated separately for the scan and rescan conditions as the group standard deviation divided by the mean values from subjects 1-8. These two CV values were then averaged for the mean between subject's CV in each case. The within subject CV was calculated as the standard deviation of the two scans divided by the mean value. The 8 within subjects CVs were then averaged to determine the mean within subject CV. Furthermore, the between subject CV was used to determine the minimum number of subjects needed per group to detect a defined biological effect. Similarly, the within subject CV was used to calculate the minimum detectable biological effect with a given number of subjects per group. The details of these calculations follow those presented in van Belle [154]. The minimum number of subjects and minimum detectable biological effect were both determined at a 95% significance level ($\alpha = 0.05$) and power of 80% ($1 - \beta = 0.80$).

2.3 Results

The minimum accepted average whole-brain SNR was 25 at b=0 for each of the included data sets. Two data sets were removed from the analysis due to low SNR causing significant reconstruction bias. Therefore, data were successfully acquired and analyzed from eight subjects (age 102 ± 13 days at time of initial scan, weight 323 ± 37 g) at two separate time points. For each subject the re-scan time point was between six and eight days after the original scan. The time of day was not standardized for the scans. Figure 2.1 shows representative cross sections of raw diffusion data (b=0) from a single subject, as well as scalar maps of ODI, NDI, and IsoVF.
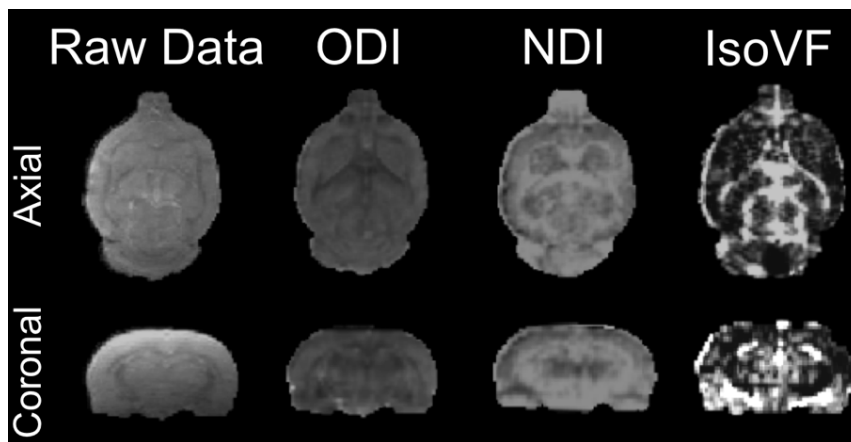
Figure 2.1 - Representative in-plane cross sections from a single subject showing unprocessed raw diffusion image data (4 shot, centric ordered, 2 averages, 25 coronal slices with slice thickness = 500 μm, 250 × 250 μm in plane resolution, FOV 40 x 40 mm, matrix size = 160 x 160, TE = 25 ms, TR = 5.0 s), and corresponding scalar image maps of the following NODDI values: Orientation Dispersion Index (ODI), Neurite Density Index (NDI), and Isotropic Volume Fraction (IsoVF).

2.3.1   ROI Analysis

Similar to previous human and rodent studies, higher average ODI values were observed within grey matter regions compared to that of white matter regions (Figure 2.2) as expected because neurite orientation is more widely dispersed throughout grey matter [142,144]. NDI and IsoVF values were similar between white and grey matter. Mean between and within subject CV for ODI ranged from 4.0-9.2% within all ROIs, NDI

ranged from 1.9-11.3%, while IsoVF ranged from 9.0-48.6% (Figure 2.3). In general, for each metric within a given ROI the mean between subject CV was higher than the within subject CV.
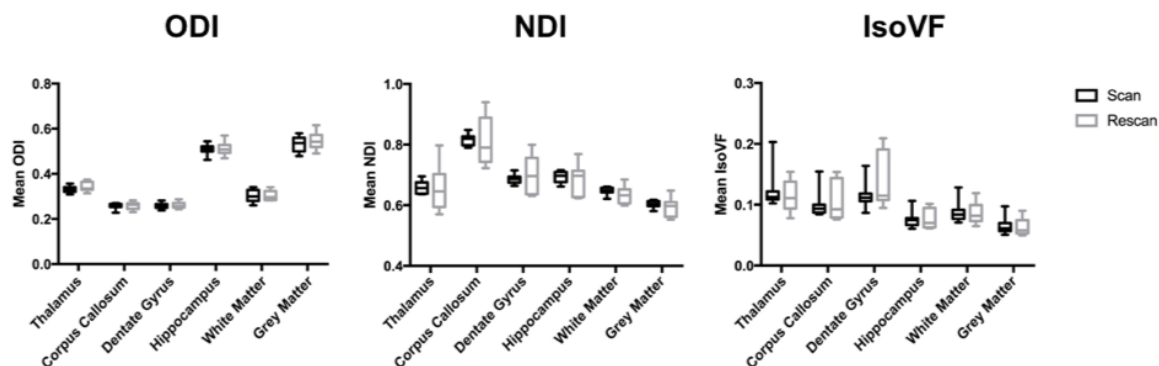
Figure 2.2 – Region of interest (ROI) values for ODI, NDI and IsoVF in both the scan and rescan conditions for several representative brain regions. Each box represents the range from 25th to 75th percentile (Interquartile Range) with the median depicted by the line within the box.
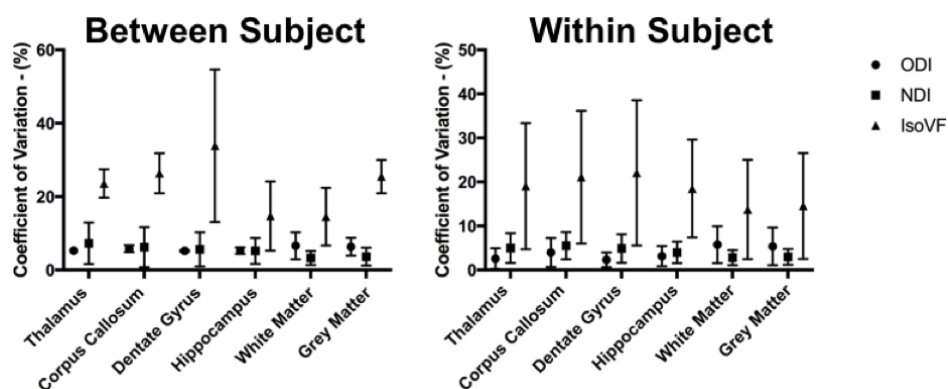
Figure 2.3 - Mean coefficient of variation (CV) for each ROI. Values for the between subject condition represent the mean ± standard deviation within each ROI averaged over a scan-rescan protocol. Values for the within subject condition represent the mean ± standard deviation within each ROI averaged over the eight subjects.

2.3.2   Whole brain voxel-wise analysis

The whole brain voxel-wise analysis showed a similar trend to the ROI analysis in terms of CVs. In the between subject histogram, over 90% of voxels fell below a CV of 20% for ODI while in the within subject histogram 90% of voxels fell below a CV of 17% (Figure 2.4 and Figure 2.5). For NDI over 90% of voxels fell below a CV of 15% and

12% for the between and within subject histograms respectively. The CV for IsoVF, ranged well above 100% for many voxels for both histograms.
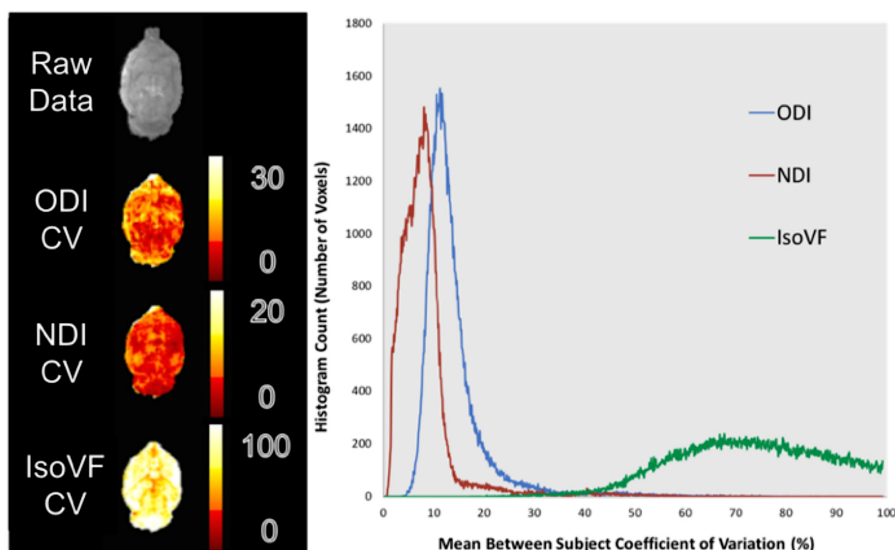
Figure 2.4 – Whole brain average between subject CV maps and histogram. Values for the between subject condition represent the mean CV within each voxel for the scan and rescan conditions averaged over the two scans. The resulting histogram has been extracted from the averaged scans. Heat maps from a representative slice show the regional variation for each metric.
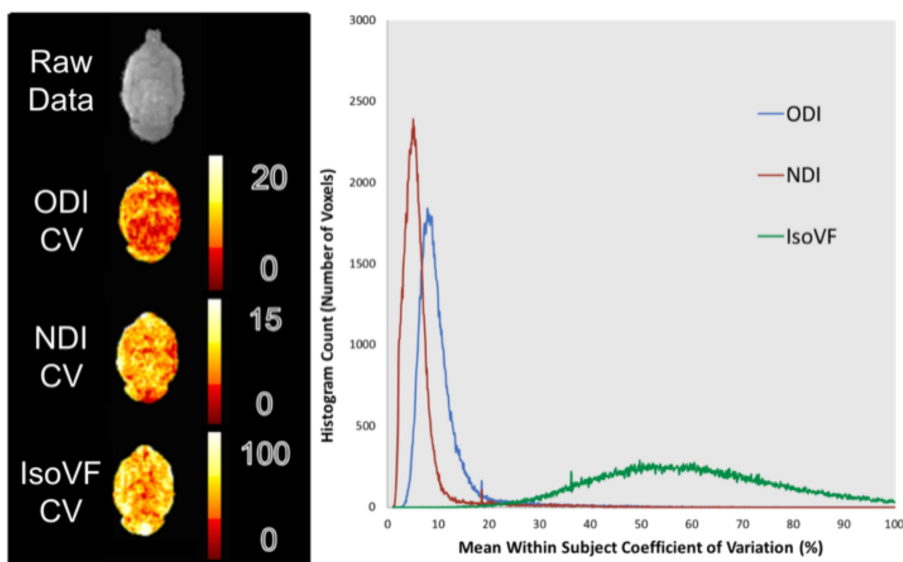
Figure 2.5 - Whole brain average within subject CV maps and histogram. Values for the within subject condition represent the mean CV within each voxel for each subject averaged over all eight subjects. The resulting histogram has been extracted from the averaged scans. Heat maps from a representative slice show the regional variation for each metric.

2.3.3 Voxel-wise ROI analysis

The voxel-wise approach targeted to specific ROIs (Figure 2.6) reinforced the results observed in mean ROI and the voxel-wise approaches. For ODI, over 90% of voxels fell below a CV of 18% in the between subject histogram, and 12% in the within subject histogram for all ROIs. For NDI, over 90% of voxels fell below a CV of 10% in the between subject histogram and 8% in the within subject histogram for all ROIs. The CV for IsoVF once again ranged well above 100% for many voxels in all ROIs. In all cases, dispersion of CV values increased with increasing ROI sizes. Likewise, in all cases and all ROIs the CVs and dispersion of CV values were lower within subjects compared to between subjects.
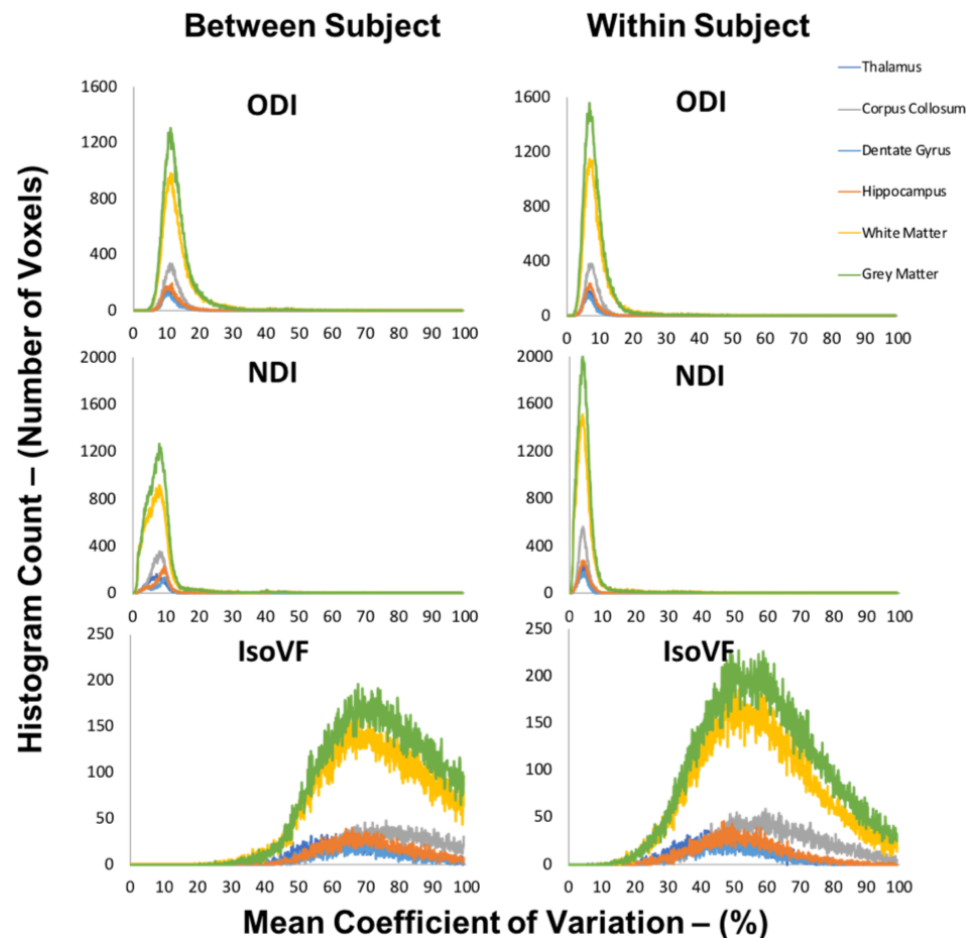
Figure 2.6 – Voxel-wise between and within subject CV histograms within each representative ROI. Voxel-wise values for the between subject condition represents the mean CV within each ROI for both the scan and rescan conditions averaged over the two

scans. Voxel-wise values for the within subject condition represent the mean CV within each ROI averaged over the eight subjects.

2.3.4   Sample sizes and minimum detectable effect

Using the between subject whole brain voxel-wise CVs, the minimum number of subjects was determined on a voxel-by-voxel basis that would allow detection of a statistically significant change of 5%, 10%, 15% and 20% between subjects in each metric. ODI produced detectable changes on the order 10% in all voxels for moderate sample sizes (n < 10) but required large sample sizes (n > 10) for whole brain voxel-wise detection of changes on the order of 5% (Figure 2.7). NDI was able to detect changes on the order of 5% in all voxels with small sample sizes (n < 6 for all voxels). IsoVF required large sample sizes (n > 10) to detect changes of any magnitude on a voxel-wise basis.

Using the within subject whole brain voxel-wise CVs, the minimum statistically significant change that may be detected in each metric on a voxel-wise basis was determined using a scan re-scan protocol for sample sizes of 6, 8 and 10 within each group. For over 90% of voxels, ODI was also able to detect small changes (<10%) on a scan-rescan basis with all sample sizes discussed, NDI showed detection of very small changes (<5%) with all sample sizes discussed and IsoVF lacked the ability to detect significant changes at any samples size explored.
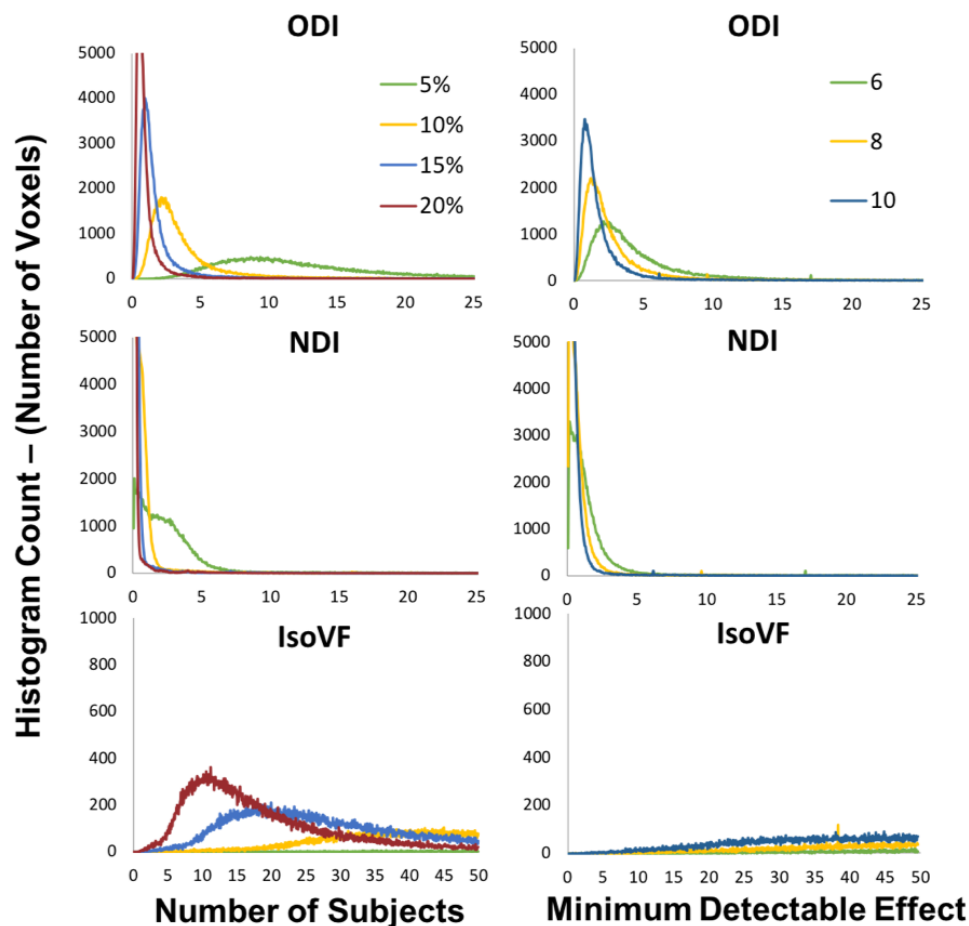
Figure 2.7 – Whole brain voxel-wise histograms representing the i) number of subjects necessary to detect a statistically significant effect with a change in the given metric of 5%, 10%, 15% and 20% and ii) the minimum detectable effect with each metric under a scan-rescan study design given group sample sizes of 6, 8 and 10. Note the varied scales for the IsoVF metric in each category as opposed to the ODI and NDI metrics.

2.4 Discussion

This study examined the reproducibility of the three most commonly derived NODDI metrics (ODI, NDI, and IsoVF) in the rodent brain at 9.4 Tesla. ODI and NDI were reproducible, showing low coefficients of variation in both the between and within subject conditions. CVs were lower within subjects compared to between subjects, indicating less variability on a within subject scan-rescan basis, as expected. These trends were observed in the mean ROI, whole brain voxel-wise, and targeted voxel-wise analyses.

Using the whole brain coefficients of variation on a voxel-by-voxel basis it was possible to detect changes on the order of 10% and 5% respectively in ODI and NDI metrics with feasible study samples sizes. For ODI, over 90% of voxels showed the ability to detect a 10% or greater change with sample sizes of five or more, while NDI showed the ability to detect a change of 5% or greater with sample sizes of five or more. NDI was the most sensitive in all cases, followed by ODI. Furthermore, it was shown that using a scan-rescan protocol and standard sample sizes (6, 8, and 10) it was possible to detect very small changes for both ODI and NDI. For example, sample sizes of eight per group (common to many preclinical studies) allowed biological effects as small as 5% to be detected on a voxel by voxel basis for both metrics.

While ODI and NDI were shown to be reproducible metrics, IsoVF was not. This was shown previously in similar studies of the human brain [142]. The IsoVF metric suffers from not only low values intrinsically in the given context but is also highly susceptible to noise [142]. This combination led to high average CVs (> 20%) in all measures explored in this study. Consequently, with the scan parameters used in this study, the reproducibility of IsoVF is limited. Improvements in SNR could increase the reproducibility of IsoVF but would come at the cost of increased scan time, decreased image resolution, or decreased angular resolution. It should be noted that inaccurate estimates of IsoVF could slightly bias the absolute values of NDI at low SNR, however this bias is expected to be consistent across all subjects and scans, allowing meaningful comparisons to be made under consistent scan parameters. As of now the optimal angular and image resolution in a rodent model of NODDI has yet to be explored, and it must be assumed that higher resolution in both improves the quality of the resulting scalar metric maps. Thus, an increase in scan time would be necessary. As the scan time in the present study was already high (83 minutes) it may be that the necessary scan time to improve the quality of IsoVF scalar maps is not feasible or cost effective.

These findings are consistent with previous research using human subjects. In humans, NODDI has been shown to produce accurate and reproducible metrics of ODI and NDI both between and within subjects [142]. The magnitude of NDI, ODI, and IsoVF have been shown to vary at different field strengths [142], and thus it is important to

characterize these metrics not only in new animal models, but also at each field strength used. At the time of writing we are not aware of any other studies that specifically look at the reproducibility of NODDI in an *in-vivo* rodent model. This study shows NODDI to be reproducible in a rodent model at 9.4 Tesla and that this technique has the potential to detect very subtle tissue microstructure changes in a rodent model.

There are several limitations that should be considered in this study. Registration was performed using FLIRT [151] and FNIRT [153] in FSL. The quality of these registrations was not specifically quantified in terms of similarity overlap. As the quality of registration is important to both ROI and voxel-wise analyses, future studies may benefit from improvements and optimization of the registration process. Specifically, when using a targeted voxel-wise approach within a given ROI, registration can be optimized within that region, thereby increasing the precision of the analysis. Currently, the optimal angular resolution, image resolution and b-value combination in our NODDI pulse sequence has not been fully explored in a rodent model at 9.4 Tesla. It is possible that at high angular resolution more subtle changes in orientation are detected, and at higher image resolution more subtle changes in neurite microstructure may be shown. Furthermore, these parameters may vary greatly in coherently ordered white matter compared to less ordered structures within regions of grey matter and may be altered in disease states. These considerations must be balanced against scan time for any *in-vivo* study. Further exploration of optimal angular resolution sampling schemes and image resolution would lend strength to this technique and lead to a more robust acquisition and analysis pipeline. Additionally, the optimal b-value has not been expressly explored in rodents at 9.4 Tesla. In humans, the optimal b-values were explored through simulation and *in-vivo* study, and it was found that as long as two shells with moderate b-value were used, the precise choice of b-value made minimal difference [29]. Finally, it should be noted that for the within-subject calculation of CV, the standard deviation was determined from only two data points. As a result, this this standard deviation may not accurately represent the spread of data within the population, leading to an unknown bias in the resulting CV.

The current study was designed to evaluate reproducibility of the NODDI metrics over a one-week interval, as this interval is relevant for many time course studies. While subtle changes in brain plasticity were of some concern, the results show that over this interval the ODI and NDI metrics were reproducible. Finally, we know of no studies which have expressly attempted to produce a template of absolute values of NODDI metrics within various brain regions of rodents at 9.4 Tesla. While intrinsic variability will always be present in these values due to scan parameters, it would be useful to attempt this characterization for all brain regions.

Preclinical imaging techniques, and specifically diffusion imaging techniques, are designed to detect very subtle changes in disease models, which may not be seen with anatomical based imaging techniques. The potential to improve the ability to detect these very small changes through novel neuroimaging techniques, such as NODDI, could illuminate early events in disease processes such as neurodegeneration. Early detection of key pathways and mechanisms involved in the progression of these devastating diseases may lead to a more thorough understanding of the downstream biological effects. By showing NODDI metrics to be reproducible in a rodent model at ultra-high field strengths, we may now apply this technique to appropriate pre-clinical models, in an effort to further our understanding of complex diseases processes affecting neuroanatomy.

Chapter 3

3 Neurite Orientation Dispersion and Density Imaging (NODDI) in a Rodent Model of Early Mild Traumatic Brain Injury

3.1 Introduction

Mild traumatic brain injury (mTBI) is known to result in a range of metabolic, microstructural, and behavioral effects. The clinical presentation varies greatly and sometimes unpredictably between subjects and over time and may impair many physical and cognitive functions [155–158]. Currently there is no pathognomonic test that can be used to accurately diagnose mTBI, assess the severity, or predict and monitor long-term outcome. Clinical assessments often rely on subjective measures and patient self-reporting, which are potentially biased, and may limit their utility [45,46]. Furthermore, Clinical Practice Guidelines (CPGs) regarding appropriate diagnosis and care following a traumatic brain injury vary widely in quality, comprehensiveness, and implementation [159–161]. Thus, it is imperative to develop unbiased metrics of mTBI that will allow informed and accurate diagnosis and lead to more effective patient treatment.

Very little is currently known about changes in the brain within the extremely early period post mTBI (< 4 hours post-injury). Patients are almost never available during this early phase for rigorous testing or data collection and thus little MRI data is available for this initial stage of injury [162]. Often, the severity of the injury is underreported, with patients only being admitted or cared for if symptoms worsen, once again eliminating the possibility to obtain clinical data in the very early stages of mTBI [163–165]. However, it is critical to understand the immediate underlying neurostructural changes that occur in the brain following injury to place observations at later time points into proper context. It is has been previously shown that many microstructural and neuroinflammatory changes occur in mTBI including neuronal cell death, axonal beading, and neuroinflammatory processes, but these studies have been largely limited to ex-vivo analysis [48,166–169]. Furthermore, several of these studies have indicated that many of these processes can

occur as early as 30 minutes post-injury, although there is substantial heterogeneity in the timing, injury model, and animal model used for these studies [56,170–173]. It remains imperative to develop methods to accurately and reliably assess and monitor the immediate microstructural and neuroinflammatory processes that occur following mTBI. Diffusion-weighted MRI (dMRI) is known to be highly sensitive to probing such changes in brain microstructure and neuroinflammatory processes *in-vivo* (please refer to Hutchinson *et. al.* [174] for an in depth review).

A number of different diffusion MRI approaches may be applied to the study of mTBI, however neurite orientation dispersion and density imaging (NODDI) provides the most direct means of assessing neurite integrity. NODDI is a powerful diffusion-weighted magnetic resonance imaging (dMRI) modality that can probe anatomical microstructure directly within the brain through careful measurement of water diffusion parameters [29]. NODDI uses a biophysical model by which the total dMRI signal is attributed to the intra-neurite, extra-neurite and CSF compartments. Each tissue compartment has unique diffusion characteristics and thus the fraction of signal attributed to each compartment may be separated and recovered uniquely. In this two-level compartmentalization approach, the volume fraction of water that diffuses freely (ie. Gaussian diffusion) is attributed to the CSF space and separated from the total signal. The remaining signal is compartmentalized into volume fractions of the intra-neurite space, where diffusion is highly restricted and directional, and the extra-neurite space, where Gaussian diffusion is hindered. The volume fraction of the intra-neurite space is represented by the metric neurite density index (NDI) and represents the volume fraction of signal originating from the dendrites and axons. The signal emanating from the extra-neurite space is representative of diffusion within cell bodies and near neurons and is simply 1- NDI. Thus, changes in the volume fraction of water in the intra-neurite and extra-neurite space are dependent on one another and will vary inversely. In addition to NDI, NODDI provides an orientation dispersion index (ODI), which characterizes the spatial configuration of neurites on a range from 0-1, with values near 1 indicating high dispersion (eg. grey matter), and values near 0 indicating highly coherent organization (eg. white matter). In addition, using data from the same acquisition it is possible to obtain the common diffusion tensor imaging (DTI) metrics, such as fractional anisotropy

(FA), mean diffusivity (MD), axial diffusivity (AD) and radial diffusivity (RD). FA represents the degree of directionality (as a scalar value from 0-1) and MD represent the overall amount of diffusion of the diffusion tensor as a whole. AD represents the amount of diffusion along the primary eigenvector alone and RD represents the average amount of diffusion along the secondary and tertiary eigenvectors [17].

There have been extensive studies using DTI in both people and pre-clinical animal models of mTBI, but the results have varied largely and provide little information with regard to the immediate structural and physiological responses in the brain to this injury [103]. Previous studies applying NODDI specifically to mTBI have occurred exclusively in the clinical setting. Churchill *et. al.* showed an elevated NDI and reduced ODI in various regions such as the corona radiata and corpus callosum of athletes with a previous history of concussion (but no reported concussions within 6 months) compared to controls [118]. In a further study, Churchill *et. al.* showed that in athletes scanned within 7 days of a diagnosed concussion, NDI was *reduced* in regions such as the corona radiata and longitudinal fasciculus, and that these changes persisted beyond the time that athletes were cleared to return to play [175]. While these studies are informative in clinical settings, there are currently no studies, either clinical or pre-clinical, that have applied NODDI to measure microstructural changes during the first few hours following mTBI. Similarly, we are unaware of any studies using any dMRI technique to examine changes as early as 1-hour post-injury in a mTBI model. However, in a recent study of mTBI in rats, mild to moderate changes in group mean FA, MD, and RD were detectable in the genu of the corpus callosum at 4 hours post-injury (and later timepoints) [176]. In another study of traumatic axonal injury (TAI) in mice, it was shown that statistically significant changes in AD, and relative anisotropy (RA) were detected in the corpus callosum by 4-6 hours following injury [21]. While the TAI injury model is far more severe than mTBI, taken together these studies indicate the presence of microstructural changes detectable with dMRI as early as 4 hours post-injury.

Given the lack of information regarding immediate brain microstructure changes following mTBI, the purpose of the current study was to apply NODDI to a rodent model of mTBI to determine whether microstructural changes in the corpus callosum could be

detected immediately following injury. Furthermore we investigated potential changes in the hippocampus as this brain region has been implicated in neurophysiological changes after various brain injuries [177,178]. Finally, we compared NODDI metrics to standard DTI metrics to determine if NODDI provided greater sensitivity to early microstructural changes following mTBI.

3.2 Methods

3.2.1 Subjects

Fifteen adult male Wistar rats (injury: n = 9, age at baseline scan: 123 ± 26 days, weight at baseline scan: 392 ± 27 g, control: n = 6, age at baseline scan: 131 ± 22 days, weight at baseline scan: 380 ± 17 g) were acquired from Charles River. Each animal was randomly assigned to either the control or injury group and was scanned twice: 7 days prior to injury (Timepoint 1), and from 1 – 4 hours post closed skull controlled cortical impact. From hours 1-4 post injury, data was collected approximately every 1 hour giving 3 acquisitions sequentially (Timepoints 2 - 4). Please refer to Figure 3.1 for the timeline of acquisition. All animal procedures were approved by the University of Western Ontario Animal Use Subcommittee and were consistent with guidelines established by the Canadian Council on Animal Care.
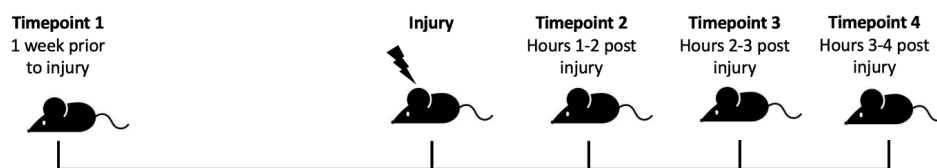
Figure 3.1 – Timeline of data acquisition for animals randomly assigned to the injury group which received a single closed skull controlled cortical impact.

3.2.2 Injury

While many different models have been developed to study TBI and mTBI in the pre-clinical setting, such as the Fluid Percussion Injury (FPI) [179,180] model, the Closed-Head Impact Model of Engineered Rotational Acceleration [181], and Blast TBI model

[182–184], we chose to use the closed skull controlled cortical impact (CCI) model [185–188]. CCI is a common and well documented model suited to closed skull mTBI, due to its close control, reproducibility, and pathophysiological response spectrum that mimics many important features of mTBI observed in humans [189–192]. It has been well documented in several animal models including rats and mice [193]. Since it is advantageous from an imaging perspective to use a larger brain, rats were used for the current study and the injury model was consistent with previous studies that have used closed skull controlled cortical impact to induce a mTBI [193–198].

Animals were anaesthetized by induction with 4% isoflurane followed by maintenance with 2% isoflurane. Each animal was placed in a Kopf mouse anesthesia mask (David Kopf Instruments, LLC, USA) under a traumatic brain injury device (TBI 0310, Precision Systems and Instrumentation, LLC, USA). For each impact, the device was programmed to impact at an intended depth of 3.0 mm, a velocity of 3.5 m/s and a 500-millisecond dwell time. The impact region for each animal was shaved prior to impact. Each animal received a single closed skull controlled cortical impact, centered at the sagittal suture, with a custom-made, 7 mm-diameter, pliant, silicone tip. Following controlled cortical impact, anesthesia was maintained at 2% isoflurane and using an in-house built portable induction chamber, each animal was transferred to the small animal MRI facility. Control animals were anaesthetized 20 minutes prior to their MRI to match the anesthesia time between induction and scan initiation in impacted animals.

3.2.3   Image Acquisition

Images were acquired using a 9.4T Bruker small animal MRI scanner at the Centre for Functional and Metabolic Mapping located within the Robarts Research Institute at the University of Western Ontario. Imaging included the acquisition of high-resolution anatomical images and NODDI in all animals. Anatomical images were acquired for each subject at the beginning of each session using a T2-weighted TurboRARE pulse sequence (8 averages, 32 slices, slice thickness = 500 μm, FOV 32 x 32 mm, matrix size 160 x 160, in-plane resolution = 200 x 200 μm, TE = 44 ms, TR = 7s, echo spacing = 11 ms, rare factor 8, total acquisition time = 14 min)[199]. The NODDI diffusion sequence

was incorporated into a multi-shot, spin echo, echo-planar-imaging (EPI) acquisition pulse sequence (4 shots, 32 slices, slice thickness = 500 μm, FOV 40 x 40 mm, matrix size 160 x 160, in-plane resolution = 250×250 μm, TE = 26.71 ms, TR = 2.5 s).

The NODDI diffusion scheme used was previously described in detail and was shown to produce reproducible and reliable results at 9.4 Tesla [200]. Briefly, a q-space sampling scheme was used across two-shells, optimized according to Caruyer *et. al.* [146], with a total of 90 directions. In shell one, 30 directions with b-value = 1000 s/mm^2 were obtained using the following diffusion gradient parameters: gradient strength (G) = 172.85 mT/m, time between the start of the first and second diffusion pulse (Δ) = 14 ms, the duration of a single gradient pulse (δ) = 4.5 ms. In shell two, 60 directions with b-value = 2000 s/mm^2 were obtained using the following diffusion gradient parameters: gradient strength (G) = 345.70 mT/m, time between the start of the first and second diffusion pulse (Δ) = 14 ms, the duration of a single gradient pulse (δ) = 4.5 ms.   Ten b = 0 s/mm^2 scans were interspersed evenly throughout the acquisition. Four averages were used to ensure adequate signal to noise ratio (SNR) in the higher b-value shell. The imaging time for each acquisition (four averages) was 66 minutes 36 seconds. A single reverse phase encoded b=0 volume was also acquired prior to the diffusion sequence for subsequent use in image processing to correct image distortions.

3.2.4   Image Processing

Brain masks were produced using the 3D Pulse Coupled Neural Network (PCNN) tool for MATLAB (R2019a) [150]. Raw data were pre-processed using fMRI Software Library (FSL, v. 6.0.1, Oxford, UK). TOPUP [148] followed by EDDY [149] was used to correct for eddy current induced distortions as well as susceptibility-induced distortions. The FDT toolbox (v. 5.0) was used to produce maps of FA, MD, AD, and RD. The NODDI Matlab toolbox (available from the University College London (UCL) Microstructure Imaging Group) was then used to produce maps of NDI, ODI, and IsoVF. All diffusion maps were produced within each subject's native diffusion image space. While IsoVF is produced during the processing steps, our previous work has indicated it

has extremely high variability and low reproducibility with this scan protocol and therefore we limited our analysis to NDI and ODI only.

3.2.5   Image Registration

For each subject, the first volume in each diffusion data set (b = 0) was aligned with its corresponding anatomical images using a linear registration in FSL (FLIRT) [151]. The anatomical image for each subject was then aligned to the Waxholm Space Atlas Sprague Dawley template [152] using a linear transformation (FLIRT) followed by a non-linear transformation (FNIRT) [153] in FSL. Binary ROI masks of the corpus collosum and hippocampus from the Waxholm Space Atlas, were then transformed into the anatomical space of each individual subject by inverting the preceding non-linear transformations. Finally, the masks were brought into diffusion space using the inverse transformation matrix from the b0 image to anatomical image registration. Thus, each mask was brought into each subject's individual native diffusion image space. Each mask was then eroded by a single voxel around the edges to avoid partial volume effects. Masks were visually inspected to ensure accuracy. For a full description of the processing steps please and representative binary ROI masks please refer to Supplement.

3.2.6   Statistical Analysis

For each subject, at each timepoint the mean value of each individual scalar metric within each relevant ROI was extracted using fslstats and the relevant binary mask. A mixed ANOVA in SPSS [201] was used for each metric to determine if there were statistically significant interaction effects (p < .05) between controls and injured animals over time. This test examined whether each metric changed over time and whether those changes were different between the two groups. Mauchly's Test was used to determine if the assumptions of sphericity were violated. In cases where the assumption of sphericity was rejected, the Greenhouse-Geisser correction was used. In each case where a statistically significant interaction effect occurred, a follow-up repeated measures ANOVA was run separately on each group (injured and controlled) to determine if there were statistically significant changes (p < .05) in the diffusion metric over time within each group.

Furthermore, post-hoc analysis was used to determine which timepoints differed within each group (Bonferroni corrected).

3.3 Results

Imaging data were successfully acquired from all 15 animals. Figure 3.2 provides representative anatomical and corresponding NODDI and DTI scalar maps in a single animal.
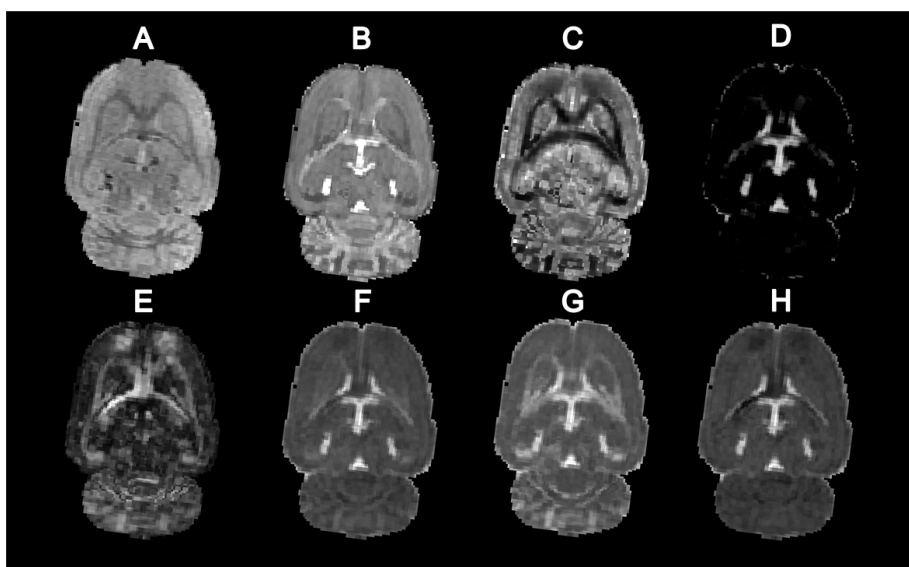
Figure 3.2 – Representative axial single-subject A) raw diffusion image data (b0) and the following scalar diffusion maps: B) Neurite Density Index (NDI) C) Orientation Dispersion Index (ODI) D) Isotropic Volume Fraction (IsoVF) E) Fractional Anisotropy (FA) F) Mean Diffusivity (MD) G) Axial Diffusivity H) Radial Diffusivity . The diffusion images were acquired with a multi-shell sequence (10 b= 0 s/mm², 30 b = 1000 s/mm² and 60 b= 2000 s/mm²) incorporated into a multi-shot, spin echo, echo-planar-imaging (EPI) acquisition pulse sequence (4 shots, 32 slices, slice thickness = 500 μm, FOV 40 x 40 mm, matrix size 160 x 160, in-plane resolution = 250 × 250 μm, TE = 26.71 ms, TR = 2.5 s).

The exact start and end time of each image varied slightly for each animal: Timepoint 1 (or baseline scan) obtained 7 days prior to injury, Timepoint 2 began at 75 minutes $\pm$ 16 minutes post-injury, Timepoint 3 began at 142 ± 17 minutes post-injury, and Timepoint 4 began at 210 ± 17 minutes post-injury.

3.3.1 Corpus Callosum

Mean ROI metrics in the corpus callosum (Figure 3.3) show a significant increase in the NDI and ODI immediately after injury that persists to four hours post injury. The first timepoint after injury showed a 0.046 ± 0.026 (7.83%) increase in average NDI and a 0.051 ± 0.037 (13.7%) increase in average ODI compared to baseline. In contrast, no changes were observed over time in the control groups. Relevant statistical results are described in Table 3.1.
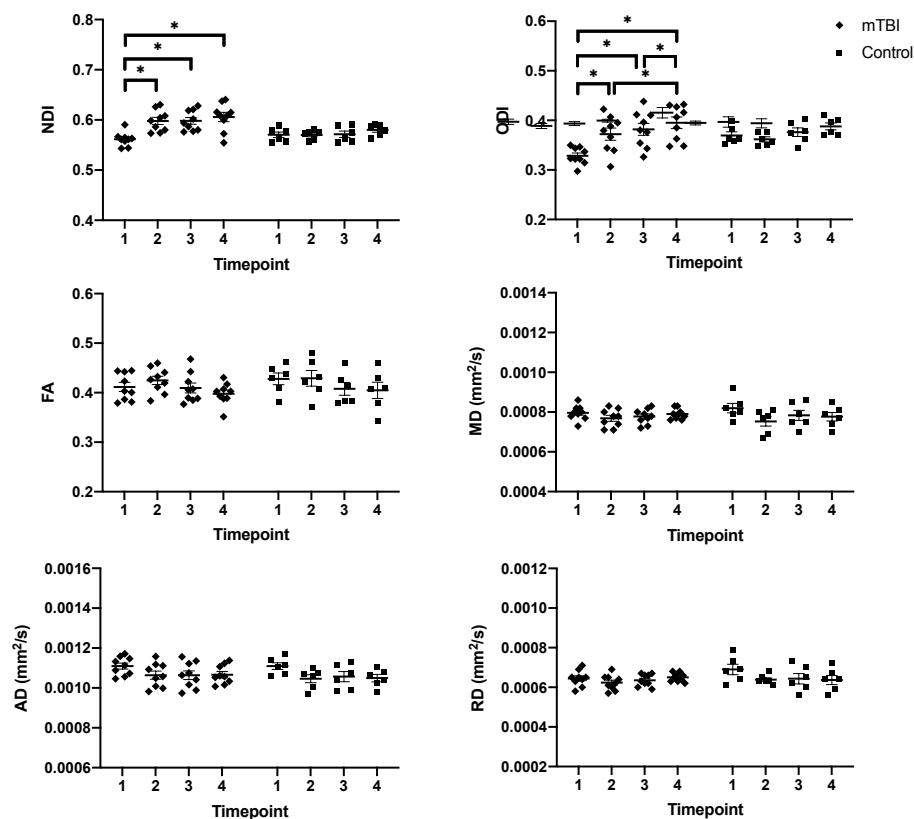
Figure 3.3 - Mean ROI Metrics within the corpus callosum for injured and control subjects. At each point the mean of the ROI values ± SEM is shown. For NDI and ODI in the corpus callosum a mixed effects ANOVA in SPSS showed a statistically significant group by time interaction (p < .05). A repeated measures ANOVA was then used to determine individual differences amongst the injured and control groups. Post-hoc pairwise comparisons (Bonferroni corrected) were performed between individual timepoints within each group. Statistically significant (p < .05) pairwise differences are indicated by *. Statistical results are listed in Table 3.1 (Mixed ANOVA) and Table 3.2 (Repeated Measures ANOVA).

Table 3.1 lists the statistical results of the mixed effects ANOVA for both NODDI and DTI metrics in the corpus callosum. There was a statistically significant (p < .05) group by time interaction effect for NDI and ODI. There were no statistically significant interaction effects (p > .05) of group by time for FA, MD, AD and RD.

Table 3.1 – Statistical results of the mixed effects ANOVA for NODDI and DTI metrics within the corpus callosum. Statistical significance is taken to be p < .05, is denoted with an asterisk (*) and indicates there is a statistically significant group by time interaction for that metric within the corpus callosum.

Metric	Statistical Results		
NDI	F (3,39) = 6.573	p = .001*	Sphericity Assumed
ODI	F (3,39) = 6.355	p = .011*	Greenhouse-Geisser
FA	F (3,39) = 0.445	p = .722	Sphericity Assumed
MD	F (3,39) = 1.085	p = .345	Greenhouse-Geisser
AD	F (3,39) = 0.166	p = .772	Greenhouse-Geisser
RD	F (3,39) = 1.919	p = .142	Sphericity Assumed

The follow-up univariate analysis of NDI and ODI showed a statistically significant change over time for the injured group, while no statistically significant change over time occurred within the control group for these metrics Table 3.2. Statistically significant changes between individual timepoints within the injury group are depicted in Figure 3.3. It should be further noted that for every individual subject in the injury group, an increase occurred in both NDI and ODI from timepoint 1 (Baseline) to timepoint 2 (refer to Figure 3.4). Following this increase, a more heterogenous individual response occurred from timepoints 2-4, but statistically significant group increases were observed at all three timepoints post impact.

Table 3.2 - Statistical results of the follow up univariate ANOVA for NDI and ODI metrics within the corpus callosum. Statistical significance is taken to be p < .05, is denoted with an asterisk (*) and indicates there is a statistically significant change in each metric over time within the given group (Injured or Control).

Metric	Statistical Results			
NDI	Injured	F (3,21) = 13.618	p = .001	Greenhouse-Geisser
	Control	F (3,9) = 1.318	p = .328	Sphericity Assumed
ODI	Injured	F (3,21) = 9.504	p = .000	Sphericity Assumed
	Control	F (3,9) = 3.431	p = .066	Sphericity Assumed
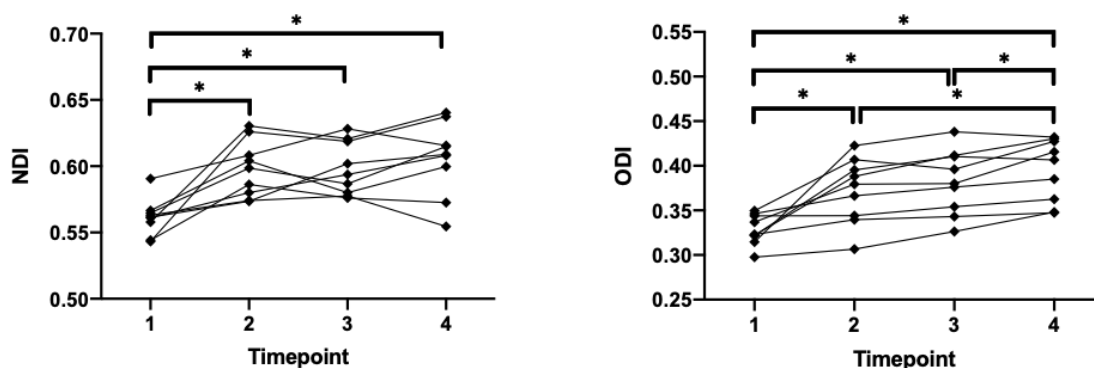
Figure 3.4 - Mean ROI values of NDI and ODI within the corpus callosum for the injured group only. It can be seen that for every individual subject in the injured group, a statistically significant increase in both NDI and ODI occurred from timepoint 1 to timepoint 2. Following this increase, statistically significant group increases were observed at all three timepoints post impact, but the individual response varied. Statistical significance is taken to be p < .05, is denoted with an asterisk (*).

3.3.2   Hippocampus

Mean ROI metrics in the hippocampus (Figure 3.5) show a significant increase in the NDI only immediately after injury that persists to four hours post injury. The first timepoint after injury showed a 0.022 ± 0.021 (3.93%) increase in average NDI. In contrast, no changes were observed over time in the control groups. Relevant statistical results are described in Table 3.3.
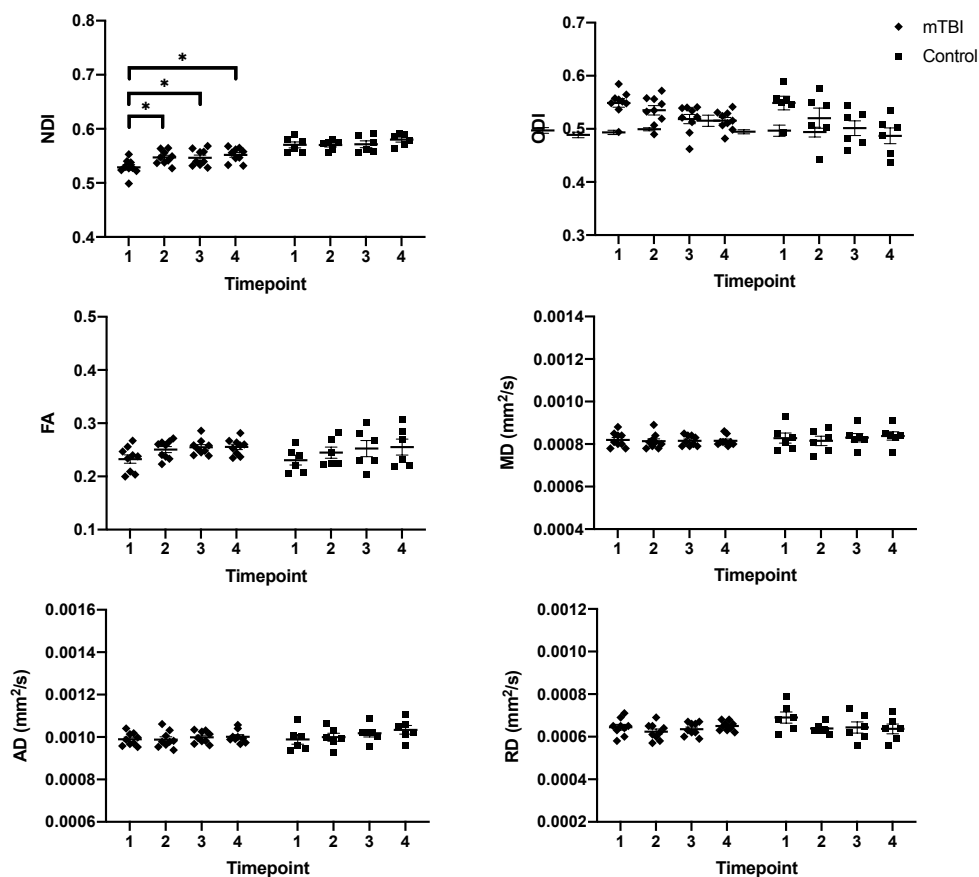
Figure 3.5 - Mean ROI metrics within the hippocampus for injured and control subjects. At each point the mean of the ROI values ± SEM is shown. For NDI and ODI in the corpus callosum a mixed effects ANOVA in SPSS showed a statistically significant group by time interaction (p < .05). A repeated measures ANOVA was then used to determine individual differences amongst the injured and control groups. Post-hoc pairwise comparisons (Bonferroni corrected) were performed between individual timepoints within each group. Statistically significant (p < .05) pairwise differences are indicated by *. Statistical results are listed in Table 3.3 (Mixed ANOVA).

Table 3.3 lists the statistical results of the mixed effects ANOVA for both NODDI and DTI metrics in the hippocampus. There was a statistically significant (p < .05) group by time interaction effect for NDI only. There were no statistically significant interaction effects (p > .05) of group by time for ODI, FA, MD, AD and RD.

Table 3.3 - Statistical results of the mixed effects ANOVA for NODDI and DTI metrics within the hippocampus. Statistical significance is taken to be p < .05, is denoted with a (*) and indicates there is a statistically significant group by time interaction for that metric within the hippocampus.

Metric	Statistical Results		
NDI	$F(3,39) = 7.077$	$p = .009$	Greenhouse-Geisser
ODI	$F(3,39) = 0.943$	$p = .382$	Greenhouse-Geisser
FA	$F(3,39) = 0.086$	$p = .967$	Sphericity Assumed
MD	$F(3,39) = 0.275$	$p = .843$	Greenhouse-Geisser
AD	$F(3,39) = 0.656$	$p = .493$	Greenhouse-Geisser
RD	$F(3,39) = 0.186$	$p = .779$	Greenhouse-Geisser

The follow-up univariate analysis of NDI showed a statistically significant change over time for the injured group while no statistically significant change over time occurred within the control group [Injured $F(3,24) = 8.648$, $p = .000$ Greenhouse-Geisser; Control $F(3,15) = 2.015$, $p = .155$, Sphericity Assumed]. Statistically significant changes between individual timepoints within the injury group are depicted in Figure 3.6. Once again, we see an increase in NDI from timepoint 1 (Baseline) to timepoint 2 in each individual subject. Following this increase, a more heterogenous individual response occurred from timepoints 2-4, but statistically significant group increases were observed at all three timepoints post impact compared to baseline.
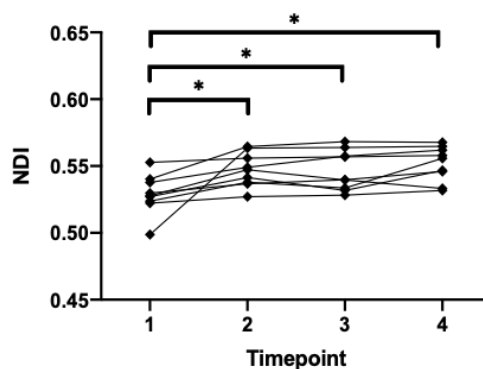
Figure 3.6 – Mean ROI values of NDI and ODI within the hippocampus for the injured group only. It can be seen that for every individual subject in the injured group, a statistically significant increase in both NDI and ODI occurred from timepoint 1 to timepoint 2. Following this increase, statistically significant group increases were observed at all three timepoints post impact, but the individual response varied. Statistical significance is taken to be p < .05, is denoted with an asterisk (*).

3.4 Discussion

The current study used an adult rodent model to examine the immediate effects of mild TBI on changes in conventional diffusion MRI and NODDI metrics. While no changes in traditional DTI metrics (FA, MD, AD and RD) were detected within the first four hours of injury, significant differences were observed in the NODDI metrics (NDI and ODI) as early as 1-hour post injury compared to baseline suggesting a microstructural change in this rodent model. Specifically, both NDI and ODI were increased in the corpus callosum immediately after impact, and NDI was increased in the hippocampus. Therefore, this study provides evidence that NODDI metrics are sensitive to microstructural changes within the earliest stages of this rodent model of mild traumatic brain injury, and that these NODDI metrics are more sensitive to such changes than traditional DTI metrics.

Neurite density index (NDI) represents the volume fraction of signal originating from the dendrites and axons. In the current study, NDI was shown to be elevated in both the corpus callosum and hippocampus at the first timepoint post-injury when compared to baseline values in the mTBI group and continued to increase over time. Several microstructural changes should be considered to explain these observations including the many microstructural changes that have been previously shown in models of mTBI including neuronal cell death, axonal swelling and beading, and various myelination and remyelination processes [47,48,202]. Due to the extremely early measurement time used in the current study (~1h post injury), the most likely of these processes that could be occurring and contributing to the increased NDI is axonal swelling and beading. Previous studies have indicated the presence of axonal swelling and beading in mTBI, with some models showing this phenomenon as early as 30 minutes to 1 hour post injury [203,204], although there is substantial heterogeneity in both the injury and animal model used in many of these studies [56,170,171]. In the current study, the observed increase in NDI is consistent with an increase in the interior diameter of axons due to these beading and swelling processes. Beading and swelling may disrupt axonal transport in the very early stages of mTBI [205,206].

While the NODDI biophysical model is restricted to three non-exchanging compartments, the microstructure of the brain is much more complicated. Specifically, there are multiple constituents within the extra-cellular compartment that may contribute to the changes in diffusion metrics observed in this study. Blood brain barrier disruption has become a common hallmark of mTBI and would directly influence the extra-cellular space [207]. This disruption has been shown to occur extremely quickly, as early as minutes after injury in pre-clinical studies, and further shown to persist for years in clinical populations [208–211]. As the blood brain barrier becomes compromised due to a mTBI, various constituents such as blood borne proteins thrombin and fibrinogen are free to enter the brain [38,212]. If these enter the extra-cellular space surrounding neurons, they could contribute to diffusion changes that are indicative of a reduction in the extra-cellular space. Since the intra-cellular and extra-cellular space varies inversely, reduced extra-cellular space would lead to increased intra-cellular space and consequently an increase in the NDI metric as observed in the current study. Furthermore, this infiltration of the extra-cellular space has been linked to microglial activation and the production of pro-inflammatory factors [209,212].

Another component that must be considered in the interpretation of the NDI metrics is the potential indirect contribution of glial cells. Neuroinflammatory processes have been shown extensively in traumatic brain injury, including microglial activation and astrocytic hypertrophy [48,61]. While glial cells are much smaller than neurons, they outnumber them considerably [213], and the bulk effect on the scale of our voxels could contribute to the metrics observed in this study. Neuroinflammatory processes could lead to reduced extra-cellular space as glial cell infiltration occurs in the extra-cellular space. Furthermore, the morphological features of glial cells vary widely under normal and pathological conditions, leading to altered geometric properties [214,215]. On the scales present in rodent microstructure, it is possible that the diffusion processes within and near activated glial cells could cause a shift in the intra-cellular to extra-cellular volume fractions and the observed change in NDI. Furthermore, in previous studies of rat and mouse models of mTBI, compression injury, and BBB disruption, it has been shown that microglia can respond within minutes by activating and undergoing morphological changes [216–219]. However, the evidence to support this early glial response is

extremely limited in mTBI models, and more commonly microglial activation is discussed within 3-6 hours of injury and beyond [220,221]. Therefore, it is possible that changes in glial cell morphology could produce an increase in the measured NDI but this interpretation requires thorough histological validation to confirm such an early neuroinflammatory response.

Orientation dispersion index (ODI), characterizes the spatial coherence or dispersion of neurites. In the current study, ODI was also increased in the corpus callosum at the initial timepoint post injury compared to baseline and continued to increase over time post-injury suggesting less coherence (greater dispersion) over time. In a single study in mice, it was previously shown that an increase in glial cell load correlated with an increase in ODI [222]. Therefore, the increase in ODI observed in the current study in the corpus callosum could indicate an increase in glial cell density and altered morphology in the injury group, but would be considered extremely early for a glial cell response of this nature. Similar to the increase in glial cell population contributing to a change in ODI, the infiltration of blood borne proteins due BBB disruption may lead to the observed increase in ODI. It is currently unknown whether BBB disruption changes the measured NODDI metrics in humans or pre-clinical models. A detailed histological analysis would be required to determine whether these BBB disruptions occurred in the current model.

Interestingly, there were no statistically significant changes observed in the current study in any of the conventional DTI metrics characterizing the corpus callosum or hippocampus. This result is consistent with the existing literature, where there is a paucity of work to characterize DTI changes in the first hours following mTBI. In previous studies examining mTBI in rats and traumatic axonal injury (TAI) in mice, statistically significant changes in diffusion metrics were detected in the corpus callosum in the acute phase (4-6 hours) following injury. [21,176] The earliest timepoints examined in these studies were 4-6 hours post-injury, which corresponds approximately to the latest timepoint examined in the current study. It seems that DTI metrics may able to detect microstructural changes in more aggressive trauma models or at later timepoints but may lack the sensitivity to detect very early changes in mTBI models.

3.5 Limitations

One of the common challenges with the interpretation of changes in dMRI metrics is determining a microstructural basis for the detected change of each metric. Various dMRI techniques have been used to study mTBI, but the results have been largely inconsistent, leading to varied interpretations of the underlying biological processes, and providing limited diagnostic or clinical utility [104,119,120,223–226]. While NODDI provides biologically relevant metrics in terms of the underlying structure, it requires careful interpretation. Particularly difficult is the fact that the intra-cellular and extra-cellular volume fractions intrinsically vary inversely [29]. Thus, any interpretation of the increase in NDI in the current study must also consider the possibility that a decrease in the extra-cellular volume fraction may be responsible. We have presented several possible biological processes that may occur individually or in concert that could lead to microstructural changes detectable by NODDI, however these changes were not confirmed with histology, which was beyond the scope of this study. While neuroimaging has many strengths, particularly the ability to provide *in-vivo* quantitative tissue characterization, it is dramatically limited in resolution when compared to histological analysis. With careful histology, the changes observed in this study could potentially be attributed to specific biological processes occurring in the brain. This association would in turn allow future clinical and pre-clinical studies to infer these changes on the basis of a given NODDI metric change.

Additionally, the current NODDI biophysical model fails to take into account glial cell contributions to the diffusion signal. It is conceivable that these contributions could be uniquely separated based on glial cell geometry, allowing a more clearly defined picture of the entire microstructural environment. Further, while NODDI metrics have been shown to have minimal dependency on axon diameter [29], this has not been expressly validated on pre-clinical models or ultra-high field systems. It should also be noted that during our image processing steps, the registrations were visually inspected for quality but no attempt was made to quantify image registration performance, such as a Dice index [227].

Finally, the current injury protocol did not include measures of injury kinematics, or subsequent behavioural impairment and cognitive defects. Thus, there could be an unknown bias or heterogeneity present in the imaging metrics observed that could be explained by varied brain injury. Future studies would benefit from the characterization of these aspects of injury. Furthermore, as anaesthesia is needed for all rodent MRI studies we induce an unknown bias to all studies as isoflurane anaesthesia has been shown to attenuate both positively and negatively the neuroinflammatory response [228,229] and blood brain barrier permeability [230–232]. While we account for the effect of anaesthesia separately with our control group, we cannot fully account for the interaction effect of the injury response and anesthesia.

3.6 Conclusions

Increased neurite density and orientation dispersion were detected in the corpus callosum and hippocamps of a rodent model by neurite orientation dispersion imaging in the initial hours following a mild traumatic brain injury. These microstructural changes were detected by NODDI in the absence of changes in traditional DTI metrics, demonstrating NODDI to have greater sensitivity to tissue changes immediately following injury.

3.7 Supplement


```
┌─────────────────────┐
│  Raw Diffusion Data  │
└─────────────────────┘
           │
           ▼
┌─────────────────────┐    ┌─────────────────┐    ┌─────────────────────┐
│     dcm2niix:       │    │  Topup, EDDY,   │    │  Scalar Diffusion   │
│ NIFTI Diffusion Data│───▶│ DTIFIT, NODDI   │───▶│ Maps: FA, MD, RD,   │
└─────────────────────┘    │    Toolbox      │    │  AD, NDI, ODI,      │
           │               └─────────────────┘    │     IsoVF           │
           ▼                                       └─────────────────────┘
┌─────────────────────┐                       ┌─────────────────┐   ┌─────────────────────┐
│      FSLROI:        │                       │ FSLSTATS: Extract│  │ Mean ROI values in  │
│     Extract b0      │                       │ Mean ROI Values │──▶│ individual subject's│
└─────────────────────┘                       └─────────────────┘   │  diffusion space    │
           │                                                         └─────────────────────┘
           ▼
┌─────────────────────┐                       ┌─────────────────────┐
│        b0           │                       │ Hippocampus and     │
└─────────────────────┘                       │ Corpus Collosum     │
           │                                  │ Binary ROI maska    │
           ▼                                  │ in diffusion space  │
┌─────────────────────┐  ┌─────────────────┐  └─────────────────────┘
│    FSL FLIRT:       │  │ FSL convert_XFM:│  ┌─────────────────────┐
│  b0 to Anatomical   │─▶│ Invert Linear   │─▶│ FSL Applywarp:      │
│   Registration      │  │ Transform Matrix│  │ Warp Masks into     │
└─────────────────────┘  └─────────────────┘  │ Diffusion Space     │
           │                                  └─────────────────────┘
           ▼              ┌─────────────────┐
┌─────────────────────┐  │ FSL invwarp:    │
│     Anatomical      │  │ Invernt Non-Linear│
└─────────────────────┘  │ Warp Coefficients│
           │             └─────────────────┘
           ▼
┌─────────────────────┐  ┌─────────────────┐
│  FSL FLIRT  &       │  │ Extract field   │
│    FNIRT:           │─▶│ oeffieicents    │
│ Anatomical to Atlas │  └─────────────────┘
│  Registration       │
└─────────────────────┘
           │
           ▼
┌─────────────────────┐          ┌─────────────────────┐
│  Waxholm Space      │          │ Waxholm Space       │
│ Atlas of the Sprague│─────────▶│ Hippocampus and     │
│ Dawley Rat Brain    │          │ Corpus Collosum     │
└─────────────────────┘          │ Binary ROI mask     │
                                 └─────────────────────┘
```

Figure 3.7 - Complete processing and analysis steps for diffusion data.
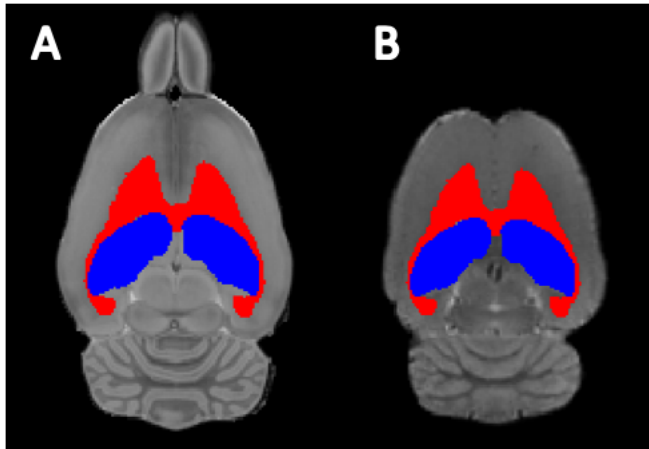
Figure 3.8 – A) Corpus callosum (Red) and hippocampus (blue) binary ROI masks generated and projected against the Waxholm Sprague Dawley Space Atlas template B) Representative corpus callosum (red) and hippocampus (blue) binary ROI masks linearly and non-linearly transformed from atlas space into diffusion space.

Chapter 4

4 Neurite Orientation Dispersion and Density Imaging (NODDI) in a Rodent Model of Repetitive Mild Traumatic Brain Injury.

4.1 Introduction

Mild traumatic brain injury (mTBI) has become a major health concern over the past few decades with a substantial increase in the awareness of the detrimental health effects associated with this injury [233]. Of particular concern is the increase in repetitive mTBI, especially amongst young athletes. Repetitive mild traumatic brain injuries can occur in athletes over the course of a sporting season and can lead to long-term debilitating symptoms, neurological impairment, and death [11,234–236]. Unfortunately, much like an initial traumatic brain injury, very little is understood about the underlying pathophysiological features of repetitive mTBI [237–239]. Current clinical tests are limited in their diagnostic and prognostic capabilities which leads to a vague understanding of the dangers associated with such injuries and limits the acceptance of legislation such as return to play guidelines for athletes [240–242]. It is important to develop unbiased patient-specific metrics that clinicians may use to diagnose, monitor, and grade the severity of repetitive mild traumatic brain injuries so that the long-term consequences associated with such injuries can be assessed.

While conventional imaging techniques such as Computed Tomography (CT) or structural magnetic resonance imaging (MRI) do not detect mTBI, advanced MRI techniques such as diffusion magnetic resonance imaging (dMRI) have shown promise in the detection and monitoring of mTBI [243–245]. Diffusion magnetic resonance imaging is a magnetic resonance imaging modality that is sensitive to the displacement pattern of water molecules in biological tissue. Many dMRI techniques provide valuable metrics by which to determine subtle changes to the tissue microstructure, the most common of which is diffusion tensor imaging (DTI) [246]. DTI has been used extensively in the study of brain injury and has shown changes in various diffusion metrics such as

fractional anisotropy (FA), mean diffusivity (MD), axial diffusivity (AD), and radial diffusivity (RD) [103,224]. While these metrics can indicate the presence and location of a change in the underlying tissue microstructure, they often require careful interpretation due to the inherently non-specific nature of DTI metrics. Thus, a more complete biophysical model is necessary to capture the vast amount of information encoded within a dMRI signal and reconstruct it in a biophysically relevant manner. To this end various reconstruction techniques have been proposed to describe the complicated microstructural environment in the brain and additionally capture various pathophysiological processes, one of which is neurite orientation dispersion and density imaging (NODDI).

NODDI applies an advanced biophysical model to partition the diffusion signal into several unique structural elements to quantify various microstructural features such as neurite density or orientation dispersion [29]. By measuring these microstructural features, NODDI is able to disentangle multiple aspects of the diffusion MR signal and monitor changes in these features independently. NODDI models three non-exchanging tissue compartments denoted as the cerebrospinal fluid (CSF), intra-neurite, and extra-neurite compartments. During signal processing, the CSF compartment is modelled as isotropic free diffusion (Gaussian) and separated from the total signal. The CSF volume fraction is captured by the NODDI metric IsoVF. The remaining signal is partitioned between the intra-neurite and extra-neurite compartments. The intra-neurite fraction is modelled as cylinders of zero-radius dispersed according to the Watson Distribution and water diffusion within this region is highly restricted and directional. Physically this represents the signal originating within the dendrites and axons and is quantified by the metric neurite density index (NDI). NDI ranges as a scalar value from 0-1. The extra-neurite fraction is modelled as hindered Gaussian diffusion and represents diffusion near neurites, and within cells bodies including various types of glial cells. Note that the extra-neurite volume fraction is simply 1-NDI, and thus the intra-neurite and extra-neurite volume fractions vary inversely and provide complementary information. Finally, NODDI provides the orientation dispersion index (ODI) metric. This index ranges from 0-1 and measures the dispersion and organization of neurites from highly coherently

organized and directional (values near 0, e.g. white matter of the corpus callosum) to widely dispersed (e.g. grey matter with values near 1).

Previous work using dMRI to study repetitive mTBI has shown that measurable changes in diffusion metrics occurs and that these often do not correlate with patient symptoms, or lack thereof [13,247,248]. Furthermore, in pre-clinical models it has been shown that repetitive mTBI's can produce altered diffusivity profiles within white matter tracts that follow a pattern of amplification analogous to a dose response to multiple hits [249]. No published studies have used dMRI to explore the immediate effects of repetitive mTBI on diffusion measurements, but pre-clinical studies have found altered diffusion profiles within 4 hours of mTBI in a rat model [176] and traumatic axonal injury (TAI) in a mouse model [21]. While the injury models differed for these studies, they highlighted the potential for dMRI to detect early changes in the microstructural environment due to injury. To our knowledge, NODDI has never been applied to any model of repetitive mTBI in either clinical or pre-clinical imaging. NODDI has been used in a select few clinical studies of traumatic brain injury and concussion, but with largely varied results. Churchill *et. al.* showed changes in NDI and ODI in various regions such as the corona radiata and corpus callosum of athletes with a previous history of concussion compared to controls [118]. Further study revealed that in athletes scanned within 7 days of a diagnosed concussion, NDI was reduced in regions such as the corona radiata and longitudinal fasciculus, and that this reduction persisted past the time that the athletes were cleared to return to play [175].

Recently, we applied NODDI and DTI in the extremely early stages of a pre-clinical model of mTBI and showed that NODDI was successfully able to detect changes in NDI and ODI within the first two hours post injury in the corpus callosum and hippocampus [250]. These changes were not detected with traditional DTI metrics, such as FA, MD, AD and RD. Thus, NODDI provides a unique opportunity to explore microstructural changes within the brain immediately following both an initial and secondary mTBI. In the current study, we aim to extend our understanding of the early stages of brain injury by applying NODDI to a pre-clinical model of *repetitive* mTBI. We hypothesize that NODDI would be sensitive to changes in the microstructural environment of rodents

within the first hour of both a primary mild traumatic brain injury and a secondary mild traumatic brain injury. Furthermore, we hypothesize that the response to the secondary impact will be greater than that observed following the initial impact. Finally, we hypothesize that NODDI metrics would be more sensitive to tissue microstructural changes than traditional DTI metrics at these early timepoints.

4.2 Methods

The injury model, imaging acquisition parameters, processing, registration, and statistical analysis methods used in the current study were identical to those listed in the previous chapter to ensure direct comparisons could be made. These sections have been repeated here for completeness.

4.2.1   Subjects

12 adult male Wistar rats (injury: n = 8, age at baseline scan: 112 ± 13 days, weight at baseline scan: 278 g ± 38 g, control: n = 4, age at baseline scan: 123 ± 24 days, weight at baseline scan: 313 ± 51 g) were acquired from Charles River. Each animal was randomly assigned to either the control or injury group. All animal procedures were approved by the University of Western Ontario Animal Use Subcommittee and were consistent with guidelines established by the Canadian Council on Animal Care. Each animal was scanned four times over 14 days according to the following timepoints: 7 days prior to injury 1 (Timepoint 1), 1-2 hours after injury 1 (Timepoint 2), 4 days after injury 1 (Timepoint 3), and 1-2 hours after injury 2 (Timepoint 4). Timepoint 4 occurred 7 days after timepoint 2.

Figure 4.1 - Timeline of data acquisition for animals randomly assigned to the injury group which received both a primary and secondary closed skull controlled cortical impact.

4.2.2   Injury

Similar to our previous study, we chose to use the closed skull controlled cortical impact (CCI) due to its pathophysiological response spectrum and thoroughly documented use in rat mTBI models [189–192]. Animals were anaesthetized by induction with 4% isoflurane followed by maintenance with 2% isoflurane. Each animal was placed in a Kopf mouse anesthesia mask (David Kopf Instruments, LLC, USA) under a traumatic brain injury device (TBI 0310, Precision Systems and Instrumentation, LLC, USA). For each impact, the device was programmed to impact at an intended depth of 3.0 mm, a velocity of 3.5 m/s and a 500-millisecond dwell time. The impact region for each animal was shaved prior to impact. Each animal received a single closed skull controlled cortical impact, centered at the sagittal suture, with a custom-made, 7 mm-diameter, pliant, silicone tip. This injury model used here is in line with previous models using closed skull controlled cortical impact to induce a mTBI [193–198]. Following controlled cortical impact animals, anesthesia was maintained at 2% isoflurane and, using an in-house built portable induction chamber, each animal was transferred to the small animal MRI facility. Control animals were anaesthetized 20 minutes prior to their MRI to match the anesthesia time between induction and scan initiation in the injured animals.

4.2.3   Acquisition

Images were acquired using a 9.4 T Bruker small animal MRI scanner at the Centre for Functional and Metabolic Mapping located within the Robarts Research Institute at the University of Western Ontario. Imaging included the acquisition of high-resolution anatomical images and NODDI in all animals. Anatomical images were acquired for each subject at the beginning of each session using a T2-weighted TurboRARE pulse sequence (8 averages, 32 slices, slice thickness = 500 μm, FOV 32 x 32 mm, matrix size 160 x 160, in-plane resolution = 200 x 200 μm, TE = 44.00 ms, TR = 7.0 s, Echo Spacing = 11.00 ms, Rare Factor 8, total acquisition time = 14 min)[199]. The NODDI diffusion sequence was incorporated into a multi-shot, spin echo, echo-planar-imaging (EPI) acquisition pulse sequence (4 shots, 32 slices, slice thickness = 500 μm, FOV 40 x 40

mm, matrix size 160 x 160, in-plane resolution = 250 × 250 μm, TE = 26.71 ms, TR = 2.5 s).

The NODDI diffusion scheme used was previously described in detail and was shown to produce reproducible and reliable results at 9.4 Tesla [200]. Briefly, a q-space sampling scheme was used across two-shells, optimized according to Caruyer *et. al.* [146], with a total of 90 directions. In shell one, 30 directions with b-value = 1000 s/mm^2 were obtained using the following diffusion gradient parameters: gradient strength (G) = 172.85 mT/m, time between the start of the first and second diffusion pulse (Δ) = 14 ms, the duration of a single gradient pulse (δ) = 4.5 ms. In shell two, 60 directions with b-value = 2000 s/mm^2 were obtained using the following diffusion gradient parameters: gradient strength (G) = 345.70 mT/m, time between the start of the first and second diffusion pulse (Δ) = 14 ms, the duration of a single gradient pulse (δ) = 4.5 ms.   Ten b = 0 s/mm^2 were interspersed evenly throughout the acquisition. Four averages were used to ensure adequate signal to noise ratio (SNR) in the higher b-value shell. The imaging time for each acquisition (four averages) was 66 minutes 36 seconds. A single reverse phase encoded b=0 volume was also acquired prior to the diffusion sequence for subsequent use in image processing to correct image distortions.

4.2.4   Processing

Brain masks were produced using the 3D Pulse Coupled Neural Network (PCNN) tool for MATLAB (R2019a) [150]. Raw data were pre-processed using fMRI Software Library (FSL, v. 6.0.1, Oxford, UK). TOPUP [148] followed by EDDY [149] was used to correct for eddy current induced distortions as well as susceptibility-induced distortions. The FDT toolbox (v. 5.0) was used to produce maps of FA, MD, AD, and RD. The NODDI Matlab toolbox (available from the University College London (UCL) Microstructure Imaging Group) was then used to produce maps of NDI, ODI, and IsoVF. All diffusion maps were produced within each subject's native diffusion image space. While IsoVF is produced during the processing steps, our previous work has indicated it to have extremely high variability and low reproducibility with this scan protocol and therefore we limit our analysis to NDI and ODI only.

4.2.5   Registration

For each subject, the first volume in each diffusion data set (b = 0) was aligned with its corresponding anatomical images using a linear registration in FSL (FLIRT) [151]. The anatomical image for each subject was then aligned to the Waxholm Space Atlas Sprague Dawley template [152] using a linear transformation (FLIRT) followed by a non-linear transformation (FNIRT) [153] in FSL. Binary ROI masks of the corpus collosum and hippocampus from the Waxholm Space Atlas, were then transformed into the anatomical space of each individual subject by inverting the preceding non-linear transformations. Finally, the masks were brought into diffusion space using the inverse transformation matrix from the b0 image to anatomical image registration. Thus, each mask was brought into each subject's individual native diffusion image space. Each mask was then eroded by a single voxel around the edges to avoid partial volume effects. Masks were visually inspected to ensure accuracy. Please refer to 3.7 for processing steps and representative visualizations of ROI binary masks.

4.2.6   Statistical Analysis

For each subject, at each timepoint the mean value of each individual scalar metric within each relevant ROI was extracted using fslstats and the relevant binary mask. A mixed ANOVA in SPSS [201] was used for each metric to determine if there were statistically significant interaction effects ($p < .05$) between controls and injured animals over time. This test examined whether each metric changed over time and whether those changes were different between the two groups. Mauchly's Test was used to determine if the assumptions of sphericity were violated. In cases where the assumption of sphericity was rejected, the Greenhouse-Geisser correction was used. In each case where a statistically significant interaction effect occurred, a follow-up repeated measures ANOVA was run separately on each group (injured and controlled) to determine if there were statistically significant changes ($p < .05$) in the diffusion metric over time within each group. Further, post-hoc analysis was used to determine which timepoints differed within each group (Bonferroni corrected). Finally, in an effort to determine if the response to each hit differed in those metrics which showed a statistically significant change from baseline, a

paired t-test on the response to injury 1 and injury 2 was used. The response to injury 1 was defined as the difference between timepoint 1 and 2, while the response the injury 2 was defined as the difference between timepoint 3 and 4.

4.3 Results

Data were successfully acquired from all 12 subjects. Figure 4.2depicts single subject raw data, NODDI scalar maps, and DTI scalar maps. The following timepoints were used in this study: Timepoint 1 (or baseline scan) obtained 7 days prior to injury, Timepoint 2 began at 62 ± 14 minutes post-injury 1, Timepoint 3 began at 98 ± 3 hours post-injury, and Timepoint 4 began at 66 ± 11 minutes post-injury 2.
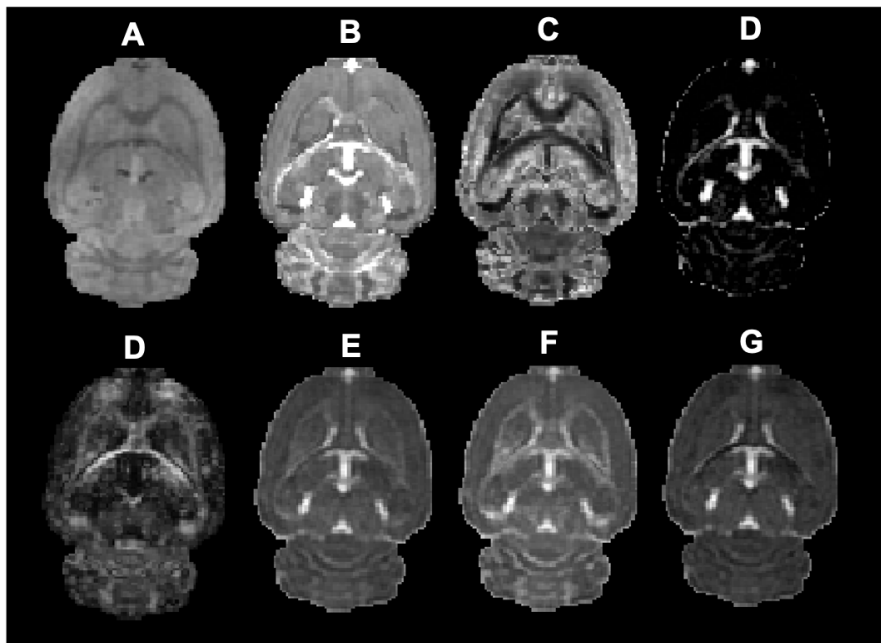
Figure 4.2 - Single-subject axial slices of A) raw diffusion data B) Neurite Density Index (NDI), C) Orientation Dispersion Index (ODI), D) Isotropic Volume Fraction (IsoVF), E) Fractional Anisotropy (FA), F) Mean Diffusivity (MD), G) Axial Diffusivity H), Radial Diffusivity. The diffusion images were acquired with a multi-shell sequence (10 b= 0 s/mm², 30 b = 1000 s/mm² and 60 b= 2000 s/mm²) incorporated into a multi-shot, spin echo, echo-planar-imaging (EPI) acquisition pulse sequence (4 shots, 32 slices, slice thickness = 500 μm, FOV 40 x 40 mm, matrix size 160 x 160, in-plane resolution = 250 × 250 μm, TE = 26.71 ms, TR = 2.5 s).

4.3.1 Corpus Callosum
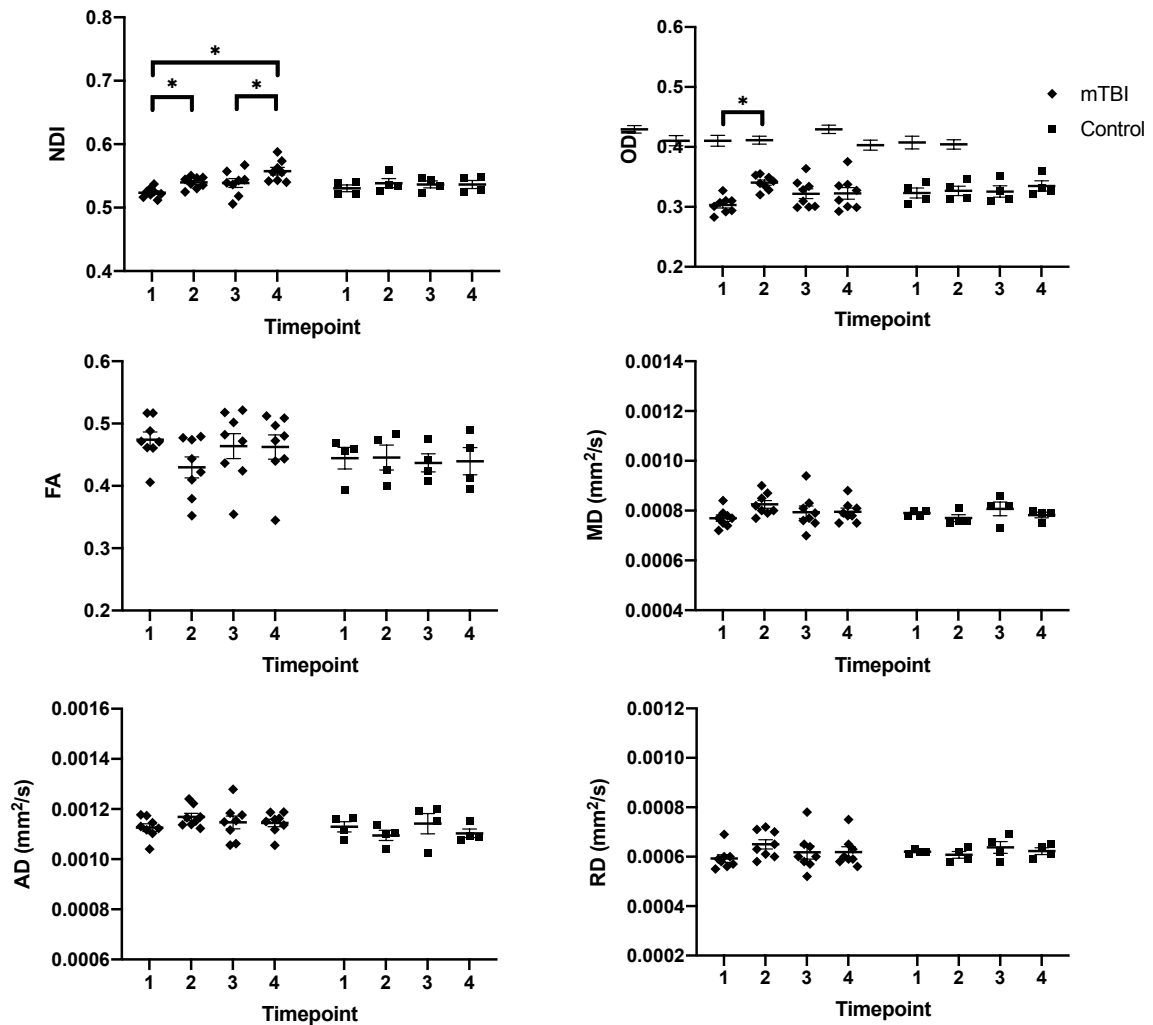
Figure 4.3 – Mean ROI metrics within the corpus callosum for injured and control subjects. Each data point depicts the mean value of an individual subject ± SEM. Note, injury 1 took place at timepoint 1 and injury 2 took place at timepoint 4. For NDI and ODI in the corpus callosum a mixed effects ANOVA in SPSS showed a statistically significant group by time interaction (p < .05). A repeated measures ANOVA was then used to determine individual differences amongst the injured and control groups. Post-hoc pairwise comparisons (Bonferroni corrected) were then determined between individual timepoints within each group. Statistically significant (p < .05) pairwise differences are indicated by *.

In the Corpus Callosum, there was a statistically significant (p < .05) group by time interaction effect for NDI [$F(3,30) = 4.161$, p = .033, Greenhouse-Geisser corrected] and

ODI [F(3,30) = 3.851, p = .047, Greenhouse-Geisser corrected]. There was no statistically significant interaction effect (p > .05) of group by time for FA, MD, AD and RD.

From the subsequent univariate repeated measures ANOVA, it can be seen that for both NDI and ODI there was a statistically significant change over time for the injured group, while no statistically significant change over time occurred within the control group for these metrics.

Table 4.1 - Mean ROI diffusion metrics that were shown to be significantly different between injured and control subjects. Values shown are mean ± SD.

Metric	Timepoint	Injured	Control
NDI	1	0.524 ± 0.008	0.530 ± 0.010
	2	0.540 ± 0.009	0.539 ± 0.014
	3	0.539 ± 0.020	0.537 ± 0.011
	4	0.558 ± 0.017	0.536 ± 0.013
ODI	1	0.303 ± 0.014	0.323 ± 0.017
	2	0.340 ± 0.012	0.327 ± 0.015
	3	0.322 ± 0.023	0.326 ± 0.016
	4	0.322 ± 0.027	0.325 ± 0.019

Table 4.2 - Statistical Results of a repeated measures ANOVA for NDI and ODI within the corpus callosum. All statistical analysis was run in SPSS (v. 26).

Metric	Statistical Results			
NDI	Injured	F (3,21) = 13.618	p = .001	Greenhouse-Geisser
	Control	F (3,9) = 1.318	p = .328	Sphericity Assumed
ODI	Injured	F (3,21) = 9.504	p = .000	Sphericity Assumed
	Control	F (3,9) = 3.431	p = .066	Sphericity Assumed
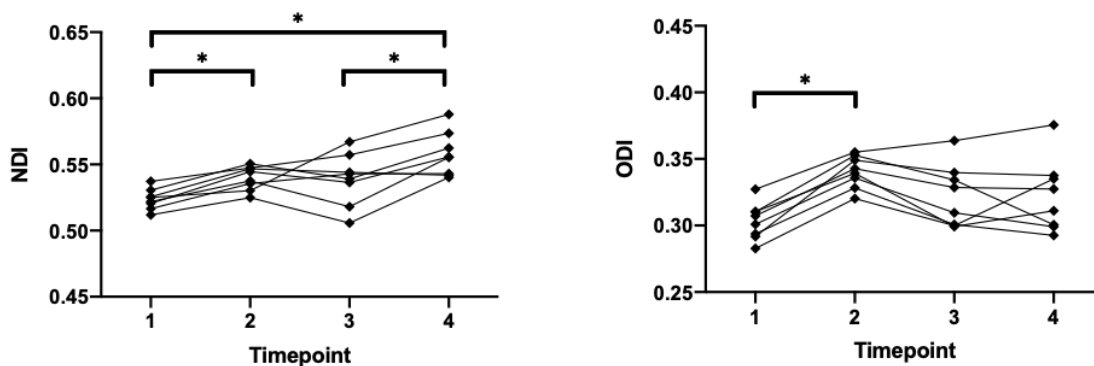
Figure 4.4 - Mean ROI values in the injured group of NDI and ODI within the corpus callosum. Note, injury 1 took place at timepoint 1 and injury 2 took place at timepoint 4. For every individual subject in the injured group, an increase in both NDI and ODI occurred from baseline to the first mTBI. Following this individual response varied across the subsequent timepoints.

Similar to our previous study, it can be seen that for every individual subject both ODI and NDI increased after the initial mTBI. Using and two-tailed paired t-test it was shown that for NDI there was no statistically significant difference in the response to injury 1 and injury 2 in the corpus callosum (p = .68). For ODI there was a statistically significant difference in the response to injury 1 and injury 2 (p =.00)

Table 4.3 – NDI and ODI values for each subject in the corpus collosum of the injured group. There was no statistically significant difference between Δ_1 and Δ_2 for NDI indicating a similar response to injury 1 and injury 2. For ODI a statistically significant difference between Δ_1 and Δ_2 existed (p =.00).

Metric	Subject	Injury 1			Injury 2		
		Timepoint 1	Timepoint 2	Δ_1	Timepoint 3	Timepoint 4	Δ_2
NDI	1	0.517	0.536	0.019	0.543	0.543	0.000
	2	0.531	0.551	0.020	0.539	0.562	0.023
	3	0.521	0.545	0.024	0.536	0.556	0.019
	4	0.526	0.547	0.021	0.544	0.542	-0.002
	5	0.512	0.525	0.013	0.506	0.540	0.0346
	6	0.522	0.538	0.016	0.518	0.555	0.0373
	7	0.525	0.530	0.005	0.567	0.588	0.0208
	8	0.537	0.547	0.010	0.557	0.574	0.0163
Mean		0.524 ± 0.008	0.540 ± 0.009	0.016 ± 0.006	0.539 ± 0.020	0.558 ± 0.017	0.019 ± 0.014
ODI	1	0.282	0.320	0.037	0.300	0.335	0.035
	2	0.307	0.343	0.035	0.329	0.327	-0.001
	3	0.301	0.336	0.034	0.310	0.299	-0.010
	4	0.310	0.353	0.042	0.334	0.301	-0.034
	5	0.310	0.339	0.029	0.299	0.311	0.012
	6	0.294	0.328	0.035	0.301	0.293	-0.008
	7	0.327	0.355	0.028	0.364	0.376	0.012
	8	0.292	0.349	0.057	0.340	0.338	-0.002
Mean		0.303 ± 0.014	0.340 ± 0.012	0.037 ± 0.009	0.322 ± 0.023	0.322 ± 0.027	0.004 ± 0.020

4.3.2 Hippocampus
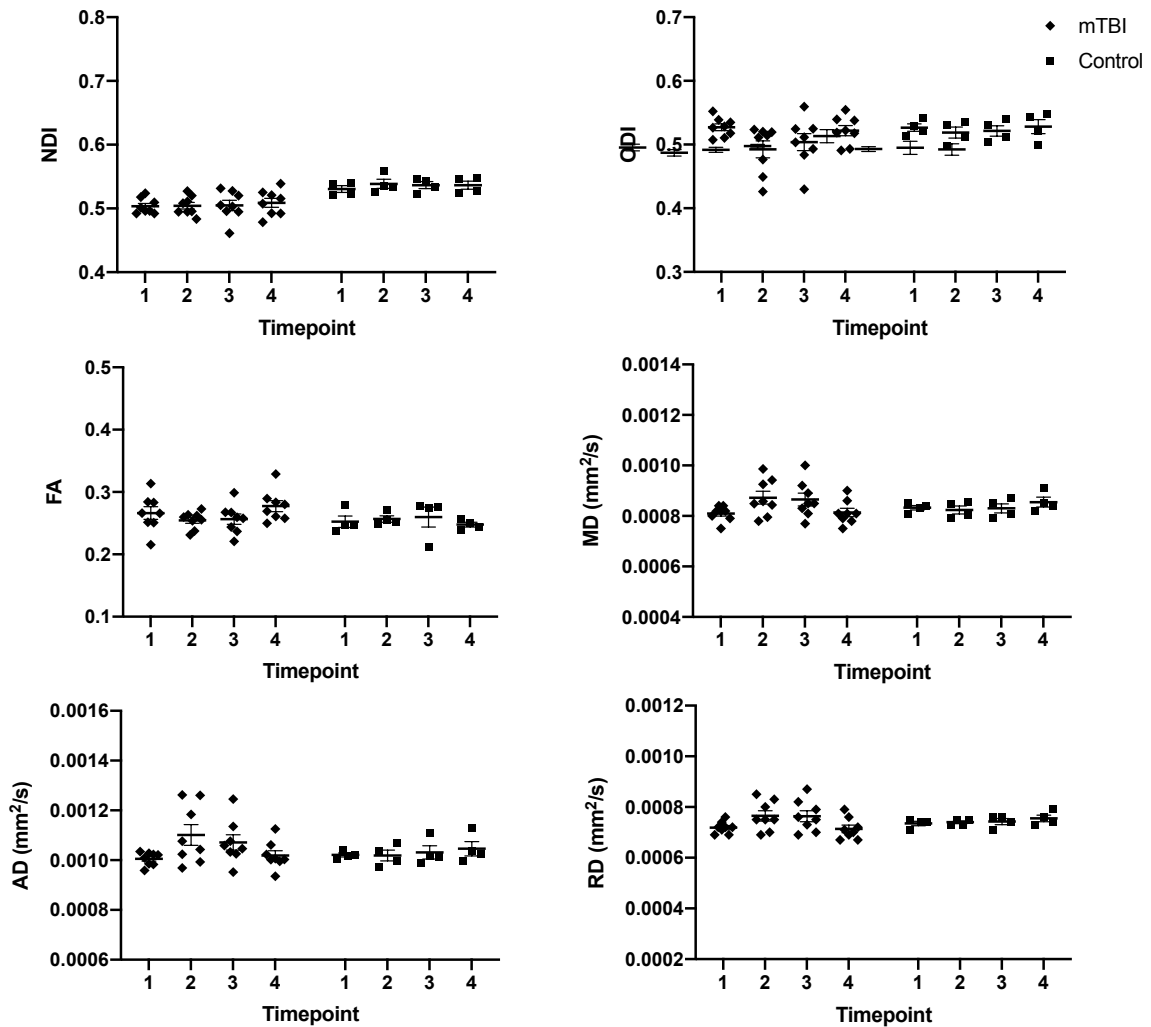
Figure 4.5 - Mean ROI metrics within the hippocampus for injured and control subjects. Each data point depicts the mean value of an individual subject ± SEM. Note, injury 1 took place at timepoint 1 and injury 2 took place at timepoint 4. No statistically significant group by time interactions (p > .05) were detected.

In the hippocampus, there was no statistically significant interaction effect (p > .05) of group by time for NDI, ODI, FA, MD, AD and RD. As no group by time interaction effect occurred in the hippocampus no subsequent statistical analysis was performed. Please refer to Figure 4.5 for ROI values.

4.4 Discussion

This study examined the immediate changes in NODDI and DTI metrics in a rodent model of repetitive mild traumatic brain injury. The NODDI metrics NDI and ODI showed statistically significant increases in the corpus callosum within the first two hours after the initial mTBI, while only NDI showed a further increase immediately following the second mTBI one week later. There were no changes in any diffusion metrics in the hippocampus. The increase in NDI in the corpus callosum suggests a change in the microstructural environment immediately following each mTBI. However, converse to our hypothesis, there were no changes in diffusion metrics that were greater following the second injury compared to the first injury on a group level. Interestingly, individual response to the second mTBI varied substantially.

Neurite density index (NDI) was shown to increase immediately following the initial mTBI and the second mTBI in the corpus callosum. Following the initial injury, an average increase in NDI of 0.016 ± 0.006 (3.22%) was found and following the second injury and average increase of 0.0187 ± 0.014 (3.41%). This result agrees with our previous study which also showed an increase of 0.046 ± 0.026 (7.83%) in NDI compared to baseline in the corpus collosum [250]. Further, it was shown that the response to injury 1 did not significantly differ from the response to injury 2 in the corpus collosum. When referring to the mean values of NDI over time we see (in order): 0.524, 0.540, 0.539, 0.558 (refer to

Table 4.3). From this we may infer that the pathophysiological response that NDI has measured did not resolve between injury 1 and injury 2 (noting there was no significant difference between timepoint 2 and 3), and that the second injury in fact compounded on the first with equal magnitude. This finding could provide a clue as to the dose-like effect of multiple mTBI's often seen in the clinical setting.

Common interpretations of increased NDI suggest an increase in the volume or number of dendrites and axons within the corpus callosum. The most likely explanation would be an increase in the inner diameter of axons due to axonal swelling and beading. Axonal swelling and beading have been shown by ex-vivo histology as a common microstructural change in mTBI [167,251,252]. In addition, these pathological processes have been shown to occur within as little as thirty minutes following injury in mTBI models [56,171]. Therefore, the increase in NDI following both the first and second mTBI in the current study could be due to these processes. Furthermore, in the current study it was shown that four days after the initial impact, NDI was not statistically different than baseline, suggesting that the effect of the initial mTBI on NDI had, at least in part, resolved in the intervening time.

While the NODDI biophysical model technically encompasses strictly the tissue components of the microstructure, there are significantly more components contained within the diffusion signal. Specifically, the various constituents in the extra-neurite compartment must be considered as this is inversely related to NDI (e.g. an increase in NDI could be due to a decrease in the extra-neurite space). Blood brain barrier disruption been extensively shown in mTBI and this disruption has been shown to occur as early as minutes after injury in pre-clinical studies [208–211]. This disruption compromises the ability of the BBB to restrict passage of various factors such as blood borne proteins from entering the extra-neurite space [38,212]. As these enter the extra-neurite space surrounding neurons, they could contribute to diffusion changes that are measured as a

reduction in the extra-neurite space, thus contributing to the increases observed in the NDI measurement.

Neuroinflammatory processes have been heavily implicated in the initial and long-term response to mTBI [72,253,254]. It has been shown that the response is complex, at times acting in a neuroprotective manner, and others in a neurodegenerative manner [255–257]. Furthermore, as shown in Figure 3, it appears that the NDI response and its outcome vary dramatically on an individual basis, consistent with the heterogeneous individual response to mTBI seen in patients [258,259]. In the current study it is possible that increased glial cells within the extra-neurite compartment contributed to a decrease in the volume of the extra-neurite compartment. As the extra-neurite and intra-neurite NDI components must sum to unity, this would lead to the measured increase in NDI apparent here. Additionally, the glial cell response has been shown to occur minutes after injury in various brain injury models such as TBI and BBB disruption [216–219]. Once again, these processes could lead to a reduction in the extra-neurite compartment and the measured NDI increase. Of particular interest in the discussion is the heterogeneous response of NDI in individuals following the first mTBI. While each individual subject showed an increase in NDI following the initial hit, the changes observed on day four varied widely amongst individuals. As discussed in our previous paper, while the relationship between NDI and neuroinflammation is an interesting possibility, a detectable glial response is more commonly thought to begin within 3-6 hours post mTBI [220,221] and further confirmation through histology would be needed to support this interpretation.

Orientation dispersion index (ODI) also increased in the corpus callosum from baseline to our initial timepoint post injury consistent with our previous study. Following the initial injury, an average increase in ODI of 0.037 ± 0.009 (10.88%). This increase was no longer present four days after impact. Interestingly, there was no further increase in ODI following the second mTBI. As described previously, the increase in ODI following the first injury indicates an increase in the dispersion of white matter tracts within the corpus callosum, leaving them less ordered along their predominant fiber direction. Axonal disorganization has been heavily implicated in mTBI, showing altered anisotropy

amongst fiber bundles and decreased alignment [260–262]. There are several other potential explanations for this change including the infiltration of blood constituents to the extra-neurite space, although there is currently no literature exploring the relationship between ODI and BBB disruption. Additionally, it has been shown that an increase in glial cell load correlates to an increase in ODI and thus it is possible that a neuroinflammatory response may account for the measured changes [222]. However, as discussed previously it is unlikely the glial response accounts for the measured signal change at the very early time point examined in the current study. Here again it is extremely important to acknowledge the heterogenous ODI response following the initial timepoint. Following the initial mTBI, the measured changes in ODI on an individual basis (Figure 3) vary substantially potentially indicating a varied individual response to trauma.

No statistically significant changes were observed in NDI or ODI in the hippocampus. This result was surprising as our previous study detected an increase in NDI but not ODI immediately following a single mTBI. It should be noted though that while the previous increase in NDI in the hippocampus was statistically significant, the magnitude was only 0.022 ± 0.021 (3.93%) at the earliest timepoint. Further, the earliest timepoint in our previous study began at 75 ± 16 minutes, while in the current study the earliest timepoint began at 62 ± 14 minutes. While this is not a large time difference in relation to the overall scan time of 66 minutes, it is possible that at these extremely early timepoints and the very small magnitude of change, the NDI changes observed in the first study did not have time to develop in the current study. Future studies would benefit by looking into this change with larger sample sizes and precisely matched timepoints.

It is also noteworthy that no statistically significant changes were observed in any DTI metrics in the corpus callosum or hippocampus following either the first or repeated mTBI. This agrees with our previous findings indicating that using the current scan protocol DTI lacks the sensitivity to detect diffusion changes immediately following mTBI [250].

4.5 Limitations

While dMRI techniques are highly sensitive to subtle changes in diffusion parameters, the results must be carefully interpreted to make inferences with regard to the underlying microstructural changes [263,264]. NODDI uses a biophysical model to partition the diffusion signal into physically relevant compartments, but still requires interpretation as it does not account for various constituents of the extra-neurite compartment such as glial cell contribution to the diffusion signal. In the current study we have provided possible biological explanations that could contribute to the measured signal changes, but these would require careful histological validation. It may also be possible in the future to partition the NODDI model further, thus separating out the unique diffusion characteristics of glial cells such as microglia and astrocytes. This would prove immensely valuable in the study of brain injury and neurodegeneration, of which neuroinflammation has been heavily implicated. Furthermore, it should be noted that while NODDI has been heavily validated for human studies at clinical field strengths, some characteristics such as axon diameter dependency in rodents at ultra-high fields have not been expressly explored. While we have shown these metrics to be reproducible in a rodent model at 9.4 Tesla, it would be useful to further validate the metrics specifically at this field strength [200].

The current injury protocol did not take into account careful examination of the kinematic properties of the injury, such as sheer forces and acceleration. Additionally, no behavioural measures were taken to determine cognitive defects associated with this injury. When observing the heterogenous individual response to the second injury in this model, it would be extremely valuable to have this additional information, such that any covariance in the injury model may be accounted for. While the impact was consistent amongst subjects, adding this covariance could account for individual differences in the result of that impact. Finally, it would be beneficial to track these subjects for several weeks following repetitive mTBI's to determine long-term outcomes and relate to the individual responses seen in the current study. This in turn could shed light on the immense variance seen in terms of recovery in the clinical patient population.

4.6 Conclusions

NODDI was successfully able to detect changes in NDI and ODI in the brain of rodent's immediately following a first and a second closed skull controlled cortical impact. The measured changes largely did not differ between the first and second impact when comparing groups but varied dramatically on an individual basis. This leads us to conclude the immediate response to repetitive mTBI is extremely heterogeneous and could provide clues with regard to the varied recovery rates evident in the clinical patient population.

Chapter 5

5 Summary and Conclusions

5.1 Overview and Research Questions

Mild traumatic brain injury (mTBI) is known to contribute to a diverse range of short- and long-term detrimental health effects, ranging from nausea and dizziness to extreme memory loss, mental health issues, and death [44,265,266]. Currently, there is no pathognomonic test that allows clinicians to diagnose, assess the severity, or monitor the recovery of patients suffering from a mTBI. Most medical imaging techniques are unable to detect mTBI as large scale changes such as expanding epidural hematoma are not present [5,6]. Further, it is nearly impossible to study the immediate changes in a clinical setting because patients simply are not available to study during this time period. Thus, the complete pathological response occurring in the early stages of mTBI is still largely unknown, limiting diagnosis, prognosis, and development of treatment.

One medical imaging modality that has shown promise in the detection of microstructural changes in mTBI is neurite orientation dispersion and density imaging (NODDI). NODDI is a biophysical modelling technique that separates a dMRI signal into three unique compartments termed the intra-neurite, extra-neurite, and CSF compartments [30]. This model allows detection of microstructural changes, such as axonal beading, separate from changes within the extra-neurite compartment, such as neuroinflammatory effects, providing a unique imaging perspective on the various pathological processes taking place in the immediate stages following mTBI.

The overreaching objective of this thesis was to apply NODDI in the early stages of a rodent model of mTBI at 9.4 Tesla in an effort to understand and quantify the pathophysiological response to mTBI. Specifically, this thesis addressed three main research questions: 1) What is the scan-rescan reproducibility of NODDI in a rat model at 9.4 Tesla, and what biological effects is NODDI capable of detecting with feasible pre-clinical sample sizes? (Chapter 2); 2) Is NODDI capable of detecting changes within

early stages of a rat model of mTBI, and if so, what underlying physiological processes do they represent? (Chapter 3); and 3) Is NODDI capable of detecting changes immediately following both a first and second injury in a rodent model of mTBI, and is this response to injury different (Chapter 4)?

5.2 Chapter Summaries and Significance

5.2.1 Chapter 2

In Chapter 2, the reproducibility of NODDI in a rodent model at 9.4 Tesla was evaluated. Eight adult male Sprague Dawley rats were subjected to a scan-rescan protocol on a 9.4 Tesla Agilent MRI. The coefficient of variation (CV) was used to assess the reproducibility and reliability of NODDI and provide insight into necessary sample sizes and the minimum detectable effect size. NDI and ODI showed high reproducibility both between and within subjects under both a voxel-wise and ROI analysis. Furthermore, it was found that small biological changes (< 5%) may be detected with feasible sample sizes (n < 6-10). In contrast, IsoVF was found to have low reliability and reproducibility, requiring very large sample sizes (n > 50) for biological changes to be detected. This work represents the first publication quantifying the reproducibility of NODDI metrics at 9.4 Tesla in a rat brain and provides valuable insights as to the number of subjects necessary to detect a given biological effect.

5.2.2 Chapter 3

With NODDI shown to be reproducible and capable of detecting subtle changes with feasible sample sizes, NODDI was applied to a rodent model of mTBI to determine whether microstructural changes could be detected immediately following injury. Secondary to this we sought to compare the sensitivity of NODDI metrics to standard DTI metrics in this model. Nine adult male Wistar rats underwent a single closed skull controlled cortical impact followed immediately by NODDI repeated three times from 1-4 hours post injury. Six sham control rats were scanned under the same conditions without injury. ROI analysis showed a statistically significant increase in NDI in both the

hippocampus and corpus callosum following injury, while ODI showed an increase in only the corpus callosum. These changes occurred at the first timepoint post-injury ($\approx$ 1 hour) and stayed elevated through the final timepoint ($\approx$ 4 hours). No statistically significant changes were observed in the sham control animals for NDI, nor ODI. No statistically significant changes were found in FA, MD, AD, or RD metrics in either group. These metrics indicate an immediate change to the microstructural architecture in the brain following mTBI and provide insight into the pathophysiological response to injury. Further, these results indicate that NODDI metrics are more sensitive than DTI metrics to early microstructural changes in the current injury model. This study represented the first application of NODDI to a pre-clinical rodent model of mTBI at 9.4 Tesla, and the first study to investigate alterations in diffusion metrics within the first 4 hours post-mTBI.

5.2.3   Chapter 4

In Chapter 4, we extended this model of mTBI to determine the response to repetitive mTBI in a rodent model using NODDI. Eight adult male Wistar rats underwent two closed skull controlled cortical impacts followed immediately by a NODDI acquisition 1-2 hours post injury. The impacts were separated by one week. Animals were scanned at four separate timepoints: 1 week before injury, immediately following the first mTBI, four days following the first mTBI, and immediately following the second mTBI. In injured animals, both NDI and ODI showed a statistically significant increase immediately following the first mTBI in the corpus callosum. NDI showed a similar increase following the second mTBI in the corpus callosum while ODI did not. No statistically significant changes were observed in the hippocampus of injured animals nor any region in the sham control animals. Furthermore, no statistically significant changes were found in FA, MD, AD, or RD metrics in either group. The observed changes support our previous findings showing an immediate change to the microstructure of the

brain following an initial mTBI and suggest further disruption of the tissue microstructure following the second mTBI. Of particular note in this study was the heterogeneous individual response to injury following the second mTBI. This finding could provide insight into the widely varied outcomes and recovery amongst the clinical population exposed to multiple mTBI. This study represented the first application of NODDI to a pre-clinical rodent model of repetitive mTBI at 9.4 Tesla, and the first study to investigate alterations in diffusion metrics immediately following mTBI in any application.

5.3 Limitations

In this section, I discuss the major limitations of the chapters individually followed by a discussion of general limitations of the thesis.

5.3.1   Chapter 2

There are several limitations to acknowledge within this study, the first of which is the fact that the quality of the linear and non-linear registrations was not specifically quantified. While they were visually assessed for quality, future studies may benefit from quantification of the registration process with Dice index analysis [227]. Secondly, optimized parameters such as angular resolution, image resolution, and b-value combination for rodent NODDI at 9.4 Tesla has not been fully explored. While these considerations must be balanced against practicalities such as scan time for any *in-vivo* study, it would be beneficial to do a thorough quantification and comparison of these parameters. In humans, the optimal b-values were explored through simulation and *in-vivo* study, and it was found that as long as two shells with moderate b-value were used, the precise choice of b-value made minimal difference and was minimally affected by axon diameter [29]. Future studies would benefit from a similar analysis within a rodent brain at 9.4 Tesla.

5.3.2 Chapter 3 and 4

These chapters follow the same experimental protocol and thus have the same limitations. Similar to Chapter 2, these studies suffer from lack of image registration quantification and NODDI parameter optimization. Additionally, they are limited by the absence of histological validation. As the NODDI reconstruction is limited to a 3-compartment model, it fails to uniquely account for contributions from pathophysiological processes such as blood-brain barrier disruption or glial cell response. It could be that these processes contributed to the changes observed in this study, but without histological validation, any interpretation is uncertain. Future studies would benefit from a careful histological analysis. Additionally, no behavioral measures were acquired to determine if the injury model used did in fact produce a mTBI. The varied response on an individual level could possibly be explained in part by behavioural analysis of the subjects. Finally, while the controlled cortical impact was landmarked and standardized for each injury, no metrics were obtained quantifying kinematic properties such as rotation and translation of the head. These metrics could be integral in further explaining sources of variation in the resulting NODDI metrics.

5.3.3 General Limitations

Over the course of this thesis, significant upgrades took place within the lab, one of which was the upgrade from an Agilent 9.4 Tesla scanner to a Bruker 9.4 Tesla scanner. Thus, the work in Chapter 2 was performed on the former system while the work in Chapter 3 and 4 was performed on the latter system. This included entirely new hardware, software, pulse sequences, data storage, and raw data reconstruction. Basic SNR calculations were performed on a small number of data sets showing improved SNR with the Bruker system ($\approx 20\%$), but a thorough quantification of NODDI performance between the two systems was not performed. It should also be noted that in Chapter 2, Sprague Dawley rats were used, while in Chapter 3 and 4, Wistar rats were used due to protocol limitations. While we do not anticipate a large change in results between the two strains, it is important to note the difference.

5.4 Future Directions

5.4.1   NODDI Optimization at 9.4 Tesla

In Chapter 2 of this thesis, NODDI was shown to be reproducible and sensitive to small changes in NDI and ODI metrics. Although this allowed these parameters to be used for future studies, it is currently unknown if they are in fact the optimal parameters. As such the optimization of the NODDI acquisition at 9.4 Tesla would provide a valuable framework for future studies. Specifically, this study would focus on the optimization of angular resolution, b-value magnitude, and b-value distribution amongst and between shells. Furthermore, this would provide optimized protocols under set scan times, which could be achieved on common 9.4 Tesla preclinical scanners. The same approach used to optimize NODDI acquisition in humans could be applied to optimize the acquisition in rodents [29,267]. This work would provide a road map for researchers to apply NODDI to extensive preclinical applications.

5.4.2   Histological Validation of NODDI Metric Changes Observed
Following mTBI

As stated in both Chapter 3 and 4, the major limitation in these studies involves interpretation of the observed changes in NODDI metrics. To overcome this, careful histological validation would be necessary to confirm these findings. We propose repeating these studies with a larger cohort and a greater histological focus. Specifically, we propose amyloid precursor protein (APP) immunohistochemistry and silver staining to characterize axonal pathology [195], ionized calcium-binding adaptor protein-1 (IBA-1) immunohistochemistry to characterize microglial activation [268], Glial fibrillary acidic protein (GFAP) to detect astrogliosis [269,270], and the evaluation of BBB disruption through the use of Immunoglobulin G (IgG) staining [271] and Evans Blue extravasation assay [272]. By performing each of these stains, we would be able to disentangle the information contained in the NODDI metrics, leading to a more thorough understanding of how the pathophysiological response contributes to these changes.

5.4.3 Combined PET/MRI to Visualize Microglial Activation in mTBI

Microglial activation has been shown as an important neuroinflammatory response to brain injuries such as mTBI [73,273]. Activation can occur within hours and persist many years, often occurring at sites of neuronal degeneration and axonal alterations [274–276]. As such, non-invasive *in-vivo* imaging of microglial activation presents a unique possibility to measure a component of the neuroinflammatory response to injury. The PET ligand [^{18}F]-DPA-714 binds with high specificity to TSPO, an 18-kDa translocator protein [277]. Activation of microglia leads to increased mitochondrial TSPO expression, while expression of TSPO under normal physiological conditions is relatively low and restricted to specific regions [278,279]. Due to the specific binding affinity, ability to cross the blood-brain barrier, and negligible levels of endogenous [^{18}F]-DPA-714, it is a prime candidate to visualize the activation of microglia *in-vivo* in mTBI [280]. The use of combined PET/MRI allows for high-resolution anatomical imaging using MRI, while obtaining the dynamic pathophysiological information from PET. Immediately following imaging, animals would be sacrificed and immunohistochemistry staining (Iba-1) would be used to verify and localize activation of microglia.

The ability to dynamically image microglial activation will allow for repeated-measures, longitudinal studies of various normal and pathological processes, which has previously been impossible within histological studies. This in turn could lead to a more thorough and accurate understanding of the development and response of the central nervous system.

5.4.4 *In-vivo* Imaging of Glial Cells using Diffusion Weighted MRI

Glial cells are the most abundant non-neuronal cell type within the central nervous system (CNS) [33]. These cells provide extensive support throughout the brain and spinal cord through the maintenance of homeostasis and various supporting activities for the neuron [35]. As discussed in this thesis, glial cells are heavily implicated in the response to mTBI. Although extensive histological techniques have been developed to visualize glial cell load and morphology *ex-vivo*, *in-vivo* techniques are sparse. Here, we propose

the use of diffusion weighted MRI to dynamically visualize and quantify glial cells *in-vivo* in rodents.

Diffusion weighted MRI would be acquired on an ultra-high field (9.4 Tesla) small animal scanner. To reconstruct the signal, we would follow the method employed in the NODDI toolbox (available from the UCL Microstructure Imaging Group) with a modification to extract the unique contribution from the glial cell compartment. Thus, the total diffusion signal would be separated into four non-exchanging microstructural compartments: the intra-neurite fraction (volume fraction of water within the axons and dendrites), the extra-neurite volume fraction (volume fraction of water near neurons), the CSF volume fraction (volume fraction of isotopically free diffusing water), and the glial volume fraction (volume fraction of water within the glial cells). While some studies have shown the contribution of glial cells to these compartments [222], we currently are not aware of any techniques which expressly define the glial cell contribution uniquely. Due to the size (approximately one tenth the size of a neuron), we expect diffusion to be minimal and non-directional within glial cells, leading to high diffusion signal in regions of high glial cell load. This diffusion pattern is unique within the microstructural environment when compared to neurons and dendrites (highly restricted and directional), the extracellular space (hindered and directional), and the CSF (free, non-directional). Initially, simulations could be employed based on those described in [267,281] to determine optimal diffusion acquisition parameters based on known glial cell structure. These parameters would then be applied to *in-vivo* rodent models of mTBI. Immediately following acquisition, animals would be euthanized and perfused in preparation for histology. Established histological stains such as Iba-1 and GFAP would be used to detect the presence of glial cells. Reconstructed diffusion images would then be registered and validated against histological images. The use of diffusion weighted MRI here will address the significant gap that exists between *ex-vivo* and *in-vivo* capabilities of imaging glial cells.

5.5 Significance and Impact

mTBI is a diverse and challenging injury to diagnose. Clinical presentations vary dramatically, as do patient outcomes [4,265,282]. To this point, the scientific literature with regard to mTBI is largely divergent, except to show the potential for debilitating and damaging health effects [2,283]. While these health effects are well known now, the underlying pathophysiological processes that produce these effects are largely unknown. Without a clear understanding of these processes it is impossible for clinicians to accurately diagnose and assess mTBI in patients. Neurite orientation dispersion and density imaging provides an opportunity to study these microstructural changes *in-vivo*.

This thesis advances the capabilities of NODDI in a pre-clinical model of mTBI. When this work began, only a single publication had applied NODDI in a preclinical setting [144], but the reliability and reproducibility of the technique in this setting was unknown. We have provided, for the first time, quantification of the reproducibility of this technique at 9.4 Tesla and provided details with regard to the measurable biological effect's detectable with this technique. This information will enable researchers to similarly apply this technique to countless pre-clinical models of neuronal health, disease, and injury.

Simultaneously, this thesis advances our understandings of the early microstructural changes present in mTBI. Clinically it is impossible to study these changes for the first several hours following a brain injury as patients rarely present early following injury and if they do, they cannot be kept in a scanner for any appreciable length of time. This thesis presents the first application of NODDI in a pre-clinical rodent model of both initial and repetitive mTBI at 9.4 Tesla. We have provided, for the first time, *in-vivo* evidence of changes in NODDI metrics detectable within the first hour following both an initial and secondary mTBI in a rodent model. These changes indicate detectable underlying microstructural changes that occur rapidly after a mTBI. This knowledge indicates the potential of NODDI to be further developed into a diagnostic imaging technique capable of quantifiably detecting mTBI *in-vivo*.

References

1. Marshall S, Bayley M, McCullagh S, Velikonja D, Berrigan L. Clinical practice guidelines for mild traumatic brain injury and persistent symptoms. Can Fam Physician. 2012;

2. Rosenbaum SB, Lipton ML. Embracing chaos: The scope and importance of clinical and pathological heterogeneity in mTBI. Brain Imaging and Behavior. 2012. doi:10.1007/s11682-012-9162-7

3. Lumba-Brown A, Yeates KO, Sarmiento K, Breiding MJ, Haegerich TM, Gioia GA, et al. Centers for Disease Control and Prevention Guideline on the Diagnosis and Management of Mild Traumatic Brain Injury among Children. JAMA Pediatrics. 2018. doi:10.1001/jamapediatrics.2018.2853

4. Marshall KR, Holland SL, Meyer KS, Martin EM, Wilmore M, Grimes JB. Mild Traumatic Brain Injury Screening, Diagnosis, and Treatment. Mil Med. 2012; doi:10.7205/milmed-d-12-00110

5. Douglas DB, Ro T, Toffoli T, Krawchuk B, Muldermans J, Gullo J, et al. Neuroimaging of Traumatic Brain Injury. Med Sci. 2019;7. doi:10.3390/medsci7010002

6. Kim JJ, Gean AD. Imaging for the Diagnosis and Management of Traumatic Brain Injury. Neurotherapeutics. 2011; doi:10.1007/s13311-010-0003-3

7. Kou Z, Wu Z, Tong KA, Holshouser B, Benson RR, Hu J, et al. The role of advanced MR imaging findings as biomarkers of traumatic brain injury. Journal of Head Trauma Rehabilitation. 2010. doi:10.1097/HTR.0b013e3181e54793

8. Belanger HG, Vanderploeg RD, Curtiss G, Warden DL. Recent Neuroimaging Techniques in Mild Traumatic Brain Injury. J Neuropsychiatr. 2007; doi:10.1176/appi.neuropsych.19.1.5

9. Levin HS. Neuroplasticity following non-penetrating traumatic brain injury. Brain

Injury. 2003. doi:10.1080/0269905031000107151

10.   Levine B, Kovacevic N, Nica EI, Schwartz ML, Gao F, Black SE. Quantified MRI and cognition in TBI with diffuse and focal damage. NeuroImage Clin. 2013; doi:10.1016/j.nicl.2013.03.015

11.   Schranz AL, Manning KY, Dekaban GA, Fischer L, Jevremovic T, Blackney K, et al. Reduced brain glutamine in female varsity rugby athletes after concussion and in non-concussed athletes after a season of play. Hum Brain Mapp. John Wiley and Sons Inc.; 2018;39: 1489–1499. doi:10.1002/hbm.23919

12.   Xiong K lin, Zhu Y shan, Zhang W guo. Diffusion tensor imaging and magnetic resonance spectroscopy in traumatic brain injury: a review of recent literature. Brain Imaging Behav. 2014; doi:10.1007/s11682-013-9288-2

13.   Manning KY, Schranz A, Bartha R, Dekaban GA, Barreira C, Brown A, et al. Multiparametric MRI changes persist beyond recovery in concussed adolescent hockey players. Neurology. Lippincott Williams and Wilkins; 2017;89: 2157–2166. doi:10.1212/WNL.0000000000004669

14.   Kohl AD, Wylie GR, Genova HM, Hillary FG, DeLuca J. The neural correlates of cognitive fatigue in traumatic brain injury using functional MRI. Brain Inj. 2009; doi:10.1080/02699050902788519

15.   Eierud C, Craddock RC, Fletcher S, Aulakh M, King-Casas B, Kuehl D, et al. Neuroimaging after mild traumatic brain injury: Review and meta-analysis. NeuroImage Clin. Elsevier; 2014;4: 283–294. doi:10.1016/j.nicl.2013.12.009

16.   Lee B, Newberg A. Neuroimaging in traumatic brain imaging. NeuroRx. American Society for Experimental Neurotherapeutics; 2005;2: 372–383. doi:10.1602/neurorx.2.2.372

17.   Pierpaoli C, Jezzard P, Basser PJ, Barnett A, Di Chiro G. Diffusion tensor MR imaging of the human brain. Radiology. 1996;201: 637–648.

18. Sidaros A, Engberg AW, Sidaros K, Liptrot MG, Herning M, Petersen P, et al. Diffusion tensor imaging during recovery from severe traumatic brain injury and relation to clinical outcome: A longitudinal study. Brain. 2008; doi:10.1093/brain/awm294

19. Adamson C, Yuan W, Babcock L, Leach JL, Seal ML, Holland SK, et al. Diffusion tensor imaging detects white matter abnormalities and associated cognitive deficits in chronic adolescent TBI. Brain Inj. 2013; doi:10.3109/02699052.2012.750756

20. Faber J, Wilde EA, Hanten G, Ewing-Cobbs L, Aitken ME, Yallampalli R, et al. Ten-year outcome of early childhood traumatic brain injury: Diffusion tensor imaging of the ventral striatum in relation to executive functioning. Brain Inj. 2016; doi:10.1080/02699052.2016.1199910

21. Mac Donald CL, Dikranian K, Bayly P, Holtzman D, Brody D. Diffusion tensor imaging reliably detects experimental traumatic axonal injury and indicates approximate time of injury. J Neurosci. 2007; doi:10.1523/JNEUROSCI.3647-07.2007

22. Niogi SN, Mukherjee P. Diffusion tensor imaging of mild traumatic brain injury. Journal of Head Trauma Rehabilitation. 2010. doi:10.1097/HTR.0b013e3181e52c2a

23. Aoki Y, Inokuchi R, Gunshin M, Yahagi N, Suwa H. Diffusion tensor imaging studies of mild traumatic brain injury: A meta-analysis. J Neurol Neurosurg Psychiatry. 2012; doi:10.1136/jnnp-2012-302742

24. Khong E, Odenwald N, Hashim E, Cusimano MD. Diffusion tensor imaging findings in post-concussion syndrome patients after mild traumatic brain injury: A systematic review. Frontiers in Neurology. 2016. doi:10.3389/fneur.2016.00156

25. Lange RT, Iverson GL, Brubacher JR, Mädler B, Heran MK. Diffusion tensor imaging findings are not strongly associated with postconcussional disorder 2

months following mild traumatic brain injury. Journal of Head Trauma Rehabilitation. 2012. doi:10.1097/HTR.0b013e318217f0ad

26. Gardner A, Kay-Lambkin F, Stanwell P, Donnelly J, Williams WH, Hiles A, et al. A systematic review of diffusion tensor imaging findings in sports-related concussion. Journal of Neurotrauma. 2012. doi:10.1089/neu.2012.2628

27. Assaf Y, Basser P. Composite hindered and restricted model of diffusion (CHARMED) MR imaging of the human brain. Neuroimage. 2002;27: 48–58.

28. Fieremans E, Jensen JH, Helpern JA. White matter characterization with diffusional kurtosis imaging. Neuroimage. 2011; doi:10.1016/j.neuroimage.2011.06.006

29. Zhang H, Schneider T, Wheeler-Kingshott C, Alexander D. NODDI: practical in vivo neurite orientation dispersion and density imaging of the human brain. Neuroimage. 2012;61: 1000–1016.

30. Zhang H, Hubbard P, Parker G, Alexander D. Axon Diameter Mapping in the Presence of Orientation Dispersion with Diffusion MRI. Neuroimage. 2011;56: 1301–1315.

31. Champney T. Essential clinical neuroanatomy. 1st ed.

32. Vallejo R, Tilley DM, Vogel L, Benyamin R. The role of glia and the immune system in the development and maintenance of neuropathic pain. Pain Practice. 2010. doi:10.1111/j.1533-2500.2010.00367.x

33. Jessen KR. Glial cells. International Journal of Biochemistry and Cell Biology. 2004. doi:10.1016/j.biocel.2004.02.023

34. Barres BA. The Mystery and Magic of Glia: A Perspective on Their Roles in Health and Disease. Neuron. 2008. doi:10.1016/j.neuron.2008.10.013

35. Maurer LL, Aschner M, Philbert MA. Glial Cells. Comprehensive Toxicology:

Third Edition. 2018. doi:10.1016/B978-0-12-801238-3.65385-0

36.   DiSabato DJ, Quan N, Godbout JP. Neuroinflammation: the devil is in the details. J Neurochem. Blackwell Publishing Ltd; 2016;139: 136–153. doi:10.1111/jnc.13607

37.   Daneman R, Prat A. The blood–brain barrier. Cold Spring Harb Perspect Biol. 2015; doi:10.1101/cshperspect.a020412

38.   Abbott NJ, Patabendige AAK, Dolman DEM, Yusof SR, Begley DJ. Structure and function of the blood-brain barrier. Neurobiology of Disease. 2010. doi:10.1016/j.nbd.2009.07.030

39.   Keaney J, Campbell M. The dynamic blood-brain barrier. FEBS J. 2015; doi:10.1111/febs.13412

40.   Bigler ED. Neuroimaging biomarkers in mild traumatic brain injury (mTBI). Neuropsychology Review. 2013. doi:10.1007/s11065-013-9237-2

41.   Slobounov S, Gay M, Johnson B, Zhang K. Concussion in athletics: Ongoing clinical and brain imaging research controversies. Brain Imaging Behav. 2012; doi:10.1007/s11682-012-9167-2

42.   Faul M, Coronado V. Epidemiology of traumatic brain injury. Handbook of Clinical Neurology. 2015. doi:10.1016/B978-0-444-52892-6.00001-5

43.   Zaninotto ALC, Costa BT, Ferreira IS, French M, Paiva WS, Fregni F. Traumatic brain injury. Neuromethods. 2018. doi:10.1007/978-1-4939-7880-9_4

44.   Levin HS, Diaz-Arrastia RR. Diagnosis, prognosis, and clinical management of mild traumatic brain injury. The Lancet Neurology. 2015. doi:10.1016/S1474-4422(15)00002-2

45.   McKinlay A, John Horwood L, Fergusson DM. Accuracy of Self-report as a Method of Screening for Lifetime Occurrence of Traumatic Brain Injury Events

that Resulted in Hospitalization. J Int Neuropsychol Soc. Cambridge University Press; 2016;22: 717–723. doi:10.1017/S1355617716000497

46.   Sy KT, Spielman L, Wellington R, Dams-O'Connor K. One-year Test-Retest Reliability of Collegiate Athletes' Self-Report of Traumatic Brain Injury. Arch Phys Med Rehabil. 2016; doi:10.1016/j.apmr.2016.08.125

47.   Stoica BA, Faden AI. Cell Death Mechanisms and Modulation in Traumatic Brain Injury. Neurotherapeutics. 2010;7: 3–12. doi:10.1016/j.nurt.2009.10.023

48.   Johnson VE, Stewart W, Smith DH. Axonal pathology in traumatic brain injury. Experimental Neurology. 2013. pp. 35–43. doi:10.1016/j.expneurol.2012.01.013

49.   Armstrong RC, Mierzwa AJ, Marion CM, Sullivan GM. White matter involvement after TBI: Clues to axon and myelin repair capacity. Experimental Neurology. Academic Press Inc.; 2016. pp. 328–333. doi:10.1016/j.expneurol.2015.02.011

50.   Siedler DG, Chuah MI, Kirkcaldie MTK, Vickers JC, King AE. Diffuse axonal injury in brain trauma: Insights from alterations in neurofilaments. Frontiers in Cellular Neuroscience. 2014. doi:10.3389/fncel.2014.00429

51.   Meythaler JM, Peduzzi JD, Eleftheriou E, Novack TA. Current concepts: Diffuse axonal injury-associated traumatic brain injury. Arch Phys Med Rehabil. 2001; doi:10.1053/apmr.2001.25137

52.   Arfanakis K, Haughton VM, Carew JD, Rogers BP, Dempsey RJ, Meyerand ME. Diffusion tensor MR imaging in diffuse axonal injury. Am J Neuroradiol. 2002;

53.   Brooks DM, Patel SA, Wohlgehagen ED, Semmens EO, Pearce A, Sorich EA, et al. Multiple mild traumatic brain injury in the rat produces persistent pathological alterations in the brain. Exp Neurol. 2017; doi:10.1016/j.expneurol.2017.07.015

54.   Marshall TM, Henricks CL. The Next Generation in Brain Recovery and Neuroregeneration. Journal of American Physicians and Surgeons. 2017.

55.   Gao X, Chen J. Mild traumatic brain injury results in extensive neuronal degeneration in the cerebral cortex. J Neuropathol Exp Neurol. 2011; doi:10.1097/NEN.0b013e31820c6878

56.   Kilinc D, Gallo G, Barbee KA. Mechanical membrane injury induces axonal beading through localized activation of calpain. Exp Neurol. 2009;219: 553–561. doi:10.1016/j.expneurol.2009.07.014

57.   Kilinc D, Gallo G, Barbee K. Poloxamer 188 reduces axonal beading following mechanical trauma to cultured neurons. Annual International Conference of the IEEE Engineering in Medicine and Biology - Proceedings. 2007. doi:10.1109/IEMBS.2007.4353562

58.   Chiu CC, Liao YE, Yang LY, Wang JY, Tweedie D, Karnati HK, et al. Neuroinflammation in animal models of traumatic brain injury. Journal of Neuroscience Methods. 2016. doi:10.1016/j.jneumeth.2016.06.018

59.   Loane DJ, Kumar A. Microglia in the TBI brain: The good, the bad, and the dysregulated. Experimental Neurology. 2016. doi:10.1016/j.expneurol.2015.08.018

60.   Pekny M, Pekna M. Astrocyte reactivity and reactive astrogliosis: Costs and benefits. Physiol Rev. 2014; doi:10.1152/physrev.00041.2013

61.   Burda JE, Bernstein AM, Sofroniew M V. Astrocyte roles in traumatic brain injury. Experimental Neurology. Academic Press Inc.; 2016. pp. 305–315. doi:10.1016/j.expneurol.2015.03.020

62.   Bradl M, Lassmann H. Oligodendrocytes: Biology and pathology [Internet]. Acta Neuropathologica. 2010. pp. 37–53. doi:10.1007/s00401-009-0601-5

63.   Lotocki G, Vaccari J de R, Alonso O, Molano JS, Nixon R, Safavi P, et al. Oligodendrocyte vulnerability following traumatic brain injury in rats. Neuroscience Letters. 2011. pp. 143–148. doi:10.1016/j.neulet.2011.05.056

64. Dent KA, Christie KJ, Bye N, Basrai HS, Turbic A, Habgood M, et al. Oligodendrocyte birth and death following traumatic brain injury in adult mice. PLoS One. 2015; doi:10.1371/journal.pone.0121541

65. Flygt J, Gumucio A, Ingelsson M, Skoglund K, Holm J, Alafuzoff I, et al. Human traumatic brain injury results in oligodendrocyte death and increases the number of Oligodendrocyte progenitor cells. J Neuropathol Exp Neurol. 2016; doi:10.1093/jnen/nlw025

66. Johnson VE, Stewart JE, Begbie FD, Trojanowski JQ, Smith DH, Stewart W. Inflammation and white matter degeneration persist for years after a single traumatic brain injury. Brain. 2013; doi:10.1093/brain/aws322

67. Soares HD, Hicks RR, Smith D, McIntosh TK. Inflammatory leukocytic recruitment and diffuse neuronal degeneration are separate pathological processes resulting from traumatic brain injury. J Neurosci. 1995; doi:10.1523/jneurosci.15-12-08223.1995

68. Holmin S, Mathiesen T. Long-term intracerebral inflammatory response after experimental focal brain injury in rat. Neuroreport. 1999; doi:10.1097/00001756-199906230-00017

69. Das M, Mohapatra S, Mohapatra SS. New perspectives on central and peripheral immune responses to acute traumatic brain injury. Journal of Neuroinflammation. 2012. doi:10.1186/1742-2094-9-236

70. Prakash R, Carmichael ST. Blood-brain barrier breakdown and neovascularization processes after stroke and traumatic brain injury. Current Opinion in Neurology. 2015. doi:10.1097/WCO.0000000000000248

71. Szarka N, Toth L, Czigler A, Kellermayer Z, Ungvari Z, Amrein K, et al. Single mild traumatic brain injury induces persistent disruption of the blood-brain barrier, neuroinflammation and cognitive decline in hypertensive rats. Int J Mol Sci. 2019; doi:10.3390/ijms20133223

72. Lafrenaye AD, Todani M, Walker SA, Povlishock JT. Microglia processes associate with diffusely injured axons following mild traumatic brain injury in the micro pig. J Neuroinflammation. 2015; doi:10.1186/s12974-015-0405-6

73. Loane DJ, Kumar A. Microglia in the TBI brain: The good, the bad, and the dysregulated. Experimental Neurology. Academic Press Inc.; 2016. pp. 316–327. doi:10.1016/j.expneurol.2015.08.018

74. Haacke EM, Brown RW, Thompson MR, Venkatesan R. Haacke - Magnetic Resonance Imaging - Physical Principles and Sequence Design.pdf. Journal of Applied Physics. 1999. doi:10.1063/1.3554697

75. McRobbie DW, Moore EA, Graves MJ, Prince MR. MRI from picture to proton. MRI from Picture to Proton. 2006. doi:10.1017/CBO9780511545405

76. Griffiths DJ, Inglefield C. *Introduction to Electrodynamics*. Am J Phys. 2005; doi:10.1119/1.4766311

77. Lawrence RF. The Principles of Diffusion Tensor Imaging. Unpublished Work;

78. Bloch F. Nuclear induction. Phys Rev. 1946; doi:10.1103/PhysRev.70.460

79. Bloch F, Hansen WW, Packard M. The nuclear induction experiment. Phys Rev. 1946; doi:10.1103/PhysRev.70.474

80. Hahn EL. Spin echoes. Phys Rev. 1950; doi:10.1103/PhysRev.80.580

81. Elster AD. Gradient-echo MR imaging: Techniques and acronyms. Radiology. 1993. doi:10.1148/radiology.186.1.8416546

82. Brown R. XXVII. A brief account of microscopical observations made in the months of June, July and August 1827, on the particles contained in the pollen of plants; and on the general existence of active molecules in organic and inorganic bodies . Philos Mag. 2011; doi:10.1080/14786442808674769

83. Fick A. V. On liquid diffusion. London, Edinburgh, Dublin Philos Mag J Sci.

Taylor & Francis; 1855;10: 30–39. doi:10.1080/14786445508641925

84. Einstein A. Investigations on the Theory of Brownian Motion. Courier Corporation. 1956. doi:10.1002/andp.19053220806

85. Theoria motus corporum coelestium in sectionibus conicis solem ambientium - Carl Friedrich Gauss - Google Books [Internet]. [cited 11 Apr 2020]. Available: https://books.google.ca/books?hl=en&lr=&id=zXEyAQAAMAAJ&oi=fnd&pg=PA1&dq=Theoria+motus+corporum+coelestium+in+sectionibus+conicis+solem+ambientium&ots=vo8ea39uqi&sig=RMawrqc6NqvKgSJT6qAqwNkQD7w&redir_esc=y#v=onepage&q=Theoria motus corporum coelestium in sectionibus conicis solem ambientium&f=false

86. Perthes FA. Carolus Fridericus Gauss Theoria motus corporum coelestium in sectionibus conicis solem ambientium. Astron Nachrichten. 1855; doi:10.1002/asna.18550402508

87. Holz M, Heil SR, Sacco A. Temperature-dependent self-diffusion coefficients of water and six selected molecular liquids for calibration in accurate 1H NMR PFG measurements. Phys Chem Chem Phys. 2000; doi:10.1039/b005319h

88. Le Bihan D. Looking into the functional architecture of the brain with diffusion MRI. Nat Rev Neurosci. 2003; doi:10.1038/nrn1119

89. Beaulieu C. The basis of anisotropic water diffusion in the nervous system - A technical review. NMR in Biomedicine. 2002. doi:10.1002/nbm.782

90. Torrey HC. Bloch equations with diffusion terms. Phys Rev. 1956; doi:10.1103/PhysRev.104.563

91. Stejskal EO, Tanner JE. Spin diffusion measurements: Spin echoes in the presence of a time-dependent field gradient. J Chem Phys. 1965; doi:10.1063/1.1695690

92. Le Bihan D, Breton E, Lallemand D, Grenier P, Cabanis E, Laval-Jeantet M. MR imaging of intravoxel incoherent motions: application to diffusion and perfusion in

neurologic disorders. Radiology. 1986; doi:10.1148/radiology.161.2.3763909

93.   Liewald D, Miller R, Logothetis N, Wagner HJ, Schüz A. Distribution of axon diameters in cortical white matter: an electron-microscopic study on three human brains and a macaque. Biol Cybern. 2014; doi:10.1007/s00422-014-0626-2

94.   Barazany D, Basser PJ, Assaf Y. In vivo measurement of axon diameter distribution in the corpus callosum of rat brain. Brain. 2009; doi:10.1093/brain/awp042

95.   Shatarat A, Alzghoul L, Qattan D Al, Elbeltagy M. Anatomical and ultrastructural sex differences in mean diameter and thickness of myelinated axons in adult rat corpus callosum. Int J Morphol. 2020; doi:10.4067/S0717-95022020000200505

96.   Kandel ER, Schwartz JH, Jessell TM. Principles of Neural Science, fourth addition. McGraw-Hill Companies. 2000. doi:10.1036/0838577016

97.   Meitzen J, Pflepsen KR, Stern CM, Meisel RL, Mermelstein PG. Measurements of neuron soma size and density in rat dorsal striatum, nucleus accumbens core and nucleus accumbens shell: Differences between striatal region and brain hemisphere, but not sex. Neurosci Lett. 2011; doi:10.1016/j.neulet.2010.10.017

98.   Fiala JC, Harris KM. Dendrite structure.

99.   Hori M, Kamiya K, Nakanishi A, Fukunaga I, Miyajima M, Nakajima M, et al. Prospective estimation of mean axon diameter and extra-axonal space of the posterior limb of the internal capsule in patients with idiopathic normal pressure hydrocephalus before and after a lumboperitoneal shunt by using q-space diffusion MRI. Eur Radiol. 2016; doi:10.1007/s00330-015-4162-9

100. Le Bihan D, Mangin JF, Poupon C, Clark CA, Pappata S, Molko N, et al. Diffusion tensor imaging: Concepts and applications. J Magn Reson Imaging. 2001; doi:10.1002/jmri.1076

101. Moseley ME, Cohen Y, Kucharczyk J, Mintorovitch J, Asgari HS, Wendland MF,

et al. Diffusion-weighted MR imaging of anisotropic water diffusion in cat central nervous system. Radiology. 1990;176: 439–445. doi:10.1148/radiology.176.2.2367658

102. Basser PJ, Mattiello J, Lebihans D. MR Diffusion Tensor Spectroscopy and Imaging. Biophys J. 1994;66: 259–267.

103. Gardner A, Kay-Lambkin F, Stanwell P, Donnelly J, Williams WH, Hiles A, et al. A Systematic Review of Diffusion Tensor Imaging Findings in Sports-Related Concussion. J Neurotrauma. 2012; doi:10.1089/neu.2012.2628

104. Shenton ME, Hamoda HM, Schneiderman JS, Bouix S, Pasternak O, Rathi Y, et al. A review of magnetic resonance imaging and diffusion tensor imaging findings in mild traumatic brain injury. Brain Imaging Behav. 2012; doi:10.1007/s11682-012-9156-5

105. Oishi K, Mielke MM, Albert M, Lyketsos CG, Mori S. DTI analyses and clinical applications in Alzheimer's disease. Adv Alzheimer's Dis. 2011; doi:10.3233/978-1-60750-793-2-525

106. Nortje G, Stein DJ, Radua J, Mataix-Cols D, Horn N. Systematic review and voxel-based meta-analysis of diffusion tensor imaging studies in bipolar disorder. Journal of Affective Disorders. 2013. doi:10.1016/j.jad.2013.05.034

107. Waller R, Dotterer HL, Murray L, Maxwell AM, Hyde LW. White-matter tract abnormalities and antisocial behavior: A systematic review of diffusion tensor imaging studies across development. NeuroImage: Clinical. 2017. doi:10.1016/j.nicl.2017.01.014

108. Scott AD, Ferreira PFADC, Nielles-Vallespin S, Gatehouse P, McGill L-A, Kilner P, et al. Optimal diffusion weighting for in vivo cardiac diffusion tensor imaging. Magn Reson Med. 2015;74: 420–430.

109. Timmers I, Roebroeck A, Bastiani M, Jansma B, Rubio-Gozalbo E, Zhang H. Assessing Microstructural Substrates of White Matter Abnormalities: A

Comparative Study Using DTI and NODDI. PLoS One. 2016;11.

110. Szafer A, Zhong J, Anderson AW, Gore JC. Diffusion-weighted imaging in tissues: Theoretical models. NMR Biomed. 1995; doi:10.1002/nbm.1940080704

111. Burdette JH, Durden DD, Elster AD, Yen YF. High b-value diffusion-weighted MRI of normal brain. J Comput Assist Tomogr. 2001; doi:10.1097/00004728-200107000-00002

112. Cohen Y, Assaf Y. High b-value q-space analyzed diffusion-weighted MRS and MRI in neuronal tissues - A technical review. NMR in Biomedicine. 2002. doi:10.1002/nbm.778

113. Yoshiura T, Mihara F, Tanaka A, Ogomori K, Ohyagi Y, Taniwaki T, et al. High b value diffusion-weighted imaging is more sensitive to white matter degeneration in Alzheimer's disease. Neuroimage. 2003; doi:10.1016/S1053-8119(03)00342-2

114. Peckham ME, Anderson JS, Rassner UA, Shah LM, Hinckley PJ, de Havenon A, et al. Low b-value diffusion weighted imaging is promising in the diagnosis of brain death and hypoxic-ischemic injury secondary to cardiopulmonary arrest. Crit Care. 2018; doi:10.1186/s13054-018-2087-9

115. Rathi Y, Michailovich O, Setsompop K, Bouix S, Shenton ME, Westin CF. Sparse multi-shell diffusion imaging. Lecture Notes in Computer Science (including subseries Lecture Notes in Artificial Intelligence and Lecture Notes in Bioinformatics). 2011. doi:10.1007/978-3-642-23629-7_8

116. Pines AR, Cieslak M, Baum GL, Cook PA, Adebimpe A, Dávila DG, et al. Advantages of Multi-shell Diffusion for Studies of Brain Development in Youth. bioRxiv. 2019; doi:10.1101/611590

117. Webster JG, Descoteaux M. High Angular Resolution Diffusion Imaging (HARDI). Wiley Encyclopedia of Electrical and Electronics Engineering. 2015. doi:10.1002/047134608x.w8258

118. Churchill NW, Caverzasi E, Graham SJ, Hutchison MG, Schweizer TA. White matter microstructure in athletes with a history of concussion: Comparing diffusion tensor imaging (DTI) and neurite orientation dispersion and density imaging (NODDI). Hum Brain Mapp. 2017;38: 4201–4211. doi:10.1002/hbm.23658

119. Churchill NW, Caverzasi E, Graham SJ, Hutchison MG, Schweizer TA. White matter during concussion recovery: Comparing diffusion tensor imaging (DTI) and neurite orientation dispersion and density imaging (NODDI). Hum Brain Mapp. John Wiley and Sons Inc.; 2019;40: 1908–1918. doi:10.1002/hbm.24500

120. Wu YC, Mustafi SM, Harezlak J, Kodiweera C, Flashman LA, McAllister TW. Hybrid Diffusion Imaging in Mild Traumatic Brain Injury. J Neurotrauma. Mary Ann Liebert Inc.; 2018;35: 2377–2390. doi:10.1089/neu.2017.5566

121. Emes RD, Goodstadt L, Winter EE, Ponting CP. Comparison of the genomes of human and mouse lays the foundation of genome zoology. Hum Mol Genet. Narnia; 2003;12: 701–709. doi:10.1093/hmg/ddg078

122. Lythgoe MF, Sibson NR, Harris NG. Neuroimaging of animal models of brain disease. Br Med Bull. 2003;65: 235–257. doi:10.1093/bmb/65.1.235

123. Denic A, Macura SI, Mishra P, Gamez JD, Rodriguez M, Pirko I. MRI in Rodent Models of Brain Disorders. Neurotherapeutics. 2011;8: 3–18. doi:10.1007/s13311-010-0002-4

124. Hoyer C, Gass N, Weber-Fahr W, Sartorius A. Advantages and challenges of small animal magnetic resonance imaging as a translational tool. Neuropsychobiology. Karger Publishers; 2014;69: 187–201. doi:10.1159/000360859

125. Alexander AL, Lee JE, Lazar M, Field AS. Diffusion tensor imaging of the brain. Neurotherapeutics. 2007;4: 316–329.

126. Qiu D, Tan L, Zhou K, Khong P. Diffusion tensor imaging of normal white matter maturation from late childhood to young adulthood: voxel-wise evaluation of mean

diffusivity, fractional anisotropy. Neuroimage. 2008;41: 223–232.

127. Kumar R, Nguyen HD, Macey PM, Woo MA, Harper RM. Regional brain axial and radial diffusivity changes during development. J Neurosci Res. 2012;90: 346–355.

128. Wheeler-Kingshott CAM, Cercignani M. About "axial" and "radial" diffusivities. Magn Reson Med. 2009;61: 1255–1260.

129. Özkan M, Marterer R, Tscheuner S, Yildirim U, Ozkan E. The role of kidney diffusion tensor magnetic resonance imaging in children. Egypt J Radiol Nucl Med. 2016;47: 1599–1611.

130. Kodiweera C, Alexander A, Harezlak J, McAllister T, Wu Y-C. Age effects and sex differences in human brain white matter of young to middle-aged adults: a DTI, NODDI, and q-space study. Neuroimage. 2016;128: 180–192.

131. Tuch DS. Q-ball imaging. Magn Reson Med. 2004;52: 1358–1372.

132. Wu EX, Cheung MM. MR diffusion kurtosis imaging for neural tissue characterization. NMR Biomed. 2010;23: 836–848.

133. Wu D, Martin LJ, Northington FJ, Zhang J. Oscillating gradient diffusion MRI reveals unique microstructural information in normal and hypoxia-ischemia injured mouse brains. Magn Reson Med. 2014;72: 1366–1374.

134. Schneider T, Brownlee W, Zhang H, Ciccarelli O, Miller DH, Wheeler-Kingshott CG. Sensitivity of multi-shell NODDI to multiple sclerosis white matter changes: a pilot study. Funct Neurol. 32: 97–101.

135. By S, Xu J, Box B, Bagnato F, Smith S. Application and evaluation of NODDI in the cervical spinal cord of multiple sclerosis patients. NeuroImage Clin. 2017;15: 333–342.

136. Caverzasi E, Papinutto N, Castellano A, Zhu AH, Scifo P, Riva M, et al. Neurite

Orientation Dispersion and Density Imaging Color Maps to Characterize Brain Diffusion in Neurologic Disorders. J Neuroimaging. 2016;26: 494–498.

137. Deligianni F, Carmichael DW, Zhang GH, Clark CA, Clayden JD. NODDI and Tensor-Based Microstructural Indices as Predictors of Functional Connectivity. PLoS One. 2016;11.

138. Kamagata K, Hatano T, Aoki S. What is NODDI and what is its role in Parkinson's assessment? Expert Rev Neurother. 2016;16: 241–243.

139. Mah A, Geeraert B, Lebel C. Detailing neuroanatomical development in late childhood and early adolescence using NODDI. PLoS One. 2017;12. doi:10.1371/journal.pone.0182340

140. Slattery C, Zhang J, Paterson R, Foulkes A, Mancini L, Thomas D, et al. Neurite orientation dispersion and density imaging (NODDI) in young onset Alzheimer's disease and its syndromic variants. Alzheimers Dement. 2015;11.

141. Wen Q, Kelley D, Banerjee S, Lupo J, Chang S, Xu D, et al. Clinically feasible NODDI characterization of glioma using multiband EPI at 7 T. NeuroImage Clin. 2015;9: 291–299.

142. Chung AW, Seunarine KK, Clark CA. NODDI reproducibility and variability with magnetic field strength: A comparison between 1.5 T and 3 T. Hum Brain Mapp. 2016;37: 4550–4565.

143. Alomair OI, Brereton IM, Smith MT, Galloway GJ, Kurniawan ND. In vivo high angular resolution diffusion-weighted imaging of mouse brain at 16.4 Tesla. PLoS One. 2015;10.

144. Colgan N, Siow B, O'Callaghan J, Harrison I. Application of neurite orientation dispersion and density imaging (NODDI) to a tau pathology model of Alzheimer's disease. Neuroimage. 2016;125: 759–744.

145. Gilbert K, Gati J, Klassen L, Zeman, P, Schaeffer D, Everling S, et al. A

geometrically adjustable receive array for imaging marmoset cohorts. Neuroimage. 2017;156: 78–86.

146. Caruyer E, Lenglet C, Sapiro G, Deriche R. Design of multishell sampling schemes with uniform coverage in diffusion MRI. Magn Reson Med. 2013;69: 1534–1540. doi:10.1002/mrm.24736

147. Frahm J, Haase A, Matthaei D. Rapid three-dimensional MR imaging using the FLASH technique. J Comput Assist Tomogr. 1986;10: 363–368.

148. Andersson JLR, Skare S, Ashburner J. How to correct susceptibility distortions in spin-echo echo-planar images: application to diffusion tensor imaging. Neuroimage. 2003;20: 870–888. doi:10.1016/S1053-8119(03)00336-7

149. Andersson J, Sotiropoulos S. An integrated approach to correction for off-resonance effects and subject movement in diffusion MR imaging. Neuroimage. 2016;125: 1063–1078.

150. Chou N, Wu J, Bingren J, Qiu A. Robust automatic rodent brain extraction using 3-D pulse-coupled neural networks (PCNN). IEEE Trans Image Process. 2011;20: 2554–2564.

151. Jenkinson M, Bannister P, Brady M, Smith S. Improved optimization for the robust and accurate linear registration and motion correction of brain images. Neuroimage. 2002;17: 825–841.

152. Eszter P, Lisa K, Sveinung L, Johnson G, Menno W, Trygve L, et al. Volumetric Waxholm Space atlas of the rat brain for spatial integration of experimental image data. Front Neuroinform. 2013;7.

153. Andersson JLR, Jenkinson M SS. Non-linear registration, aka spatial normalisation. 2010.

154. van Belle G. Sample Size. Statistical Rules of Thumb. 2nd ed. Hoboken: John Wiley & Sons; 2018. pp. 27–51. doi:10.4135/9781412985451.n7

155. Bauman S, Ray M, Joseph PP. Gender differences in clinical presentation and recovery of sports related concussion. Br J Sports Med. BMJ; 2017;51: A35.2-A35. doi:10.1136/bjsports-2016-097270.89

156. Choe MC, Giza CC. Diagnosis and management of acute concussion. Semin Neurol. 2015; doi:10.1055/s-0035-1544243

157. King NS, Kirwilliam S. Permanent post-concussion symptoms after mild head injury. Brain Inj. 2011;25: 462–470. doi:10.3109/02699052.2011.558042

158. Bloom GA, Caron JG. Psychological Aspects of Sport-Related Concussions. Psychological Aspects of Sport-Related Concussions. Routledge; 2019. doi:10.4324/9781351200516

159. Patel A, Vieira MMC, Abraham J, Reid N, Tran T, Tomecsek K, et al. Quality of the development of traumatic brain injury clinical practice guidelines: A systematic review. PLoS One. Public Library of Science; 2016;11. doi:10.1371/journal.pone.0161554

160. Bulger EM, Nathens AB, Rivara FP, Moore M, MacKenzie EJ, Jurkovich GJ. Management of severe head injury: Institutional variations in care and effect on outcome. Crit Care Med. 2002; doi:10.1097/00003246-200208000-00033

161. Gupta D, Sharma D, Kannan N, Prapruettham S, Mock C, Wang J, et al. Guideline Adherence and Outcomes in Severe Adult Traumatic Brain Injury for the CHIRAG (Collaborative Head Injury and Guidelines) Study. World Neurosurg. 2016; doi:10.1016/j.wneu.2015.12.097

162. Moppett IK. Traumatic brain injury: Assessment, resuscitation and early management. British Journal of Anaesthesia. 2007. doi:10.1093/bja/aem128

163. Povlishock JT. The window of risk in repeated head injury. Journal of Neurotrauma. 1 Jan 201330: 1. doi:10.1089/neu.2013.9942

164. Kroshus E, Baugh CM, Daneshvar DH, Viswanath K. Understanding concussion

reporting using a model based on the theory of planned behavior. J Adolesc Heal. Elsevier USA; 2014;54. doi:10.1016/j.jadohealth.2013.11.011

165. Kroshus E, Garnett B, Hawrilenko M, Baugh CM, Calzo JP. Concussion under-reporting and pressure from coaches, teammates, fans, and parents. Soc Sci Med. Elsevier Ltd; 2015;134: 66–75. doi:10.1016/j.socscimed.2015.04.011

166. Xiong Y, Mahmood A, Chopp M. Current understanding of neuroinflammation after traumatic brain injury and cell-based therapeutic opportunities. Chinese Journal of Traumatology - English Edition. 2018. doi:10.1016/j.cjtee.2018.02.003

167. Mckee AC, Daneshvar DH. The neuropathology of traumatic brain injury. Handbook of Clinical Neurology. 2015. doi:10.1016/B978-0-444-52892-6.00004-0

168. Blennow K, Hardy J, Zetterberg H. The Neuropathology and Neurobiology of Traumatic Brain Injury. Neuron. 2012. doi:10.1016/j.neuron.2012.11.021

169. Bigler ED, Maxwell WL. Neuropathology of mild traumatic brain injury: Relationship to neuroimaging findings. Brain Imaging Behav. 2012; doi:10.1007/s11682-011-9145-0

170. Dastgheyb RM. MECHANISMS OF AXONAL PATHOLOGY IN THE CONTEXT OF TRAUMATIC BRAIN INJURY. 2014.

171. Hill CS, Coleman MP, Menon DK. Traumatic Axonal Injury: Mechanisms and Translational Opportunities. Trends in Neurosciences. Elsevier Ltd; 2016. pp. 311–324. doi:10.1016/j.tins.2016.03.002

172. Schimmel S, Acosta S, Lozano D. Neuroinflammation in traumatic brain injury: A chronic response to an acute injury. Brain Circ. Medknow; 2017;3: 135. doi:10.4103/bc.bc_18_17

173. Wofford KL, Loane DJ, Cullen DK. Acute drivers of neuroinflammation in traumatic brain injury. Neural Regeneration Research. Wolters Kluwer Medknow

Publications; 2019. pp. 1481–1489. doi:10.4103/1673-5374.255958

174. Hutchinson EB, Schwerin SC, Avram A V., Juliano SL, Pierpaoli C. Diffusion MRI and the detection of alterations following traumatic brain injury. Journal of Neuroscience Research. 2018. doi:10.1002/jnr.24065

175. Churchill NW, Caverzasi E, Graham SJ, Hutchison MG, Schweizer TA. White matter during concussion recovery: Comparing diffusion tensor imaging (DTI) and neurite orientation dispersion and density imaging (NODDI). Hum Brain Mapp. John Wiley & Sons, Ltd; 2019;40: 1908–1918. doi:10.1002/hbm.24500

176. Hoogenboom WS, Rubin TG, Ye K, Cui MH, Branch KC, Liu J, et al. Diffusion Tensor Imaging of the Evolving Response to Mild Traumatic Brain Injury in Rats. J Exp Neurosci. 2019; doi:10.1177/1179069519858627

177. Girgis F, Pace J, Sweet J, Miller JP. Hippocampal neurophysiologic changes after mild traumatic brain injury and potential neuromodulation treatment approaches. Frontiers in Systems Neuroscience. 2016. doi:10.3389/fnsys.2016.00008

178. Bigler ED, Blatter DD, Gale SD, Ryser DK, Macnamara SE, Bailey BJ, et al. Traumatic brain injury and memory: The role of hippocampal atrophy. Neuropsychology. 1996; doi:10.1037/0894-4105.10.3.333

179. Alder J, Fujioka W, Lifshitz J, Crockett DP, Thakker-Varia S. Lateral Fluid Percussion: Model of Traumatic Brain Injury in Mice. J Vis Exp. 2011; doi:10.3791/3063

180. Dixon CE, Lyeth BG, Povlishock JT, Findling RL, Hamm RJ, Marmarou A, et al. A fluid percussion model of experimental brain injury in the rat. J Neurosurg. 1987; doi:10.3171/jns.1987.67.1.0110

181. Cheng WH, Martens KM, Carr M, Wilkinson A, Fan J, Robert J, et al. Merging pathology with biomechanics using CHIMERA (Closed-Head Impact Model of Engineered Rotational Acceleration): a novel, surgery-free model of traumatic brain injury. Mol Neurodegener. 2014;

182. Rubovitch V, Ten-Bosch M, Zohar O, Harrison CR, Tempel-Brami C, Stein E, et al. A mouse model of blast-induced mild traumatic brain injury. Exp Neurol. 2011; doi:10.1016/j.expneurol.2011.09.018

183. Budde MD, Shah A, McCrea M, Cullinan WE, Pintar FA, Stemper BD. Primary Blast Traumatic Brain Injury in the Rat: Relating Diffusion Tensor Imaging and Behavior. Front Neurol. 2013; doi:10.3389/fneur.2013.00154

184. Cheng J, Gu J, Ma Y, Yang T, Kuang Y, Li B, et al. Development of a rat model for studying blast-induced traumatic brain injury. J Neurol Sci. 2010; doi:10.1016/j.jns.2010.04.010

185. Romine J, Gao X, Chen J. Controlled cortical impact model for traumatic brain injury. J Vis Exp. 2014; doi:10.3791/51781

186. Osier ND, Korpon JR, Dixon CE. Controlled cortical impact model. Brain Neurotrauma: Molecular, Neuropsychological, and Rehabilitation Aspects. 2015. doi:10.1201/b18126

187. Lighthall JW. Controlled Cortical Impact: A New Experimental Brain Injury Model. J Neurotrauma. 1988; doi:10.1089/neu.1988.5.1

188. Edward Dixon C, Clifton GL, Lighthall JW, Yaghmai AA, Hayes RL. A controlled cortical impact model of traumatic brain injury in the rat. J Neurosci Methods. 1991; doi:10.1016/0165-0270(91)90104-8

189. Washington PM, Forcelli PA, Wilkins T, Zapple DN, Parsadanian M, Burns MP. The effect of injury severity on behavior: A phenotypic study of cognitive and emotional deficits after mild, moderate, and severe controlled cortical impact injury in mice. J Neurotrauma. 2012; doi:10.1089/neu.2012.2456

190. Saatman KE, Feeko KJ, Pape RL, Raghupathi R. Differential behavioral and histopathological responses to graded cortical impact injury in mice. J Neurotrauma. 2006; doi:10.1089/neu.2006.23.1241

191. Mao H, Jin X, Zhang L, Yang KH, Igarashi T, Noble-Haeusslein LJ, et al. Finite element analysis of controlled cortical impact-induced cell loss. J Neurotrauma. 2010; doi:10.1089/neu.2008.0616

192. Igarashi T, Potts MB, Noble-Haeusslein LJ. Injury severity determines Purkinje cell loss and microglial activation in the cerebellum after cortical contusion injury. Exp Neurol. 2007; doi:10.1016/j.expneurol.2006.08.030

193. Osier N, Dixon CE. Mini review of controlled cortical impact: A well-suited device for concussion research. Brain Sciences. 2017. doi:10.3390/brainsci7070088

194. Osier ND, Dixon CE. The controlled cortical impact model: Applications, considerations for researchers, and future directions. Frontiers in Neurology. 2016. doi:10.3389/fneur.2016.00134

195. Shitaka Y, Tran HT, Bennett RE, Sanchez L, Levy MA, Dikranian K, et al. Repetitive closed-skull traumatic brain injury in mice causes persistent multifocal axonal injury and microglial reactivity. J Neuropathol Exp Neurol. 2011; doi:10.1097/NEN.0b013e31821f891f

196. Jamnia N, Urban JH, Stutzmann GE, Chiren SG, Reisenbigler E, Marr R, et al. A Clinically Relevant Closed-Head Model of Single and Repeat Concussive Injury in the Adult Rat Using a Controlled Cortical Impact Device. J Neurotrauma. 2017; doi:10.1089/neu.2016.4517

197. K. M, E. G. A preclinical model of heterogeneity in closed head mTBI. J Neurotrauma. 2018; doi:http://dx.doi.org/10.1089/neu.2018.29013.abstracts

198. Petraglia AL, Plog BA, Dayawansa S, Chen M, Dashnaw ML, Czerniecka K, et al. The spectrum of neurobehavioral sequelae after repetitive mild traumatic brain injury: A novel mouse model of chronic traumatic encephalopathy. J Neurotrauma. 2014; doi:10.1089/neu.2013.3255

199. Hennig J, Nauerth A, Friedburg H. RARE imaging: A fast imaging method for

clinical MR. Magn Reson Med. 1986; doi:10.1002/mrm.1910030602

200. McCunn P, Gilbert KM, Zeman P, Li AX, Strong MJ, Khan AR, et al. Reproducibility of Neurite Orientation Dispersion and Density Imaging (NODDI) in rats at 9.4 Tesla. PLoS One. 2019; doi:10.1371/journal.pone.0215974

201. IBM SPSS Statistics for Mac Version 26 (IBM Corp., Armonk, N.Y. USA).

202. Sato M, Chang E, Igarashi T, Noble LJ. Neuronal injury and loss after traumatic brain injury: Time course and regional variability. Brain Res. 2001; doi:10.1016/S0006-8993(01)02905-5

203. Stone JR, Okonkwo DO, Dialo AO, Rubin DG, Mutlu LK, Povlishock JT, et al. Impaired axonal transport and altered axolemmal permeability occur in distinct populations of damaged axons following traumatic brain injury. Exp Neurol. Academic Press; 2004;190: 59–69. doi:10.1016/j.expneurol.2004.05.022

204. Pierce JES, Trojanowski JQ, Graham DI, Smith DH, McIntosh TK. Immunohistochemical characterization of alterations in the distribution of amyloid precursor proteins and β-amyloid peptide after experimental brain injury in the rat. J Neurosci. Society for Neuroscience; 1996;16: 1083–1090. doi:10.1523/jneurosci.16-03-01083.1996

205. Hemphill MA, Dauth S, Yu CJ, Dabiri BE, Parker KK. Traumatic brain injury and the neuronal microenvironment: A potential role for neuropathological mechanotransduction. Neuron. 2015. doi:10.1016/j.neuron.2015.02.041

206. Schwab N, Grenier K, Hazrati LN. DNA repair deficiency and senescence in concussed professional athletes involved in contact sports. Acta Neuropathol Commun. 2019; doi:10.1186/s40478-019-0822-3

207. O'Keeffe E, Kelly E, Liu Y, Giordano C, Wallace E, Hynes M, et al. Dynamic Blood–Brain Barrier Regulation in Mild Traumatic Brain Injury. J Neurotrauma. Mary Ann Liebert Inc.; 2020;37: 347–356. doi:10.1089/neu.2019.6483

208. Hay JR, Johnson VE, Young AMH, Smith DH, Stewart W. Blood-brain barrier disruption is an early event that may persist for many years after traumatic brain injury in humans. J Neuropathol Exp Neurol. 2015; doi:10.1097/NEN.0000000000000261

209. Chodobski A, Zink BJ, Szmydynger-Chodobska J. Blood-Brain Barrier Pathophysiology in Traumatic Brain Injury. Translational Stroke Research. 2011. doi:10.1007/s12975-011-0125-x

210. Marchi N, Bazarian JJ, Puvenna V, Janigro M, Ghosh C, Zhong J, et al. Consequences of Repeated Blood-Brain Barrier Disruption in Football Players. PLoS One. 2013; doi:10.1371/journal.pone.0056805

211. Sahyouni R, Gutierrez P, Gold E, Robertson RT, Cummings BJ. Effects of concussion on the blood–brain barrier in humans and rodents. J Concussion. 2017; doi:10.1177/2059700216684518

212. Alves JL. Blood-brain barrier and traumatic brain injury. Journal of Neuroscience Research. 2014. doi:10.1002/jnr.23300

213. Herculano-Houzel S. The glia/neuron ratio: How it varies uniformly across brain structures and species and what that means for brain physiology and evolution. GLIA. 2014. doi:10.1002/glia.22683

214. Kreutzberg GW. Microglia: A sensor for pathological events in the CNS. Trends in Neurosciences. 1996. doi:10.1016/0166-2236(96)10049-7

215. Burda JE, Sofroniew M V. Reactive gliosis and the multicellular response to CNS damage and disease. Neuron. 2014. doi:10.1016/j.neuron.2013.12.034

216. Corps KN, Roth TL, McGavern DB. Inflammation and neuroprotection in traumatic brain injury. JAMA Neurol. 2015; doi:10.1001/jamaneurol.2014.3558

217. Nimmerjahn A, Kirchhoff F, Helmchen F. Neuroscience: Resting microglial cells are highly dynamic surveillants of brain parenchyma in vivo. Science (80-). 2005;

doi:10.1126/science.1110647

218. Davalos D, Grutzendler J, Yang G, Kim J V., Zuo Y, Jung S, et al. ATP mediates rapid microglial response to local brain injury in vivo. Nat Neurosci. 2005; doi:10.1038/nn1472

219. Roth TL, Nayak D, Atanasijevic T, Koretsky AP, Latour LL, McGavern DB. Transcranial amelioration of inflammation and cell death after brain injury. Nature. 2014; doi:10.1038/nature12808

220. Taib T, Leconte C, Van Steenwinckel J, Cho AH, Palmier B, Torsello E, et al. Neuroinflammation, myelin and behavior: Temporal patterns following mild traumatic brain injury in mice. PLoS One. 2017; doi:10.1371/journal.pone.0184811

221. Jassam YN, Izzy S, Whalen M, McGavern DB, El Khoury J. Neuroimmunology of Traumatic Brain Injury: Time for a Paradigm Shift. Neuron. 2017. doi:10.1016/j.neuron.2017.07.010

222. Yi SY, Barnett BR, Torres-Velázquez M, Zhang Y, Hurley SA, Rowley PA, et al. Detecting microglial density with quantitative multi-compartment diffusion MRI. Front Neurosci. Frontiers Media S.A.; 2019;13. doi:10.3389/fnins.2019.00081

223. Jurick SM, Bangen KJ, Evangelista ND, Sanderson-Cimino M, Delano-Wood L, Jak AJ. Advanced neuroimaging to quantify myelin in vivo: Application to mild TBI. Brain Injury. Taylor and Francis Ltd; 2016. pp. 1452–1457. doi:10.1080/02699052.2016.1219064

224. Asken BM, DeKosky ST, Clugston JR, Jaffee MS, Bauer RM. Diffusion tensor imaging (DTI) findings in adult civilian, military, and sport-related mild traumatic brain injury (mTBI): a systematic critical review. Brain Imaging and Behavior. Springer New York LLC; 2018. pp. 585–612. doi:10.1007/s11682-017-9708-9

225. Mayer AR, Ling JM, Dodd AB, Meier TB, Hanlon FM, Klimaj SD. A prospective microstructure imaging study in mixed-martial artists using geometric measures

and diffusion tensor imaging: methods and findings. doi:10.1007/s11682-016-9546-1

226. Churchill NW, Caverzasi E, Graham SJ, Hutchison MG, Schweizer TA. White matter microstructure in athletes with a history of concussion: Comparing diffusion tensor imaging (DTI) and neurite orientation dispersion and density imaging (NODDI). Hum Brain Mapp. John Wiley and Sons Inc.; 2017;38: 4201–4211. doi:10.1002/hbm.23658

227. Taha AA, Hanbury A. Metrics for evaluating 3D medical image segmentation: Analysis, selection, and tool. BMC Med Imaging. BioMed Central Ltd.; 2015;15. doi:10.1186/s12880-015-0068-x

228. Friese MB, Nathan M, Culley DJ, Crosby G. Isoflurane anesthesia impairs the expression of immune neuromodulators in the hippocampus of aged mice. PLoS One. 2018; doi:10.1371/journal.pone.0209283

229. Blum FE, Zuo Z. Volatile anesthetics-induced neuroinflammatory and anti-inflammatory responses. Med Gas Res. 2013; doi:10.1186/2045-9912-3-16

230. Tétrault S, Chever O, Sik A, Amzica F. Opening of the blood-brain barrier during isoflurane anaesthesia. Eur J Neurosci. 2008; doi:10.1111/j.1460-9568.2008.06443.x

231. Chi OZ, Mellender SJ, Kiss GK, Liu X, Weiss HR. Blood -brain barrier disruption was less under isoflurane than pentobarbital anesthesia via a PI3K/Akt pathway in early cerebral ischemia. Brain Res Bull. Elsevier Inc.; 2017;131: 1–6. doi:10.1016/j.brainresbull.2017.02.007

232. Oak Za Chi, Anwar M, Sinha AK, Hwu Meei Wei, Klein SL, Weiss HR. Effects of isoflurane on transport across the blood-brain barrier. Anesthesiology. 1992. pp. 426–431. doi:10.1097/00000542-199203000-00016

233. Dixon KJ. Pathophysiology of Traumatic Brain Injury. Physical Medicine and Rehabilitation Clinics of North America. 2017. doi:10.1016/j.pmr.2016.12.001

234. McKee AC, Cantu RC, Nowinski CJ, Hedley-Whyte ET, Gavett BE, Budson AE, et al. Chronic traumatic encephalopathy in athletes: Progressive tauopathy after repetitive head injury. Journal of Neuropathology and Experimental Neurology. 2009. doi:10.1097/NEN.0b013e3181a9d503

235. Stern RA, Riley DO, Daneshvar DH, Nowinski CJ, Cantu RC, McKee AC. Long-term Consequences of Repetitive Brain Trauma: Chronic Traumatic Encephalopathy. PM and R. 2011. doi:10.1016/j.pmrj.2011.08.008

236. Sports-Related Concussions in Youth: Improving the Science, Changing the Culture. Mil Med. 2015; doi:10.7205/milmed-d-14-00516

237. Prigatano GP, Gale SD. The current status of postconcussion syndrome. Curr Opin Psychiatry. 2011; doi:10.1097/YCO.0b013e328344698b

238. Ojo JO, Mouzon BC, Crawford F. Repetitive head trauma, chronic traumatic encephalopathy and tau: Challenges in translating from mice to men. Experimental Neurology. 2016. doi:10.1016/j.expneurol.2015.06.003

239. Bailes JE, Dashnaw ML, Petraglia AL, Turner RC. Cumulative effects of repetitive mild traumatic brain injury. Concussion. 2012. doi:10.1159/000358765

240. McLendon LA, Kralik SF, Grayson PA, Golomb MR. The Controversial Second Impact Syndrome: A Review of the Literature. Pediatric Neurology. 2016. doi:10.1016/j.pediatrneurol.2016.03.009

241. Williams N, Sas A, Madey J, Bodle J, Scovel L, Edwards J. High school coaches perceptions of physicians' role in the assessment and management of sports-related concussive injury. Front Neurol. 2012; doi:10.3389/fneur.2012.00130

242. Coxe K, Hamilton K, Harvey HH, Xiang J, Ramirez MR, Yang J. Consistency and Variation in School-Level Youth Sports Traumatic Brain Injury Policy Content. J Adolesc Heal. 2018; doi:10.1016/j.jadohealth.2017.07.003

243. Yuh EL, Cooper SR, Mukherjee P, Yue JK, Lingsma HF, Gordon WA, et al.

Diffusion tensor imaging for outcome prediction in mild traumatic brain injury: a TRACK-TBI study. J Neurotrauma. 2014; doi:10.1089/neu.2013.3171

244.   Sharp DJ, Ham TE. Investigating white matter injury after mild traumatic brain injury. Current Opinion in Neurology. 2011. doi:10.1097/WCO.0b013e32834cd523

245.   D'Souza MM, Trivedi R, Singh K, Grover H, Choudhury A, Kaur P, et al. Traumatic brain injury and the post-concussion syndrome: A diffusion tensor tractography study. Indian J Radiol Imaging. 2015; doi:10.4103/0971-3026.169445

246.   Basser PJ, Mattiello J, LeBihan D. MR diffusion tensor spectroscopy and imaging. Biophys J. 1994; doi:10.1016/S0006-3495(94)80775-1

247.   Koerte IK, Ertl-wagner B, Reiser M, Zafonte R, Shenton ME. Players Without a Symptomatic Concussion. JAMA J Am Med Assoc. 2014; doi:10.1001/jama.2012.13735.White

248.   Newcombe VFJ, Williams GB, Nortje J, Bradley PG, Harding SG, Smielewski P, et al. Analysis of acute traumatic axonal injury using diffusion tensor imaging. Br J Neurosurg. 2007; doi:10.1080/02688690701400882

249.   Kulkarni P, Morrison TR, Cai X, Iriah S, Simon N, Sabrick J, et al. Neuroradiological Changes Following Single or Repetitive Mild TBI. Front Syst Neurosci. 2019; doi:10.3389/fnsys.2019.00034

250.   McCunn P, Xu X, Li A, Brown A, Bartha R. Neurite Orientation Dispersion and Density Imaging (NODDI) in a Rodent Model of Early Mild Traumatic Brain Injury. 2020.

251.   Monnerie H, Tang-Schomer MD, Iwata A, Smith DH, Kim HA, Le Roux PD. Dendritic alterations after dynamic axonal stretch injury in vitro. Exp Neurol. 2010; doi:10.1016/j.expneurol.2010.05.001

252. Zander NE, Piehler T, Boggs ME, Banton R, Benjamin R. In vitro studies of primary explosive blast loading on neurons. J Neurosci Res. 2015; doi:10.1002/jnr.23594

253. Petraglia A, Plog B, Dayawansa S, Dashnaw M, Czerniecka K, Walker C, et al. The pathophysiology underlying repetitive mild traumatic brain injury in a novel mouse model of chronic traumatic encephalopathy. Surg Neurol Int. 2014; doi:10.4103/2152-7806.147566

254. Wofford KL, Harris JP, Browne KD, Brown DP, Grovola MR, Mietus CJ, et al. Rapid neuroinflammatory response localized to injured neurons after diffuse traumatic brain injury in swine. Exp Neurol. 2017; doi:10.1016/j.expneurol.2017.01.004

255. Patterson ZR, Holahan MR. Understanding the neuroinflammatory response following concussion to develop treatment strategies. Front Cell Neurosci. 2012; doi:10.3389/fncel.2012.00058

256. Briones TL, Woods J, Rogozinska M. Decreased neuroinflammation and increased brain energy homeostasis following environmental enrichment after mild traumatic brain injury is associated with improvement in cognitive function. Acta Neuropathol Commun. 2014; doi:10.1186/2051-5960-1-57

257. Lozano D, Gonzales-Portillo GS, Acosta S, de la Pena I, Tajiri N, Kaneko Y, et al. Neuroinflammatory responses to traumatic brain injury: Etiology, Clinical consequences, And therapeutic opportunities. Neuropsychiatric Disease and Treatment. 2015. doi:10.2147/NDT.S65815

258. Thelin EP, Tajsic T, Zeiler FA, Menon DK, Hutchinson PJA, Carpenter KLH, et al. Monitoring the neuroinflammatory response following acute brain injury. Frontiers in Neurology. 2017. doi:10.3389/fneur.2017.00351

259. Schmidt OI, Infanger M, Heyde CE, Ertel W, Stahel PF. The role of neuroinflammation in traumatic brain injury. European Journal of Trauma. 2004.

doi:10.1007/s00068-004-1394-9

260. Harris NG, Verley DR, Gutman BA, Sutton RL. Bi-directional changes in fractional anisotropy after experiment TBI: Disorganization and reorganization? Neuroimage. 2016; doi:10.1016/j.neuroimage.2016.03.012

261. Kraus MF, Susmaras T, Caughlin BP, Walker CJ, Sweeney JA, Little DM. White matter integrity and cognition in chronic traumatic brain injury: A diffusion tensor imaging study. Brain. 2007; doi:10.1093/brain/awm216

262. Eierud C, Craddock RC, Fletcher S, Aulakh M, King-Casas B, Kuehl D, et al. Neuroimaging after mild traumatic brain injury: Review and meta-analysis. NeuroImage Clin. 2014; doi:10.1016/j.nicl.2013.12.009

263. O'Donnell LJ, Pasternak O. Does diffusion MRI tell us anything about the white matter? An overview of methods and pitfalls. Schizophrenia Research. 2015. doi:10.1016/j.schres.2014.09.007

264. Dyrby TB, Innocenti GM, Bech M, Lundell H. Validation strategies for the interpretation of microstructure imaging using diffusion MRI. NeuroImage. 2018. doi:10.1016/j.neuroimage.2018.06.049

265. McCrea M, Iverson GL, McAllister TW, Hammeke TA, Powell MR, Barr WB, et al. An integrated review of recovery after mild traumatic brain injury (MTBI): Implications for clinical management. Clinical Neuropsychologist. 2009. doi:10.1080/13854040903074652

266. Vanderploeg RD, Curtiss G, Luis CA, Salazar AM. Long-term morbidities following self-reported mild traumatic brain injury. J Clin Exp Neuropsychol. 2007; doi:10.1080/13803390600826587

267. Alexander DC. A general framework for experiment design in diffusion MRI and its application in measuring direct tissue-microstructure features. Magn Reson Med. 2008; doi:10.1002/mrm.21646

268. Hovens I, Nyakas C, Schoemaker R. A novel method for evaluating microglial activation using ionized calcium-binding adaptor protein-1 staining: cell body to cell size ratio. Neuroimmunol Neuroinflammation. 2014; doi:10.4103/2347-8659.139719

269. Myer DJ, Gurkoff GG, Lee SM, Hovda DA, Sofroniew M V. Essential protective roles of reactive astrocytes in traumatic brain injury. Brain. 2006; doi:10.1093/brain/awl165

270. Cotrina ML, Chen M, Han X, Iliff J, Ren Z, Sun W, et al. Effects of traumatic brain injury on reactive astrogliosis and seizures in mouse models of Alexander disease. Brain Res. 2014; doi:10.1016/j.brainres.2014.07.029

271. Ekmark-Lewén S, Flygt J, Kiwanuka O, Meyerson BJ, Lewén A, Hillered L, et al. Traumatic axonal injury in the mouse is accompanied by a dynamic inflammatory response, astroglial reactivity and complex behavioral changes. J Neuroinflammation. 2013; doi:10.1186/1742-2094-10-44

272. Alluri H, Shaji CA, Davis ML, Tharakan B. A mouse controlled cortical impact model of traumatic brain injury for studying blood–brain barrier dysfunctions. Methods in Molecular Biology. Humana Press Inc.; 2018. pp. 37–52. doi:10.1007/978-1-4939-7526-6_4

273. Smith C, Gentleman SM, Leclercq PD, Murray LS, Griffin WST, Graham DI, et al. The neuroinflammatory response in humans after traumatic brain injury. Neuropathol Appl Neurobiol. 2013; doi:10.1111/nan.12008

274. Maxwell WL, MacKinnon MA, Stewart JE, Graham DI. Stereology of cerebral cortex after traumatic brain injury matched to the Glasgow Outcome Score. Brain. 2010; doi:10.1093/brain/awp264

275. Giunta B, Obregon D, Velisetty R, Sanberg PR, Borlongan C V., Tan J. The immunology of traumatic brain injury: a prime target for Alzheimer's disease prevention. Journal of Neuroinflammation. 2012. doi:10.1186/1742-2094-9-185

276. Donat CK, Scott G, Gentleman SM, Sastre M. Microglial activation in traumatic brain injury. Frontiers in Aging Neuroscience. 2017. doi:10.3389/fnagi.2017.00208

277. Shen Z, Bao X, Wang R. Clinical PET imaging of microglial activation: Implications for microglial therapeutics in Alzheimer's disease. Frontiers in Aging Neuroscience. 2018. doi:10.3389/fnagi.2018.00314

278. Ebert SE, Jensen P, Ozenne B, Armand S, Svarer C, Stenbaek DS, et al. Molecular imaging of neuroinflammation in patients after mild traumatic brain injury: a longitudinal 123I-CLINDE single photon emission computed tomography study. Eur J Neurol. 2019; doi:10.1111/ene.13971

279. Liu GJ, Middleton RJ, Hatty CR, Kam WWY, Chan R, Pham T, et al. The 18 kDa translocator protein, microglia and neuroinflammation. Brain Pathol. 2014; doi:10.1111/bpa.12196

280. Boutin H, Prenant C, Maroy R, Galea J, Greenhalgh AD, Smigova A, et al. [18F]DPA-714: Direct Comparison with [11C]PK11195 in a Model of Cerebral Ischemia in Rats. PLoS One. Public Library of Science; 2013;8. doi:10.1371/journal.pone.0056441

281. Nguyen V-D, Leoni M, Dancheva T, Jansson J, Hoffman J, Wassermann D, et al. Portable simulation framework for diffusion MRI. 2019; Available: http://arxiv.org/abs/1908.01719

282. Marshall S, Bayley M, McCullagh S, Velikonja D, Berrigan L, Ouchterlony D, et al. Updated clinical practice guidelines for concussion/mild traumatic brain injury and persistent symptoms. Brain Inj. 2015; doi:10.3109/02699052.2015.1004755

283. Mondello S, Schmid K, Berger RP, Kobeissy F, Italiano D, Jeromin A, et al. The Challenge of Mild Traumatic Brain Injury: Role of Biochemical Markers in Diagnosis of Brain Damage. Med Res Rev. 2014; doi:10.1002/med.21295

Appendices

Appendix A: Permission for Reproduction of Scientific Articles and Figures

PLS Clear

PARTIES:

1. **Cambridge University Press** [CompanyNumber] (Licensor); and
2. **Patrick McCunn** (Licensee).

Thank you for your recent permission request. Some permission requests for use of material published by the Licensor, such as this one, are now being facilitated by PLSclear.

Set out in this licence cover sheet (the **Licence Cover Sheet**) are the principal terms under which Licensor has agreed to license certain Licensed Material (as defined below) to Licensee. The terms in this Licence Cover Sheet are subject to the attached General Terms and Conditions, which together with this Licence Cover Sheet constitute the licence agreement (the **Licence**) between Licensor and Licensee as regards the Licensed Material. The terms set out in this Licence Cover Sheet take precedence over any conflicting provision in the General Terms and Conditions.

Free Of Charge Licence Terms

Licence Date:	13/04/2020
PLSclear Ref No:	36231

The Licensor

Company name:	**Cambridge University Press**
Address:	**University Printing House** **Shaftesbury Road** **Cambridge** **CB2 8BS** **GB**

The Licensee

Licensee Contact Name:	Patrick McCunn
Licensee Address:	1151 Richmond St. N. London N6A 5B7 Canada

Licensed Material

title:	MRI from Picture to Proton
ISBN:	9780521683845
publisher:	Cambridge University Press

Are you requesting permission to reuse the cover of the publication?	No
Figure number & title	Figure 7.16
Page numbers	125
Will it be cropped	No
Are you requesting permission to reuse the cover of the publication?	No
Figure number & title	Figure 7.19
Page numbers	129
Will it be cropped	No

For Use In Licensee's Publication(s)

usage type	Book, Journal, Magazine or Academic Paper-Thesis / Dissertation
Will your dissertation be placed in an online repository?	Yes
Author	Patrick McCunn
Estimated publication date	July 2020
Language	English
Title of dissertation/thesis	Neurite Orientation Dispersion and Density Imaging (NODDI) in a rodent model of Mild Traumatic Brain Injury (mTBI) at 9.4 Tesla
University or institution	The University of Western Ontario
Unlimited circulation?	Yes

Rights Granted

Exclusivity:	Non-Exclusive
Format:	Thesis / Dissertation
Language:	English
Territory:	World
Duration:	Lifetime of Licensee's Edition
Maximum Circulation:	Unlimited

GENERAL TERMS AND CONDITIONS

1. Definitions and Interpretation

1.1 Capitalised words and expressions in these General Terms and Conditions have the meanings given to them in the Licence Cover Sheet.

1.2 In this Licence any references (express or implied) to statutes or provisions are references to those statutes or provisions as amended or re-enacted from time to time. The term including will be construed as illustrative, without limiting the sense or scope of the words preceding it. A reference to in writing or written includes faxes and email. The singular includes the plural and vice versa.

2. Grant of Rights

2.1 The Licensor grants to Licensee the non-exclusive right to use the Licensed Material as specified in the Licence Cover Sheet.

2.2 The rights licensed to Licensee under this Licence do not include the right to use any third party copyright material incorporated in the Licensed Material. Licensee should check the Licensed Material carefully and seek permission for the use of any such third party copyright material from the relevant copyright owner(s).

2.3 Unless otherwise stated in the Licence Cover Sheet, the Licensed Material may be:

2.3.1 subjected to minor editing, including for the purposes of creating alternative formats to provide access for a beneficiary person (provided that any such editing does not amount to derogatory treatment); and/or

2.3.2 used for incidental promotional use (such as online retail providers' search facilities).

2.4 Save as expressly permitted in this Licence or as otherwise permitted by law, no use or modification of the Licensed Material may be made by Licensee without Licensor's prior written permission.

3. Copyright Notice and Acknowledgement

3.1 Licensee must ensure that the following notices and acknowledgements are reproduced prominently alongside each reproduction by Licensee of the Licensed Material:

3.1.1 the title and author of the Licensed Material;

3.1.2 the copyright notice included in the Licensed Material; and

3.1.3 the statement "Reproduced with permission of The Licensor through PLSclear."

4. Reversion of Rights

4.1 The rights licensed to Licensee under this Licence will terminate immediately and automatically upon the earliest of the following events to occur:

4.1.1 the Licensed Material not being used by Licensee within 18 months of the Licence Date;

4.1.2 expiry of the Licence Duration; or

4.1.3 the Maximum Circulation being reached.

5. Miscellaneous

5.1 By using the Licensed Material, Licensee will be deemed to have accepted all the terms and conditions contained in this Licence.

5.2 This Licence contains the entire understanding and agreement of the parties relating to its subject matter and supersedes in all respects any previous or other existing arrangements, agreements or understandings between the parties whether oral or written in relation to its subject matter.

5.3 Licensee may not assign this Licence or any of its rights or obligations hereunder to any third party without Licensor's prior written consent.

5.4 This Licence is governed by and shall be construed in accordance with the laws of England and Wales and the parties hereby irrevocably submit to the non-exclusive jurisdiction of the Courts of England and Wales as regards any claim, dispute or matter arising under or in relation to this Licence.

PLOS ONE

Licenses and Copyright

LF Lawrence R Frank
Sun 4/12/2020 5:36 PM
Patrick McCunn ⩢

Dear Patrick,

Sure you can certainly use those figures. I'm glad you found them useful.

And I'm very glad to hear you liked the textbook and found that useful as well. I'd be very curious to know how much of it you read, and what parts you found most helpful (and which parts not so much). If I do every return to finishing it, I would most like have to reduce its size. So knowing what sections people found most useful would be good to know.

Good luck writing the thesis!

Best,
Larry

Appendix B: Health Sciences Research Ethics Board Approval Notices

AUP Number: 2018-176
PI Name: Brown, Arthur
AUP Title: Investigations of CNS Injury and Regenerative Therapies
Approval Date: 03/01/2019

Official Notice of Animal Care Committee (ACC) Approval:
Your new Animal Use Protocol (AUP) 2018-176:1: entitled " Investigations of CNS Injury and Regenerative Therapies "
has been APPROVED by the Animal Care Committee of the University Council on Animal Care. This approval, although valid for up to four years, is subject to annual Protocol Renewal.

Prior to commencing animal work, please review your AUP with your research team to ensure full understanding by everyone listed within this AUP.

As per your declaration within this approved AUP, you are obligated to ensure that:
      1) Animals used in this research project will be cared for in alignment with:
            a) Western's Senate MAPPs 7.12, 7.10, and 7.15
            http://www.uwo.ca/univsec/policies_procedures/research.html
            b) University Council on Animal Care Policies and related Animal Care Committee
procedures
            http://uwo.ca/research/services/animalethics/animal_care_and_use_policies.htm
      2) As per UCAC's Animal Use Protocols Policy,
            a) this AUP accurately represents intended animal use;
            b) external approvals associated with this AUP, including permits and
              scientific/departmental peer approvals, are complete and accurate;
            c) any divergence from this AUP will not be undertaken until the related Protocol
              Modification is approved by the ACC; and
            d) AUP form submissions - Annual Protocol Renewals and Full AUP Renewals - will be
              submitted and attended to within timeframes outlined by the ACC.
            e) http://uwo.ca/research/services/animalethics/animal_use_protocols.html

      3) As per MAPP 7.10 all individuals listed within this AUP as having any hands-on animal contact will
            a) be made familiar with and have direct access to this AUP;
            b) complete all required CCAC mandatory training (training@uwo.ca); and
            c) be overseen by me to ensure appropriate care and use of animals.
      4) As per MAPP 7.15,
            a) Practice will align with approved AUP elements;
            b) Unrestricted access to all animal areas will be given to ACVS Veterinarians and ACC
Leaders;
            c) UCAC policies and related ACC procedures will be followed, including but not limited
to:
                    i) Research Animal Procurement
                    ii) Animal Care and Use Records
                    iii) Sick Animal Response
                    iv) Continuing Care Visits
      5) As per institutional OH&S policies, all individuals listed within this AUP who will be using or potentially
           exposed to hazardous materials will have completed in advance the appropriate institutional OH&S
           training, facility-level training, and reviewed related (M)SDS Sheets,
           http://www.uwo.ca/hr/learning/required/index.html

Submitted by: Copeman, Laura
on behalf of the Animal Care Committee
University Council on Animal Care

Western

AUP Number: 2017-108
PI Name: Strong, Michael
AUP Title: Somatic gene transfer to express Thr175Asp-tau, Thr175Ala-tau or wild-type tau in rat hippocampus.
Approval Date: 02/01/2018

Official Notice of Animal Care Committee (ACC) Approval:
Your new Animal Use Protocol (AUP) 2017-108:1: entitled " Somatic gene transfer to express Thr175Asp-tau, Thr175Ala-tau or wild-type tau in rat hippocampus."
has been APPROVED by the Animal Care Committee of the University Council on Animal Care. This approval, although valid for up to four years, is subject to annual Protocol Renewal.

Prior to commencing animal work, please review your AUP with your research team to ensure full understanding by everyone listed within this AUP.

As per your declaration within this approved AUP, you are obligated to ensure that:
  1) Animals used in this research project will be cared for in alignment with:
       a) Western's Senate MAPPs 7.12, 7.10, and 7.15
        http://www.uwo.ca/univsec/policies_procedures/research.html

        b) University Council on Animal Care Policies and related Animal Care Committee procedures
       http://uwo.ca/research/services/animalethics/animal_care_and_use_policies.htm
   2) As per UCAC's Animal Use Protocols Policy,
         a) this AUP accurately represents intended animal use;
        b) external approvals associated with this AUP, including permits and scientific/departmental peer approvals, are complete and accurate;
        c) any divergence from this AUP will not be undertaken until the related Protocol Modification is approved by the ACC; and
        d) AUP form submissions - Annual Protocol Renewals and Full AUP Renewals - will be submitted and attended to within timeframes outlined by the ACC.
          e) http://uwo.ca/research/services/animalethics/animal_use_protocols.html

  3) As per MAPP 7.10 all individuals listed within this AUP as having any hands-on animal contact will
       a) be made familiar with and have direct access to this AUP;
        b) complete all required CCAC mandatory training (training@uwo.ca); and
         c) be overseen by me to ensure appropriate care and use of animals.
   4) As per MAPP 7.15,
        a) Practice will align with approved AUP elements;
         b) Unrestricted access to all animal areas will be given to ACVS Veterinarians and ACC Leaders;
         c) UCAC policies and related ACC procedures will be followed, including but not limited to:
              i) Research Animal Procurement
             ii) Animal Care and Use Records
               iii) Sick Animal Response
             iv) Continuing Care Visits
    5) As per institutional OH&S policies, all individuals listed within this AUP who will be using or potentially exposed to hazardous materials will have completed in advance the appropriate institutional OH&S training, facility-level training, and reviewed related (M)SDS Sheets,
     http://www.uwo.ca/hr/learning/required/index.html

Submitted by: Copeman, Laura
on behalf of the Animal Care Committee
University Council on Animal Care

*** THIS IS AN EMAIL NOTIFICATION ONLY. PLEASE DO NOT REPLY ***

Curriculum Vitae

Education

Doctor of Philosophy   **2014 - 2020**
Medical Biophysics
Western University, London, ON.

Master of Science   **2016 - 2018**
Clinical Medical Biophysics (CAMPEP)
Western University, London, ON.

Bachelor of Science   **2009 - 2013**
Honours, Chemical Physics; Honours, Human Kinetics
University of Guelph, Guelph, ON.

Research Experience

The Hospital for Sick Children   **2020 – Present**
Research Fellow
- o Developed Magnetic Resonance Imaging (MRI) pipelines to study clinical presentations of Post-Traumatic Stress Disorder in military personnel.

Western University   **2014 - Present**
Research Associate
- o Developed novel Magnetic Resonance Imaging (MRI) techniques to study pre-clinical models of concussion, neurodegeneration and cancer. Expected May 2020.

University of Guelph   **2012 - 2013**
Research Assistant
- o Explored the use of ultrasound imaging to measure muscle fiber orientation of the illiocostalis lumborum and longissimus thoracis under varying conditions of abdominal flexion.

University of Guelph   **2012 – 2013**
Research Assistant
- o Studied the use of classroom lecture capture technology as related to perceived level of topic difficulty in undergraduate education.

Academic Work Experience

Applications Specialist   **2020 - Present**
Scintica Instrumentation Inc.
Imaging Division
- o Pursued and developed product leads and sales bids for research equipment sales.
- o Developed product specific marketing content and sales support documents.
- o Produced publication reference lists for various research imaging equipment.

Sessional Professor   **2016 - 2019**
Fanshawe College
Department of Health Sciences
- o Oversaw all aspects of course delivery including content creation, marking, and evaluation
- o Supervised and guided novice sessional professors in course delivery and content.

Quality Assurance   **2017 - 2019**
Department of Radiology
Victoria Hospital, London, ON.
- o Performed quality assurance of various aspects of clinical linear accelerators.
- o Ensured accurate electron and photon beam radiation output to maintain accurate patient treatment and dose deposition.

Supported Learning Group Leader   **2010 - 2013**
University of Guelph
Canadian National Center for Supplemental Instruction
- o Facilitated weekly help sessions to aid students in course content and learning strategies.
- o Planned sessions and created alternative course content in line with institutional and instructional outcomes.

Academic Scholarship and Awards

- o Graduate Student Innovation Scholar   **2019**
- o Western Graduate Research Scholarship   **2019**
- o Proteus Innovation Competition Winner   **2018**
- o Western Graduate Research Scholarship   **2018**
- o Ivey-Deloitte Entrepreneurship Bootcamp Winner   **2018**
- o Proteus Innovation Competition Winner   **2017**
- o Western Graduate Research Scholarship   **2017**
- o QEII Graduate Scholarship in Science & Technology   **2015 – 2016**
- o Western Graduate Research Scholarship   **2016**
- o Robarts Research Day Presentation Award   **2015**
- o Western Graduate Research Scholarship   **2014**

Publications

Moszczynski AJ., Harvey M., Fulcher N., deOliviera C., **McCunn P.,** Donison N., Bartha R., Schmid S., Strong MJ., Volkening K. Synergistic toxicity in an *in vivo* model of neurodegeneration through the co-expression of human TDP-43M337V and Thr175Asp tau protein. *acta neuropathol commun* **7,** 170 (2019)

McCunn, P., Gilbert, K., Zeman, P., Li, A., Strong, M., Khan, A., Bartha, R. (2019). Reproducibility of Neurite Orientation Dispersion and Density Imaging (NODDI) in rats at 9.4 Tesla. *PLOS ONE*, *14*(4).

Moszczynski, A., Gopaul, J., **McCunn, P.,** Volkening, K., Harvey, M., Bartha, R., Schmid, S., Strong, MJ. (2018). Somatic Gene Transfer Using a Recombinant Adenoviral Vector (rAAV9) Encoding Pseudo phosphorylated Human Thr175 Tau in Adult Rat Hippocampus Induces Tau Pathology. *Journal Of Neuropathology & Experimental Neurology*, *77*(8).

Newton, G., & **McCunn, P.** (2015). Student perception of topic difficulty: Lecture capture in higher education. *Australasian Journal of Educational Technology*, *31*(3).

Manuscripts Submitted for Publication

McCunn, P., Xu, X. Li, A., Brown, A., Bartha, R. Neurite Orientation Dispersion and Density Imaging (NODDI) in a rodent model of Mild Traumatic Brain Injury. *In revisions with Journal of Neurotrauma.*

McCunn, P., Richardson, J.D., Jetly, R., and Dunkley, B. Diffusion Tensor Imaging Reveals White Matter Differences in Military Personnel Exposed to Trauma with and without Post-traumatic Stress Disorder. *Submitted to Psychiatry Research*.

Manuscripts in Preparation

McCunn, P., Xu, X. Li, A., Brown, A., Bartha, R. Neurite Orientation Dispersion and Density Imaging (NODDI) in a rodent model of repetitive Mild Traumatic Brain Injury